

Correlated electron systems with antiferromagnetic spin interaction

Zur Erlangung des akademischen Grades eines
DOKTORS DER NATURWISSENSCHAFTEN
von der Fakultät für Physik der
Universität (TH) Karlsruhe

genehmigte

DISSERTATION

von

Dipl.-Phys. Holger Schmidt

aus Offenburg

Referent:	Prof. Dr. Peter Wölfle
Korreferent:	Prof. Dr. Alexander Shnirman
Tag der mündlichen Prüfung:	23. Oktober 2009

Contents

1	Preface	5
I	Kondo Dot Model in and out of Equilibrium: Functional RG Approach	7
2	Introduction	9
3	Introduction to the Kondo Model	13
3.1	Introduction	13
3.2	Single Impurity Anderson Model	13
3.3	Kondo Model	15
3.4	Kondo Dot Model	15
3.5	Brief History of the Kondo Model	17
3.5.1	Kondo Effect and Kondo Problem	18
3.5.2	Anderson's Poor Man Scaling	19
3.5.3	Numerical Renormalization Group	20
3.5.4	Local Fermi Liquid Picture	21
4	Equilibrium and Nonequilibrium Functional Renormalization Group Method	23
4.1	Introduction	23
4.2	Functional Formalism and Generating Functionals	24
4.3	Equilibrium Functional Renormalization Group	26
4.4	Keldysh Formalism and Propagators for the Kondo Dot Model	29
4.4.1	Green Functions	30
4.4.2	Interaction Vertices	34
4.5	Nonequilibrium Functional Renormalization Group	35
5	The FRG to the Kondo Dot Model	41
5.1	Introduction	41
5.2	Prelude	42
5.2.1	Perturbative Expressions	42
5.2.2	Recovering Second Order Perturbation Theory	43
5.2.3	Poor Man's Scaling Limit	43
5.2.4	Perturbative Renormalization Group	45
5.3	Weak Coupling Regime	46

5.3.1	Vertex Function Structure	46
5.3.2	Approximated Flow Equations	49
5.3.3	Weak Coupling and Linear Response at Finite Temperature	50
5.3.4	Weak Coupling at Finite Bias Voltage	55
5.4	Towards the Strong Coupling Regime	60
6	Experimental Overview	67
6.1	Introduction	67
6.2	Kondo Quantum Dots in Equilibrium	67
6.3	Kondo Quantum Dots out of Equilibrium	70
7	Conclusion and Outlook	73
II	Magnetic Excitations from Cite-Centered Stripes in CuO Superconductors	75
8	Introduction	77
9	Theory and Method	81
9.1	Introduction	81
9.2	Basis States for Three-Site Rungs	81
9.3	Coupling the Rungs	85
9.4	Expanding the Hamiltonian	87
9.5	Solution by Bogoliubov Transformation	90
10	Results and Discussion	93
10.1	Introduction	93
10.2	Estimating the Interladder Coupling	93
10.3	Results	94
11	Conclusion	101
A	The Pseudo-Fermion Representation	103
B	Grassmann Algebra	105
C	Derivation of the Functional Integral	107
D	Details on the Nonequilibrium FRG for the Kondo Model	111
E	Useful Relations and Formulas	115
F	Matrix Elements of the Individual Spin Operators on Rungs	117
G	Analysis of \tilde{E}_0, \hat{H}_{a0}, \hat{H}_{c0}, \hat{H}_{a1}, and \hat{H}_{c2}	121

H Matrix Elements	125
I Staggered Magnetization	127

πάντα ῥεῖ (Heraklit)

List of publications

1. Holger Schmidt and Peter Wölfle, *Transport through a Kondo quantum dot: Functional RG approach*, submitted to Ann. Phys. (Berlin)
2. Martin Greiter and Holger Schmidt, *Evidence for site-centered stripes from magnetic excitations in CuO superconductors*, submitted to Phys. Rev. Lett
3. Martin Greiter and Holger Schmidt, *Magnetic excitations in the cite-centered stripe phase: spin wave theory of coupled three leg ladders*, to be submitted to Phys. Rev. B

1 Preface

For many classes of correlated electron systems the electronic spin plays a major role as the correlations mediated by it lead to a variety and novelty of collective quantum phenomena. Even one single magnetic moment which interacts with a continuum of electrons is able to produce a complex, correlated many body quantum state.

Such a situation can be prepared by connecting a small semiconductor box to two electronic reservoirs - a so-called quantum dot. A gate voltage applied to the quantum dot can tune the system into a regime where effectively only one single electron with a non-zero magnetic moment remains as a degree of freedom on the dot. Without the electronic spin, electron transport would be prohibited by the Coulomb blockade. However, the effective spin on the dot interacts locally with the surrounding spins of the lead electrons and thereby generates a coherent quantum many body state, a state built by coherent spin flip processes. This resonance state enhances the density of states of the quantum dot near the Fermi level of the leads, which in turn leads directly to an increase of the conductance, a phenomenon known as the Kondo effect. Due to the Kondo resonance state the local spin forms a spin singlet with the lead electrons, which effectively screens the local spin and subsequently makes the dot fully transparent, i.e. the Coulomb Blockade is completely overcome and the maximal value of conductance allowed by quantum mechanics, the so called unitary limit, is reached. Applying a finite bias voltage between the two leads destroys this quantum coherent state again and hence leads to a suppression of the Kondo effect.

Theoretically this physics is captured by the Kondo model which results as a certain limit from the single impurity Anderson model. Both models play prominent roles when dealing with quantum dot devices and have a long history in the physics of quantum impurity systems. In this work we will treat the Kondo model theoretically in and out of equilibrium using the functional renormalization group (fRG) method. The fRG—as a powerful, microscopic and first principle method when dealing with correlated systems—allows us to substantiate and improve previous renormalization group schemes for the Kondo model. In particular, we shall first of all extend the fRG to a nonequilibrium situation and give a detailed derivation of the corresponding, approximated flow equations for the Kondo model. One of the major subjects is addressed by the question how decoherence rates which especially out of equilibrium serves as a cutoff for the fRG equations are generated by the fRG. We will thus be able to strengthen and substantiate previous proposed RG schemes and find excellent accordance with known results in the weak coupling regime. We shall further analyze the breakdown of our approximated set of fRG equations as we enter the strong coupling regime and give an outlook how the latter may be approached.

Another fascinating class of materials where spin correlations take center stage are high temperature superconductivity compounds, the conventional example of which is composed of two dimensional CuO planes. Without any doping and at zero temperature these planes represent a perfect realization of a two dimensional antiferromagnet on a square lattice which is described by a standard Heisenberg Hamiltonian having magnons as its elementary excitations. Upon doping and varying the temperature, a rich phase diagram emerges. Most notably in a certain range of doping degree these materials become superconducting. However, at a certain value inside this superconducting dome, superconductivity is suppressed and the CuO planes are seen to arrange themselves in spin and charge stripes with a spin modulation of eight and charge modulation of four lattice sites, respectively. Recent neutron scattering experiments have focused on this regime of doping degree and measured the magnetic scattering from which a dispersion of the magnetic excitations is extracted.

Theoretically at this doping degree the material is believed to be best described by the t - J Hamiltonian which, besides the antiferromagnetic spin correlation, includes the mobility of the holes as a kinetic degree of freedom. We will, however, first of all map the system onto a spin only Heisenberg type model as we antiferromagnetically couple three leg ladders. We thus neglect the kinetic degree of freedom of the holes and replace them by an effective, antiferromagnetic exchange coupling of neighboring spin ladders. Contrary to this so called site-centered model people studied a bond-centered model previously, corresponding to ferromagnetically coupled two leg ladders to be appropriate to capture the physics at this doping level.

In this thesis we will show that there is evidence for site- rather than bond-centered stripes and hence answer one of the basic questions in this regard. We also shall numerically estimate the induced inter-ladder coupling—which in case of the bond-centered model has so far been taken as a fitting parameter or chosen such that the required Goldstone modes just emerge—for the site-centered as well as for the bond-centered model and show that only the site-centered stripes exhibit magnetic order. Furthermore, we present a fully consistent spin wave analysis of coupled three leg ladders and compare various observables, like the magnetic excitation spectrum or the dynamical structure factor with recent neutron scattering experiments. We find excellent agreement.

Part I

Kondo Dot Model in and out of Equilibrium: Functional RG Approach

2 Introduction

The Kondo effect—a physical phenomenon already discovered in the early 1930s, explained in the 1960s and since then has been the subject of numerous reviews—is still in the center of interest of both experimental and theoretical physics. In the past decade it even experienced a revival [1]. Besides the fact that the Kondo effect in its own manner is an intriguing phenomenon as it displays a beautiful example of a correlated, complex many body quantum state, it entailed a variety of research areas and challenges to overcome.

It was observed [2, 3] that if magnetic ions are added to a metal, the resistance no longer monotonically decreases down to a residual value, but starts to increase again below a certain temperature, which became known as the Kondo effect. Jun Kondo [4] in 1964 first explained this scenario by means of perturbation theory. Although he was able to predict the logarithmic increase of the resistivity his result diverged at a temperature T_K , the Kondo temperature. This breakdown of the perturbative result is known as the Kondo problem. In the subsequent years no effort has been spared in various attempts to obtain a solution for the Kondo problem, as for instance by parquet approximation, a resummation of certain classes of diagrams [5, 6, 7] or using self-consistent perturbation theory [8, 9]. Although this methods turned out to be adequate for temperatures larger than T_K and gave a finite result as $T \rightarrow 0$ the crossover regime $T \approx T_K$ and the initial slope turned out to be incorrect when comparing to experiment and to the strong coupling solution for $T \ll T_K$, that was provided by P. Nozieres [10] by means of a local Fermi liquid picture. For the understanding of the physics below T_K more sophisticated theoretical approaches were necessary. A first successful step was made half a decade after Kondo’s theory by P.W. Anderson [11] with a method known as “poor man’s scaling” or perturbative renormalization group. The breakthrough with a non-perturbative method was given by K.G. Wilson [12, 13] via the numerical renormalization group. In the early 80s interest was again attracted to the Kondo model due to the discovery of an exact solution using the Bethe ansatz [14, 15].

An immense progress in nanotechnology made it possible to create little semiconductor boxes that can hold a small number of electrons, so called quantum dots, which are, as they resemble the properties of real atoms, sometimes referred to artificial atoms. An odd number of electrons thereby corresponds to a non zero total localized spin S on the dot with a minimum value of $S = \frac{1}{2}$. To study the Kondo problem—i.e. to mimic a cobalt-in-copper system—this localized spin is pinched between two electronic leads which became known as the Kondo dot model. If a gate voltage is applied to this quantum dot device the dot levels can be tuned in a way that effectively only one single

electron with a non-zero magnetic moment remains as a degree of freedom on the quantum dot. This local effective spin now interacts with the surrounding lead electron spins and thereby generates a coherent quantum many body state, which has far reaching consequences: To begin with, it enhances the density of states of the quantum dot near the Fermi level of the leads, which in turn leads directly to an increase of the conductance, i.e. it produces the Kondo effect. Hence, due to this Kondo resonance state the local spin forms a singlet with the spins of the lead electrons, which effectively screens the local spin and thereby makes the dot fully transparent, i.e. the Coulomb Blockade is completely overcome. While in the case of an impurity embedded in a bulk material the Kondo effect manifests itself in the increase of the resistance due to scattering of plane wave electronic states from the impurity and the transfer of momentum, which is thereby generated, the situation for a quantum dot is quite different. Since in this case all the electrons have to travel through the dot, the Kondo resonance affirms the mixing of electrons between different leads and hence leads to an increase of the conductivity. If, however, in the two lead setup a finite bias is applied between the two electronic leads the situation changes again as the voltage destroys the Kondo correlation and hence diminishes the conductance again.

In the present work we apply the functional renormalization group (FRG) method to study the Kondo dot model in and out of equilibrium. The fermionic FRG is a powerful method for the treatment of correlated electron systems. The basic idea is to track the evolution of all one-particle irreducible (1PI) diagrams when an infrared cutoff Λ is lowered. Technically this leads to an infinite system of coupled differential equations for the 1PI vertex functions, which are—in principle—fully dressed and frequency (and/or momentum) dependent, giving rise to the name FRG. For any realistic, interacting physical system, however, appropriate simplifications of these equations have to be performed. As the equation for each n -point vertex function involves the $n + 1$ -point vertex function the major approximation, in order to close the differential equation system, is a truncation at a certain order. As in all present examples in the literature we will perform the truncation at order $n = 2$, i.e. we shall only deal with the self energy of the dot spin and the two particle vertex or coupling function. The setup of the FRG equations for the Kondo model and the subsequent calculations will be performed in Keldysh space [16] which provides the fundamental basis when dealing with systems out of equilibrium. As in a theoretical description the Kondo effect derives from logarithmic contributions which are resummed by renormalization group we shall begin our analysis by extracting these leading components in Keldysh space and show that upon keeping track only of these components one is allowed to deal with a single amplitude in Keldysh space. In contrast to previous RG works the FRG naturally includes the effect of the decoherence rate which in particular in nonequilibrium is seen to be instrumental as a cutoff for the frequency dependent coupling function. We are thus able to strengthen and substantiate a previously proposed RG scheme [17, 18] which included this effect on a self-consistent basis. We shall further investigate the behavior of the decoherence rate and the leading component of the coupling function as the temperature or the bias voltage enter the strong coupling regime, i.e. $T, V \lesssim T_K$. As a physical observable we focus mainly on the

conductance G as a function of the temperature T and bias voltage V which is obtained from an expression in terms of the renormalized coupling function which is seen to agree very well with known results in the weak coupling regime $T, V \gg T_K$. Finally we analyze and give an outlook to the approach to strong coupling.

This thesis is organized as follows: In **Chapter 3** we introduce the single impurity Anderson model (SIAM) and the Kondo model and show how these two models are related, in particular how the latter may be obtained from the former. For the Kondo model we will distinguish between the one-lead model, i.e. a single impurity spin embedded in bulk of conduction electrons and the two-lead model, where the impurity spin is pinched between two fermionic leads. Furthermore, we shall give a short overview about the milestone works in the chronology of the Kondo model, i.e. the Kondo's explanation of the resistance minimum [4], Anderson's poor man scaling approach [11], Wilson's numerical renormalization group approach [12, 13] and Noziere's local Fermi liquid description of the Kondo model [10].

Chapter 4 contains the introduction to the fermionic FRG in and out of equilibrium. After a short summary of functional formalism and path integrals we shall begin with a review of the equilibrium FRG. Towards our main goal—the treatment of the nonequilibrium Kondo model—using FRG we state the Keldysh formalism [16] which is the fundamental technique when dealing with systems out of equilibrium. Furthermore, we give the corresponding Green and vertex functions for the Kondo model. Having this technique at hand we subsequently extend the FRG to nonequilibrium situations and give a detailed derivation of the set of coupled differential equations for the Kondo model, in particular for the pseudo fermion self energy and the vertex function.

Chapter 5 contains the main body of this work, the treatment of the Kondo model using the FRG in and out of equilibrium, i.e. the analysis of the FRG equation derived in Section 3. In a short prelude on the Kondo dot model we start with a summary of second order perturbative results for the pseudo fermion self energy and show how these expressions are reobtained via the FRG. We also show how Anderson's poor man scaling equation [11] is contained as a certain limit in the FRG equations. Moreover we will review a perturbative renormalization group by Rosch *et. al.* [17, 18], which was proposed to capture the physics of a finite bias voltage or the inclusion of a magnetic field and likewise illuminate this theory in the framework of FRG. We then pass on to the main subject of this thesis, the analysis of the FRG equations for the Kondo model in and out of equilibrium. As a first step we will simplify the FRG insofar as we extract the leading components for the vertex function and—upon keeping track only of these components—find that the Keldysh structure of the corresponding vertex function reduces to the one of the bare vertex and hence we are allowed to deal with a single amplitude in Keldysh space only. This is seen to simplify the FRG equations for the imaginary part of the self energy and vertex function substantially. We solve the FRG equations in the weak coupling regime $T, V \gg T_K$ and find excellent accordance with known results. We then focus our attention mainly on the decoherence rate which in particular in nonequilibrium is instrumental to cutoff the otherwise logarithmic divergent coupling function. We shall analyze the behavior and breakdown of our approximated

set of FRG equations as the strong coupling regime $T, V \lesssim T_K$ is entered. Finally we show under which conditions the strong coupling regime may be approached via the FRG.

In **Chapter 6** we shall give an overview of experiments regarding our theoretical research. In the past decades much progress has been achieved to mimic the Kondo situation by means of quantum dot devices coupled to fermion reservoirs which serve as conduction leads. After a few attempts where only a weak Kondo effect has been observed [19, 20, 21] the breakthrough came in 2000 by van der Wiel *et. al.* [22] where “The Kondo effect in the unitary limit” has been achieved. We shall first of all review these experiments in equilibrium before we finally pass on to a recent experiment of the Kondo model out of equilibrium [23].

We close this part of the thesis with a short conclusion in **Chapter 7**.

To enhance readability of the thesis we shall postpone some of the technical details in the appendices. A description of Abrikosov’s pseudo fermion representation [24, 25] and the spin algebra and spin summations in this regard are given in **Appendix A**. In **Appendix B** we briefly summarize basic properties of and rules for Grassman variables and list some integral formulas. **Appendix C** provides a derivation of the non-equilibrium path integral representation for the Kondo dot model according to [26]. Technical details of Chapter 3 that occur during the derivation of the FRG equation for the Kondo dot model in Keldysh space are presented in **Appendix D**. **Appendix E** finally contains some useful formulas and relations for the Bose- and Fermi-functions and integrations in this regard.

3 Introduction to the Kondo Model

3.1 Introduction

This chapter introduces the elementary models in the framework of local moment physics where an impurity is either located in a bulk of conduction electrons or is pinched between two fermionic leads, respectively. In Section 3.2 we begin with the single impurity Anderson model (SIAM) [27] which plays the key role when dealing with impurity systems as it allows for charge fluctuations and incorporates Coulomb interaction on the impurity site. In the limit, where the impurity site is occupied just by one electron, leaving effectively only the electronic spin as a degree of freedom the SIAM can be mapped onto the Kondo model, which is introduced in Section 3.3. The Kondo model describes a bulk of conduction electrons which interact locally via an antiferromagnetic Heisenberg exchange with the impurity spin. If the bulk of electrons is replaced by two fermionic leads and the impurity spin is pinched between them it becomes the Kondo dot or two lead Kondo model, which is discussed in Section 3.4. This model will be studied throughout the thesis. In Section 3.5 we shall give a summary of the keystones in the history of the Kondo model: To begin with we give a short outline on Kondo's explanation of the resistance minimum [4], followed by Anderson's poor man scaling approach [11]. Furthermore we state Wilson's numerical renormalization group procedure [12, 13] (for a review see [28]) and finally the local Fermi liquid picture by Nozières [10].

3.2 Single Impurity Anderson Model

The SIAM is given by the following Hamiltonian

$$H = \sum_{\mathbf{k}\sigma} \epsilon_{\mathbf{k}} c_{\mathbf{k}\sigma}^\dagger c_{\mathbf{k}\sigma} + \sum_{\sigma} \epsilon_d d_{\sigma}^\dagger d_{\sigma} + U n_{\uparrow} n_{\downarrow} + \sum_{\mathbf{k}\sigma} V \left(c_{\mathbf{k}\sigma}^\dagger d_{\sigma} + d_{\sigma}^\dagger c_{\mathbf{k}\sigma} \right). \quad (3.1)$$

The first term represents the free electrons of the metallic host. $c_{\mathbf{k}\sigma}^\dagger$ and $c_{\mathbf{k}\sigma}$ are creation and annihilation operators of conduction electrons with momentum \mathbf{k} and spin σ . The second term describes a local orbital which can be empty, single or double occupied. Each electron occupying the impurity site thereby gains an energy of ϵ_d . The third term emerges from the Coulomb repulsion if two electrons simultaneously occupy the d -level. These three possible configurations are depicted in Fig. 3.2. The last term describes the hybridization, i.e. the hopping of the conduction electrons onto and out of the impurity site.

Depending on the parameters ϵ_d and U the SIAM exhibits different phases: for vanishing

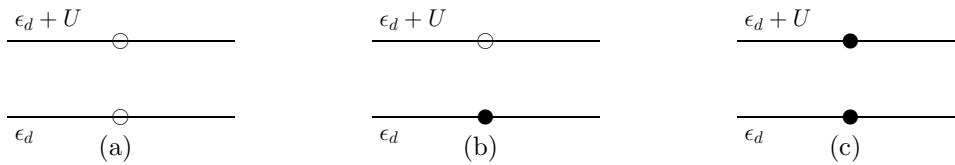


Figure 3.1: Possible configurations for the impurity state with energies (a) $E = 0$, (b) $E = \epsilon_d$, (c) $E = 2\epsilon_d + U$.

hybridization strength $V = 0$ the ground state of the SIAM can either be magnetic or non-magnetic as shown in Fig. 3.2. If the Fermi level is pinched between the upper and lower impurity level the SIAM is in the magnetic phase, whereas if it is completely above or below of the two impurity levels the SIAM becomes non-magnetic. The two cases (not depicted in Fig. 3.2) where either the top or the low level coincides with—or is at least close to—the Fermi level are referred to as the mixed valence regimes.

The model becomes particle-hole symmetric if its parameters are subject to the condition $\epsilon_F - \epsilon_d = \epsilon_d + U - \epsilon_F$ or $\epsilon_d = -U/2$ if we take $\epsilon_F = 0$. For sufficiently large values of U the conditions are now such that the d level contains only a single electron, which behaves as a magnetic spin $1/2$ impurity. However, on lowering the temperature T below a certain crossover value, which is referred to as the Kondo temperature T_K , coherent virtual transitions between the d level and the conduction band begin to "screen" the spin of the d level. The most spectacular consequence is that the impurity density of states develops a so called Kondo or Abrikosov-Suhl resonance, a sharp peak at the Fermi level (depicted in Fig. 3.3). This Kondo resonance reaches its maximal value, which is known as the "unitarity limit," when the ground state wave function is a spin singlet which in turn indicates that the local spin is completely screened. As shown in the next Section in this regime the Anderson model may be described by an effective model, the Kondo model.

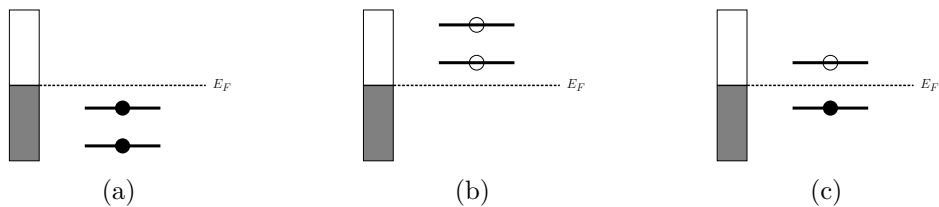


Figure 3.2: Without hybridization (i.e. $V = 0$) the ground state of the SIAM can either be (a), (b) non-magnetic or (c) magnetic.

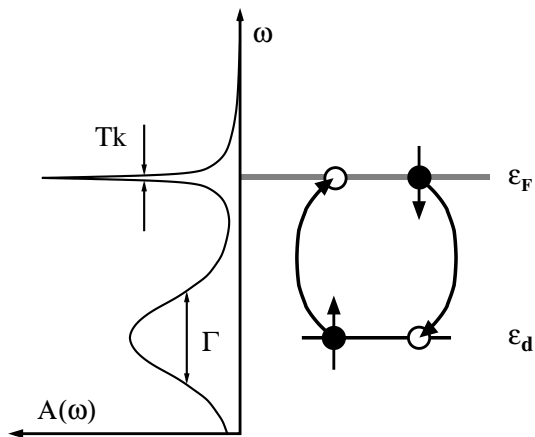


Figure 3.3: Sketch of an effective spin flip. A coherent superposition of such processes leads to a narrow resonance of width T_K in the impurity density of states at the Fermi level ϵ_F . The impurity level ϵ_d is broadened on a scale $\Gamma = \pi|V|^2$.

3.3 Kondo Model

As already marked out in the previous chapter for $\epsilon_d \ll \epsilon_F \ll \epsilon_d + U$ the SIAM enters the so called Kondo regime and can be mapped onto the Kondo (or s - d) model. Technically this is achieved by a Schrieffer-Wolff [29] transformation. The corresponding Hamiltonian takes the form

$$H = \sum_{\mathbf{k}\sigma} \epsilon_{\mathbf{k}} c_{\mathbf{k}\sigma}^\dagger c_{\mathbf{k}\sigma} + \sum_{\mathbf{k}\mathbf{k}'} J \mathbf{S} \mathbf{s}_{\mathbf{k}\mathbf{k}'} = \sum_{\mathbf{k}\sigma} \epsilon_{\mathbf{k}} c_{\mathbf{k}\sigma}^\dagger c_{\mathbf{k}\sigma} + \frac{J}{2} \sum_{\mathbf{k}'\mathbf{k}, \sigma'\sigma} \mathbf{S} c_{\mathbf{k}'\sigma'}^\dagger \vec{\tau}_{\sigma'\sigma} c_{\mathbf{k}\sigma}, \quad (3.2)$$

where \mathbf{S} is the impurity spin and $\vec{\tau} = (\sigma_x, \sigma_y, \sigma_z)^T$ denotes the vector formed by the three Pauli matrices. The exchange coupling J may either be ferromagnetic ($J < 0$) or antiferromagnetic ($J > 0$). The Kondo model describes a bulk of conduction electrons which interact locally via an antiferromagnetic Heisenberg exchange with the impurity spin. If the Kondo model is derived from the SIAM the effective exchange coupling J is related to its parameters via

$$J = V^2 \left(\frac{1}{|\epsilon_d|} + \frac{1}{U + \epsilon_d} \right). \quad (3.3)$$

From there the coupling J is seen to be always antiferromagnetic.

3.4 Kondo Dot Model

The relevant model for the theoretical consideration of this thesis is the so called Kondo dot model where the impurity spin (also known as the Kondo dot) is pinched between two fermionic leads, which are assumed to be thermally equilibrated. However, a finite bias voltage V may be applied between these two leads, which drives the system out of equilibrium and leads to a difference in the chemical potentials $\mu_\alpha = \pm V/2$ ($\alpha = L, R$) of the leads. The occupation distribution of each lead is given by the usual Fermi function $f_\alpha(\epsilon) = 1/(e^{(\epsilon - \mu_\alpha)/T} + 1)$. Additionally the impurity spin may as well be subject to a

finite magnetic field B . Hence, the corresponding Hamiltonian takes the form

$$H = \sum_{\alpha k \sigma} (\epsilon_k - \mu_\alpha) c_{\alpha k \sigma}^\dagger c_{\alpha k \sigma} - g \mu_B B S_z + \frac{1}{2} \sum_{\alpha' \alpha \sigma' \sigma k' k} J_{\alpha' \alpha} \mathbf{S} c_{\alpha' k' \sigma'}^\dagger \vec{\tau}_{\sigma' \sigma} c_{\alpha k \sigma}. \quad (3.4)$$

where \mathbf{S} denotes again the impurity (or Kondo) spin on the quantum dot. As we wish to derive functional renormalization group equations for this model which are based on a diagrammatic calculus we need a representation in terms of fermionic operators for the Kondo spin. Throughout this thesis we shall work in the pseudofermion representation which was introduced by Abrikosov [24, 25]

$$\mathbf{S} = \frac{1}{2} \sum_{\gamma' \gamma} f_{\gamma'}^\dagger \vec{\tau}_{\gamma' \gamma} f_\gamma \quad \text{with} \quad Q = \sum_{\gamma} f_\gamma^\dagger f_\gamma = 1. \quad (3.5)$$

This representation of a spin 1/2 in terms of fermionic operators is further discussed in App. A. The constraint of the pseudo fermion number operator $Q = 1$ originates from the fact, that only the singly occupied fermion states have any physical relevance. Hence, this representation must be supplemented by a projection onto the physical subspace, where double and empty occupied states are excluded. To this end, we introduce a chemical potential λ , whereupon the physically relevant expectation value of an observable \mathcal{O} is obtained as the limiting value

$$\langle \mathcal{O} \rangle_{Q=1} = \lim_{\lambda \rightarrow \infty} \frac{\langle \mathcal{O} Q \rangle_\lambda}{\langle Q \rangle_\lambda}. \quad (3.6)$$

Since λ enters as a chemical potential, thermal averages taken with a finite λ contain various powers of $e^{-\lambda/T}$. In particular, $\langle Q \rangle_\lambda \sim e^{-\lambda/T}$ and hence the limit of $\lambda \rightarrow \infty$ in equ.(3.6) picks out the terms in $\langle \mathcal{O} Q \rangle_\lambda$ which are also proportional to $e^{-\lambda/T}$. Consequently, when calculating any thermal average at finite λ , one is allowed to retain only terms of lowest order in $e^{-\lambda/T}$. In the pseudofermion representation the Kondo dot Hamiltonian takes the form

$$H = \sum_{\alpha k \sigma} (\epsilon_k - \mu_\alpha) c_{\alpha k \sigma}^\dagger c_{\alpha k \sigma} + \sum_{\gamma} \left(\lambda - \gamma \frac{B}{2} \right) f_\gamma^\dagger f_\gamma + \frac{1}{4} \sum_{\alpha' \alpha \sigma' \sigma} J_{\alpha' \alpha} \vec{\tau}_{\sigma' \sigma} \vec{\tau}_{\gamma' \gamma} f_{\gamma'}^\dagger f_\gamma c_{\alpha' \sigma'}^\dagger c_{\alpha \sigma}, \quad (3.7)$$

where we made use of the relation $\sum_k c_{\alpha k \sigma} = c_{\alpha, x=0, \sigma} \equiv c_{\alpha \sigma}$. The interaction is local in space ($x = 0$) and consists of bare interaction processes where a conduction electron is transported either between different leads $\alpha \neq \alpha'$ or the same lead $\alpha = \alpha'$. Coinstantaneously the lead electrons spin is changed from σ' to σ and the spin on the dot is transferred from a state γ' to γ . Such a process conserves spin and furthermore the energy of the “incoming” and “outgoing” particles

$$\sigma + \gamma = \sigma' + \gamma' \quad (3.8)$$

$$\omega_e + \omega_f = \omega_{e'} + \omega_{f'}. \quad (3.9)$$

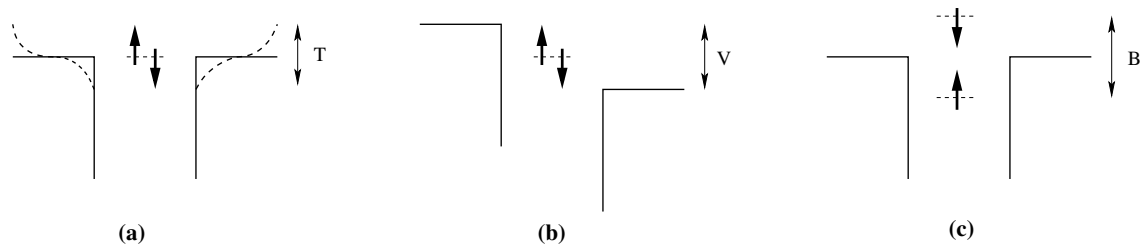


Figure 3.4: Different mechanism leading to an attenuation of the Kondo effect: (a) temperature T destroys the resonance by smearing out the Fermi surface. (b) A voltage V induces a splitting of the Fermi energy of the left and the right lead, which influences either directly or via a voltage induced current-noise the resonant electron scattering. (c) A magnetic field B lifts the degeneracy of the levels on the dot and thus prohibits resonant scattering.

From a total of 16 addends in the spin sum of (3.7) only 6 possibilities remain, which we list for illustration in the subsequent table

	$\sigma \gamma \rightarrow \sigma' \gamma'$	$\vec{T}_{\sigma' \sigma} \vec{T}_{\gamma' \gamma}$
Non Spin Flip	$\uparrow \uparrow \rightarrow \uparrow \uparrow$	1
	$\downarrow \downarrow \rightarrow \downarrow \downarrow$	1
	$\uparrow \downarrow \rightarrow \uparrow \downarrow$	-1
	$\downarrow \uparrow \rightarrow \downarrow \uparrow$	-1
Spin Flip	$\uparrow \downarrow \rightarrow \downarrow \uparrow$	2
	$\downarrow \uparrow \rightarrow \uparrow \downarrow$	2

As described in the previous Section the Kondo effect is most pronounced for vanishing temperature, bias voltage and magnetic field. Whereas each of these three quantities will reduce the Kondo effect the mechanisms are quite different. The temperature T will destroy the Kondo resonance as it smears out the Fermi surface. In case of a finite bias voltage V a splitting of the Fermi energy of the left and the right lead is induced which influences the resonant electron scattering either directly or via a voltage induced current-noise. Finally a magnetic field B will lift the degeneracy of the levels on the Kondo dot which prohibits resonant scattering and thus the emergence of a Kondo resonance. For illumination we have depicted these mechanism in Fig. 3.4.

3.5 Brief History of the Kondo Model

In this subsection we shall give a brief summary of the most important theoretical steps in the long history of the Kondo model. The subsequent sections may be reviewed in [30, 31, 32]. We start from Kondo's second order calculation [4] to find the resistance minimum in dilute magnetic alloys and quote the Kondo problem, i.e. the divergence of his result below the Kondo temperature T_K . Subsequently we explain Anderson's poor man's scaling approach [11] and state the conjectures, that arose from his considerations.

The latter were confirmed by Wilson using the numerical renormalization group [12, 13]. At last we give a synopsis on the effective, analytical low temperature description of the Kondo model by means of a local Fermi liquid originally invented by P. Nozieres [10].

3.5.1 Kondo Effect and Kondo Problem

In dilute magnetic alloys (e.g. *Fe* in *Au* or *Mo-Nb*) the resistivity as a function of the temperature T shows anomalous behavior. Instead of decreasing monotonically down to a residual value ρ_0 (caused by scattering on non-magnetic impurities) the resistivity shows a minimum at a certain temperature which has become known as the Kondo temperature T_K . This behavior is exemplified in Fig. 3.5 for various *Mo-Nb* alloys, which contain 1% *Fe*. In order to calculate the contribution from the spin-spin interaction in

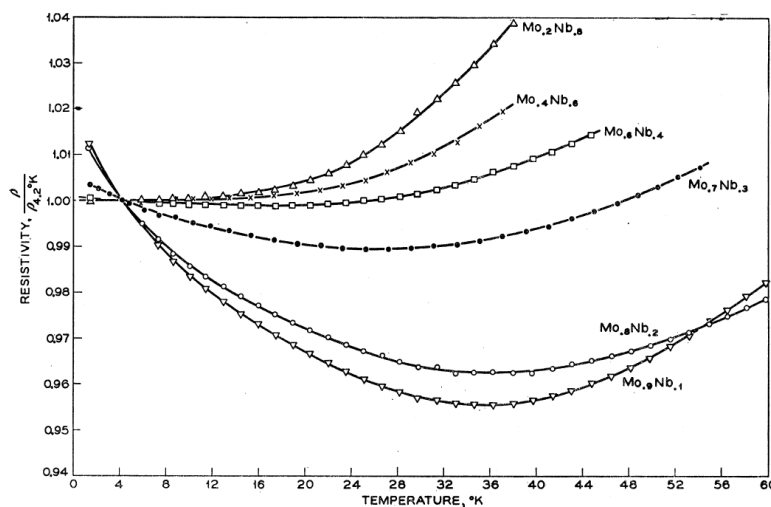


Figure 3.5: Resistivity as a function of temperature for different kinds of *Mo-Nb* alloys containing 1% *Fe*. At 4.2 K the resistivities are normalized [3].

perturbation theory one needs to find the matrix elements $T_{\mathbf{k}\sigma, \mathbf{k}'\sigma'}^{\gamma\gamma'}$ of the T -matrix

$$T = V + V \frac{1}{\epsilon_{\mathbf{k}} - H_0 + i0} V + \dots \quad (3.10)$$

with respect to the basis build up by the states $|\mathbf{k}\sigma, \gamma\rangle \equiv |\mathbf{k}\sigma\rangle \otimes |\gamma\rangle$, i.e. $\langle \mathbf{k}\sigma, \gamma | T | \mathbf{k}'\sigma', \gamma' \rangle$. This matrix elements in turn enter the relaxation time $\tau(\mathbf{k})$ via

$$\frac{1}{\tau(k)} = 2\pi c_{\text{imp}} \int \frac{d^3k'}{(2\pi)^3} \delta(\epsilon_k - \epsilon_{k'}) |T_{\mathbf{k}\mathbf{k}'}|^2 (1 - \cos \Theta'), \quad (3.11)$$

with c_{imp} being the impurity concentration. From there the conductivity is found to be

$$\sigma = -\frac{2e^2}{3} \int \frac{d^3k}{(2\pi)^3} v_k^2 \tau(k) \frac{\partial f}{\partial \epsilon_k}, \quad (3.12)$$

which yields a third order (second order in the T matrix) contribution to the resistivity

$$R_{\text{Kondo}}(T) \propto -\ln(k_B T / D). \quad (3.13)$$

Obviously this results becomes invalid as it diverges as $T \rightarrow 0$, a phenomenon known as the Kondo problem.

3.5.2 Anderson's Poor Man Scaling

The terms leading to a breakdown of the perturbative results come as $\ln(D)$, which signals that the high energy states are important for calculating the low energy excitations and physics. The key idea of Anderson's poor man scaling approach [11] is to successively lower the conduction bandwidth D (at each step by a small amount δD), i.e. to integrate out the high energy states and absorb these in a renormalization of the couplings. A sketch of this renormalization process is depicted in Fig. 3.6. For the

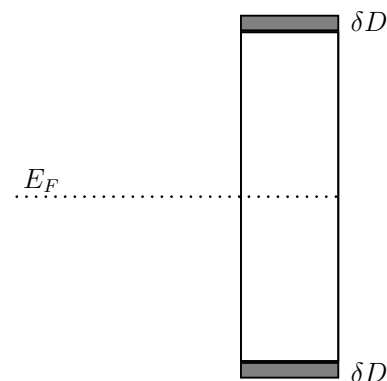


Figure 3.6: Anderson's poor man scaling approach: In each step of the renormalization procedure a small amount of high energy states is removed - thereby the bandwidth reduced by δD - and absorbed in the coupling $J(D)$.

isotropic Kondo model (3.2) the following scaling equation is obtained for $g = N_0 J$

$$\frac{\partial g(D)}{\partial \ln D} = -2g^2(D) \quad \text{with} \quad g(D_0) = g \quad (3.14)$$

with the solution

$$g(D) = \frac{g}{1 - 2g \ln(D_0/D)} = \frac{1}{2 \ln(D/T_K)} \quad (3.15)$$

where the Kondo temperature

$$T_K = D_0 e^{-1/(2g)} \quad (3.16)$$

has been defined. To begin with this result tells us, that the perturbative method becomes invalid as D reaches T_K from above, signaling a breakdown of this scaling approach. However, the solution equ. (3.15) is obtained in the zero temperature limit. If we deal with a finite temperature $T \gg T_K$ the renormalization group flow is cut off at this temperature leading to a renormalized coupling $g(T) = 1/(2 \ln(T/T_K))$. Hence, in the regime $T \gg T_K$ this is the leading term and physical quantities may be calculated by replacing the bare interaction vertex by this renormalized coupling. In Section 5.2.3 we will reconsider this problem and illuminate it in the framework of the functional renormalization group.

However, Anderson suggested that the coupling $g(D)$ even for $T = 0$ should diverge only in the limit $D \rightarrow 0$, i.e. giving a finite result for $0 < D \leq T_K$, a conjecture that was verified by Kenneth G. Wilson using the numerical renormalization group.

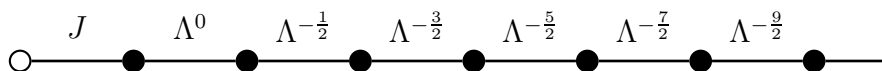


Figure 3.7: Sketch of the approximated form of the tight binding form for the Kondo model (“Wilson-chain”). The impurity spin \mathbf{S} is located to left (open circle) and coupled to the zeroth side in the real space configuration. The sloping hopping elements are shown.

3.5.3 Numerical Renormalization Group

Kenneth G. Wilson [12, 13] was able to affirm the conjecture, that the Kondo model has two fixed points: A stable one for $J = \infty$ and an instable one for $J = 0$. Wilson started from the Kondo model (3.2) which is rewritten by means of a tight binding Hamiltonian where the impurity spin \mathbf{S} is located at one end of the tight binding chain. Mathematically this is achieved by a Lanczos procedure whereupon the conduction electron Hamiltonian is transferred from diagonal to tridiagonal form, i.e. $H_c = \sum_{n=0\sigma}^{\infty} \epsilon_n c_{n\sigma}^\dagger c_{n\sigma} + (\gamma_n c_{n+1\sigma}^\dagger c_{n\sigma} + h.c.)$. The first approximation is to choose a particular form of ϵ_n and γ_n (see below). Secondly—as a starting point for the renormalization group procedure—the chain is kept finite, i.e. it consists of N conduction electrons. The corresponding Hamiltonian takes the following form

$$H_N = \frac{D(1 + \Lambda^{-1})}{2} \sum_{n=0,\sigma}^{N-1} \Lambda^{-n/2} \left(c_{n\sigma}^\dagger c_{n+1\sigma} + c_{n+1\sigma}^\dagger c_{n\sigma} \right) + J \sum_{\sigma'\sigma} \mathbf{S} c_{0\sigma'}^\dagger \vec{\tau}_{\sigma'\sigma} c_{0\sigma} \quad (3.17)$$

and is illustrated in Fig. 3.7. Based on the Hamiltonian H_N Wilson sets up the following iterative scheme

$$\tilde{H}_N \equiv \frac{2}{D(1 + \Lambda^{-1})} \Lambda^{(N-1)/2} H_N \quad (3.18)$$

$$\tilde{H}_{N+1} = \Lambda^{1/2} \tilde{H}_N + \sum_{\sigma} c_{N\sigma}^\dagger c_{N+1\sigma} + c_{N+1\sigma}^\dagger c_{N\sigma} \equiv R(\tilde{H}_N) \quad (3.19)$$

Equ. (3.19) defines a sequence of renormalization group transformations (denoted by R). The successive stages in the iterative diagonalization are:

- (i) Diagonalize, i.e. find the energy levels of \tilde{H}_N , starting from a single side coupled to the local spin ($N=0$).
- (ii) Rescale the energy levels by multiplying with $\Lambda^{1/2}$ (according to equ. (3.19))
- (iii) Add one more side to the chain, i.e. a set of states $\{|0, 0\rangle, |\uparrow, 0\rangle, |0, \downarrow\rangle, |\uparrow, \downarrow\rangle\}$.

These steps are repeated while only a certain number N_0 corresponding to the lowest levels of \tilde{H}_{N+1} is kept at each stage.

How did Wilson confirm the conjecture of the two fixed points named above? First off all one has to note that for $J = 0$ the impurity is completely uncoupled from the dot and

the excitations are therefore given by the ones of a tight binding chain (ranging from 0 to N). On contrary for $J = \infty$ the impurity is indefinitely strong coupled to the first side, effectively removing it from the chain. The excitations in this case are then given by the ones of a tight binding chain ranging from 1 to N . Hence, the conjecture turns into the statement that the low energy excitations of $\tilde{H}_N(J = \infty)$ are the same as for $\tilde{H}_{N-1}(J = 0)$. Wilson was able to show that the values of the lowest excitation energies for $\Lambda = 2$ and small $J = 0.009$ for even and large N approach the values corresponding to the $J = \infty$ fixed point.

3.5.4 Local Fermi Liquid Picture

Regarding physical quantities like the resistivity or conductance (according to which Kondo system is under consideration) the physics for $T \gg T_K$ was well understood. For the properties well below T_K Nozieres [10] provided a description by means of a local Fermi liquid. The key idea was to take as granted that for low temperature the coupling between the conduction electrons and the impurity spin is infinitely strong, leaving effectively a non-magnetic and repulsive impurity. In other words at $T = 0$ the local spin binds one electron from the band into a singlet whereupon the other electrons form a Fermi liquid for which the impurity acts as a potential scatterer, inducing phase shifts only, i.e. causing only elastic scattering of bulk electrons. Due to this point like, momentum independent coupling it is sufficient to consider s -wave scattering only. At zero temperature the corresponding phase shift $\delta(\epsilon_F)$ is at resonance, i.e. $\delta(\epsilon_F) = \pi/2$. Hence the resistivity or conductance, respectively reaches the unitarity limit

$$G = G_0 = \frac{2e^2}{h} \quad \text{for } T = 0. \quad (3.20)$$

If we reside near by zero temperature, i.e. for $T \neq 0$ but still $T \ll T_K$ the coupling between the impurity and the lead electrons is still huge but finite, thus allowing also for inelastic collisions. The corresponding inelastic relaxation rate has to be added in delicate way (i.e. one has to take care of a diminishment of the elastic scattering rate since inelastic scattering processes remove particles from the elastic channel) and gives finally rise to a temperature dependence of the following form

$$G(T) = G_0 \left(1 - \frac{\pi^4 w}{16} \left(\frac{T}{T_K} \right)^2 \right) \quad \text{for } T \ll T_K, \quad (3.21)$$

with the Wilson number $w \approx 0.4107$. The quadratic temperature dependence of equ. (3.21) is characteristic for Fermi liquid results. Here the Kondo temperature T_K is defined by the zero temperature susceptibility $\chi_0 = \frac{1}{4T_K}$. The form equ. (3.21) has nowadays been well established by experiment [22] and is discussed in more detail in Chapter 6.

4 Equilibrium and Nonequilibrium Functional Renormalization Group Method

4.1 Introduction

The functional renormalization group is an ideal tool when dealing with the diversity of energy scales and the interplay of correlations in interacting fermionic systems such as the Kondo model where the bandwidth D and the correlation induced Kondo temperature T_K differ by orders of magnitude. Via a field theoretical approach an exact infinite hierarchy of flow equations is obtained, which yields the gradual evolution from a microscopic model Hamiltonian to the effective action as a function of a continuously decreasing energy cutoff. Practically one modifies the bare propagator by cutting off frequencies smaller than some infrared cutoff Λ . As this cutoff is progressively lowered more and more low-energy degrees of freedom are included, until the original model is recovered for $\Lambda \rightarrow 0$. In applications the main approximation consists of a suitable truncation of the hierarchy.

Starting from a small introduction to the basic notion of path integrals in Section 4.2 we introduce the equilibrium FRG and give a detailed derivation of the FRG flow equations in Section 4.3. In the literature there exist quite a number of publications which review and deepen this Section. From purely technical and conceptual introductions [33, 34], various correlated electrons systems have been studied using the equilibrium FRG formalism such as the two-dimensional Hubbard model [34, 35], Luttinger liquids with impurities [34, 36, 37, 38], the single-impurity Anderson model [39] and electron transport through correlated quantum dots [37, 40, 41]. In the subsequent Section 4.4 we review the Keldysh formalism, a real-time technique introduced by L. Keldysh [16] for the treatment of physical systems out of equilibrium. The main difference compared to equilibrium diagrammatic techniques, like the $T = 0$ or the Matsubara formalism manifests itself in the matrix or tensor structure for the Green or the vertex functions, respectively. We introduce the two common representations when dealing with Keldysh diagrams, the contour ordered and the Keldysh rotated representation. A general analysis of the properties of multi-particle Green and vertex functions within the Keldysh formalism can be found in [42]. Especially for the Kondo model we state the bare propagators for the lead electrons and the pseudo fermions and relate their various components and self-energy parts. Furthermore we give a short abstract on the structure of the bare interaction vertex at the end of this Section. Having these two ingredients—the equi-

librium FRG and the Keldysh technique—at hand in Section 4.5 we then briefly extend in a first step the FRG to nonequilibrium. The extension of the FRG concept to non equilibrium systems can be as well found either by Gezzi *et. al.* [43] where the authors use a path integral formulation and study the single two lead impurity Anderson model out equilibrium or by Jakobs *et. al.*[44, 45], where they use a diagrammatic approach to obtain FRG flow equations and apply it to a quantum wire with contact barriers. In a second step we give a rather detailed derivation of the nonequilibrium flow equations for the particular case of the Kondo dot model. We choose to build in the cutoff function in the bare propagator for the lead electrons and neglect the self energy part of those completely. The corresponding differential equation system is stated up to second order in the 1PI vertex functions, i.e. it contains flow equations for the pseudo fermion self energy and the two particle vertex function.

4.2 Functional Formalism and Generating Functionals

Path integrals have a long history in quantum mechanics and quantum field theory. As a starting point one may consider the question to find the transition probability for a single particle in one dimension, governed by a time independent Hamiltonian $H = \frac{p^2}{2m} + V(r)$ to propagate from (x_i, t_i) to (x_f, t_f) which is given by

$$U(x_f t_f; x_i t_i) = \langle x_f | e^{-iH(t_f - t_i)} | x_i \rangle. \quad (4.1)$$

Following standard textbook techniques [46, 47] the key steps to obtain the path integral representation for the transition probability $U(x_f t_f; x_i t_i)$ may be summarized as follows: To begin with one divides the time interval $(t_f - t_i)$ in M equal steps $\epsilon = \frac{t_f - t_i}{M}$ and then inserts $(M - 1)$ times the closure relation $1 = \int |x_j\rangle \langle x_j|$ ($j = 1, \dots, M - 1$). Next one finds an appropriate approximation for the matrix element $\langle x_j | e^{-i\epsilon H} | x_{j-1} \rangle$ and finally takes the limit $M \rightarrow \infty$. As a result one is left with the expression

$$U(x_f t_f; x_i t_i) = \int_{(x_i, t_i)}^{(x_f, t_f)} D[x(t)] e^{iS[x(t)]}, \quad (4.2)$$

where

$$\int_{(x_i, t_i)}^{(x_f, t_f)} D[x(t)] = \lim_{M \rightarrow \infty} \int \prod_{j=1}^{M-1} dx_j \left(\frac{m}{2\pi i \epsilon} \right)^{\frac{3M}{2}} \quad (4.3)$$

represents the sum over all trajectories that start at (x_i, t_i) and end at (x_f, t_f) . In the path integral representation (4.2) the action $S[x(t)]$ is given by the time integrated Lagrangian of the system

$$S[x(t)] = \int_{t_i}^{t_f} dt L[x(t)] \quad \text{with} \quad L[x(t)] = \frac{m}{2} \left(\frac{dx}{dt} \right)^2 - V(x(t)). \quad (4.4)$$

Hence the transition probability U may be interpreted as the sum over all trajectories from the initial (x_i, t_i) to the end point (x_f, t_f) , weighted with the exponential e^{iS} . (Remark: The classical trajectory $x_{cl}(t)$ would minimize the action S . Even in the quantum situation the main contributions stems from this classical path, all other trajectories $x(t) = x_{cl}(t) + \delta x(t)$ interfere and cancel each other.)

This setup scheme for the simple Feynman path integral is a common feature as well for more sophisticated path integral representations as for interacting quantum many body systems. In this context the first observation towards a path integral representation is that the the partition function $Z = \text{Tre}^{-\beta H} = \int \langle x | e^{-\beta H} | x \rangle$ with $\beta = 1/T$ has a functional integral representation, which can be either derived in a straightforward way by setting $\beta = i(t_f - t_i) \equiv \tau_f - \tau_i$ and performing the same steps as described above or by performing an analytic continuation of ((4.2)) to the imaginary time by setting $t = -i\tau$, which is known as Wick rotation.

For a fermionic quantum many body system the partition function can be written as [46]

$$Z = \frac{1}{Z_0} \int D[\bar{\psi}, \psi] \exp\{(\bar{\psi}, G_0^{-1}\psi) - V(\bar{\psi}, \psi)\} \quad (4.5)$$

with the interaction part

$$V(\bar{\psi}, \psi) = \sum_{k'_1, k'_2, k_1, k_2} v_{k'_1, k'_2, k_1, k_2} \bar{\psi}_{k'_1} \bar{\psi}_{k'_2} \psi_{k_2} \psi_{k_1} \quad (4.6)$$

and the non-interacting partition function

$$Z_0 = \int D[\bar{\psi}, \psi] \exp\{(\bar{\psi}, G_0^{-1}\psi)\}. \quad (4.7)$$

The combined indices $k_i^{(l)}$ represent the quantum numbers of the considered one particle basis (e.g. momenta, frequency, spin, lead index, etc.). $\bar{\psi}$ and ψ denote Grassmann fields (cf. App. B). Furthermore the following short hand notation

$$(\bar{\psi}, G_0^{-1}\psi) = \sum_{k', k} \bar{\psi}_{k'} [G_0^{-1}]_{k', k} \psi_k \quad (4.8)$$

has been introduced. This may again be interpreted as follows: The integration over all possible field configurations weighted with a Boltzmann factor (e^{-S}) redisplayes the trace over the Boltzmann weight $e^{-\beta(H-\mu N)}$. That fact, that we are dealing with a fermionic system is contained in the algebra of the Grassmann fields which is discussed in App. B. By adding source fields in the exponent one obtains the generating functional for the n -particle Green functions

$$\mathcal{G}(\bar{\eta}, \eta) = \frac{1}{Z_0} \int D[\bar{\psi}, \psi] \exp\{(\bar{\psi}, G_0^{-1}\psi) - V(\bar{\psi}, \psi) - (\bar{\psi}, \eta) - (\bar{\eta}, \psi)\}. \quad (4.9)$$

Singling out the connected Green functions is achieved by taking the logarithm

$$\mathcal{W}(\bar{\eta}, \eta) = \ln [\mathcal{G}(\bar{\eta}, \eta)] . \quad (4.10)$$

By taking functional derivatives with respect to the source fields one obtains the fully dressed connected Green functions

$$G_n(k'_1, \dots, k'_n; k_1, \dots, k_n) = \frac{\partial^n}{\partial \bar{\eta}_{k'_1} \dots \partial \bar{\eta}_{k'_n}} \frac{\partial^n}{\partial \eta_{k_n} \dots \partial \eta_{k_1}} \mathcal{W}(\bar{\eta}, \eta) \Big|_{\bar{\eta}=\eta=0}. \quad (4.11)$$

If we introduce the Grassmann fields

$$\chi = -\frac{\partial \mathcal{W}(\bar{\eta}, \eta)}{\partial \bar{\eta}} \quad \text{and} \quad \bar{\chi} = \frac{\partial \mathcal{W}(\bar{\eta}, \eta)}{\partial \eta} \quad (4.12)$$

and subsequently perform a Legendre transformation

$$\Gamma(\bar{\chi}, \chi) = -W(\bar{\eta}, \eta) - (\bar{\chi}, \eta) - (\bar{\eta}, \chi) + (\bar{\chi}, G_0^{-1} \chi) \quad (4.13)$$

we finally arrive at the generating functional for the one-particle irreducible n -particle vertex functions γ_n , which are again obtained by taking derivatives with respect the source fields

$$\gamma_n(k'_1, \dots, k'_n; k_1, \dots, k_n) = \frac{\partial^n}{\partial \bar{\chi}_{k'_1} \dots \partial \bar{\chi}_{k'_n}} \frac{\partial^n}{\partial \chi_{k_n} \dots \partial \chi_{k_1}} \Gamma(\bar{\chi}, \chi) \Big|_{\bar{\chi}=\chi=0}. \quad (4.14)$$

There exists an important relation between the second functional derivatives of Γ and \mathcal{W} with respect to particular source fields [46], which will prove to be an essential ingredient for deriving the FRG flow equations

$$\begin{pmatrix} \frac{\partial^2 \Gamma}{\partial \bar{\chi} \partial \chi} + G_0^{-1} & \frac{\partial^2 \Gamma}{\partial \bar{\chi} \partial \bar{\chi}} \\ \frac{\partial^2 \Gamma}{\partial \chi \partial \bar{\chi}} & \frac{\partial^2 \Gamma}{\partial \chi \partial \chi} - G_0^{-1} \end{pmatrix} \begin{pmatrix} \frac{\partial^2 \mathcal{W}}{\partial \bar{\eta} \partial \eta} & -\frac{\partial^2 \mathcal{W}}{\partial \bar{\eta} \partial \bar{\eta}} \\ -\frac{\partial^2 \mathcal{W}}{\partial \eta \partial \bar{\eta}} & \frac{\partial^2 \mathcal{W}}{\partial \eta \partial \eta} \end{pmatrix} = \mathbf{1}. \quad (4.15)$$

If we now put the source fields to zero and furthermore assume that the physical system under consideration is not in any symmetry-breaking phase, i.e. the off diagonals in both matrices in equ. (4.15) vanish, we obtain

$$G_1 = \frac{\partial \mathcal{W}}{\partial \bar{\eta} \partial \eta} \Big|_{\bar{\eta}=\eta=0} = \left(\frac{\partial^2 \Gamma}{\partial \bar{\chi} \partial \chi} + G_0^{-1} \right)^{-1} = (G_0^{-1} + \gamma_1)^{-1}. \quad (4.16)$$

If we compare this with the usual Dyson equation $G = (G_0^{-1} - \Sigma)^{-1}$ we conclude

$$\Sigma = -\gamma_1. \quad (4.17)$$

4.3 Equilibrium Functional Renormalization Group

In this chapter we will give a detailed derivation of the FRG flow equations. For the purpose of our work on the Kondo dot model it is sufficient to consider propagators which only depend on frequency. The setup of the FRG flow equations is based on the following modification of the bare propagator G_0 : It is replaced by a cutoff dependent propagator G_0^Λ , such that for some Λ_0 the bare Green function $G_0^{\Lambda_0}$ vanishes, whereas

for $\Lambda = 0$ one obtains $G_0^{\Lambda=0} = G_0$. To put this modification in words, one might say that for $\Lambda = \Lambda_0$ no degrees of freedom or modes are turned on while at $\Lambda = 0$ one recovers the cutoff independent problem. One particular choice is a sharp frequency cutoff of the form

$$G_0^\Lambda(\omega) = G_0(\omega)\Theta(|\omega| - \Lambda). \quad (4.18)$$

Another possible choice is a smooth cutoff which might be chosen as

$$G_0^\Lambda(\omega) = G_0(\omega) \left(\frac{1}{2} + \frac{1}{\pi} \arctan \left(\frac{|\omega| - \Lambda}{b} \right) \right). \quad (4.19)$$

In this choice the Θ function of equ. (4.18) is broadened on a scale b .

Both of these two particular cutoff choices turn out to have advantages and disadvantages. The sharp cutoff is seen to simplify matters insofar, as it leaves no internal integration in the diagrams appearing on the r.h.s. of the FRG flow equation, but it might lead to instabilities, e.g. by neglecting self energy effects (especially the imaginary part) or dealing with small self energy contributions one faces the treatment of sharp and peaked functions. This deficiency can be repaired—at least to some extent—by choosing a smooth cutoff and paying the price of an extra integration, i.e. a numerically more expensive treatment of the FRG equations.

By choosing a cutoff dependent bare propagator in the action of the generating functionals these (i.e. equ. (4.9), (4.10) and (4.13)) become functions of the cutoff Λ as well. The first step towards the FRG flow equation hierarchy is obtained by taking the derivative of \mathcal{W}^Λ with respect to Λ . This yields

$$\frac{d}{d\Lambda} \mathcal{W}^\Lambda = -\text{Tr} (Q^\Lambda G_0^\Lambda) + \text{Tr} \left(Q^\Lambda \frac{\partial \mathcal{W}^\Lambda}{\partial \bar{\eta} \eta} \right) - \left(\frac{\partial \mathcal{W}^\Lambda}{\partial \eta}, Q^\Lambda \frac{\partial \mathcal{W}^\Lambda}{\partial \bar{\eta}} \right), \quad (4.20)$$

where we introduced the Λ -derivative of the free inverse propagator

$$Q^\Lambda = \frac{d}{d\Lambda} (G_0^\Lambda)^{-1}. \quad (4.21)$$

With the aid of equ. (4.20) we may now proceed differentiating the Λ -dependent functional for the 1PI vertex functions Γ^Λ (cf. equ. (4.13)) to obtain

$$\frac{d}{d\Lambda} \Gamma^\Lambda = \text{Tr} (Q^\Lambda G_0^\Lambda) - \text{Tr} (G^\Lambda Q^\Lambda R_{11}), \quad (4.22)$$

where R_{11} denotes the upper left block of the matrix

$$R = \sum_{n=0}^{\infty} \begin{pmatrix} -G^\Lambda & 0 \\ 0 & G^\Lambda \end{pmatrix} \begin{pmatrix} \frac{\partial^2 \Gamma}{\partial \bar{\chi} \partial \chi} & \frac{\partial^2 \Gamma}{\partial \bar{\chi} \partial \bar{\chi}} \\ \frac{\partial^2 \Gamma}{\partial \chi \partial \chi} & \frac{\partial^2 \Gamma}{\partial \chi \partial \bar{\chi}} \end{pmatrix}. \quad (4.23)$$

If we finally expand the Γ^Λ in the external sources with the 1PI vertex functions as expansion coefficients

$$\Gamma^\Lambda(\bar{\chi}, \chi) = \sum_{n=0}^{\infty} \frac{(-1)^n}{(n!)^2} \gamma^\Lambda(k'_1, \dots, k'_n; k_1, \dots, k_n) \bar{\chi}_{k'_1} \cdots \bar{\chi}_{k'_n} \chi_{k_n} \cdots \chi_{k_1} \quad (4.24)$$

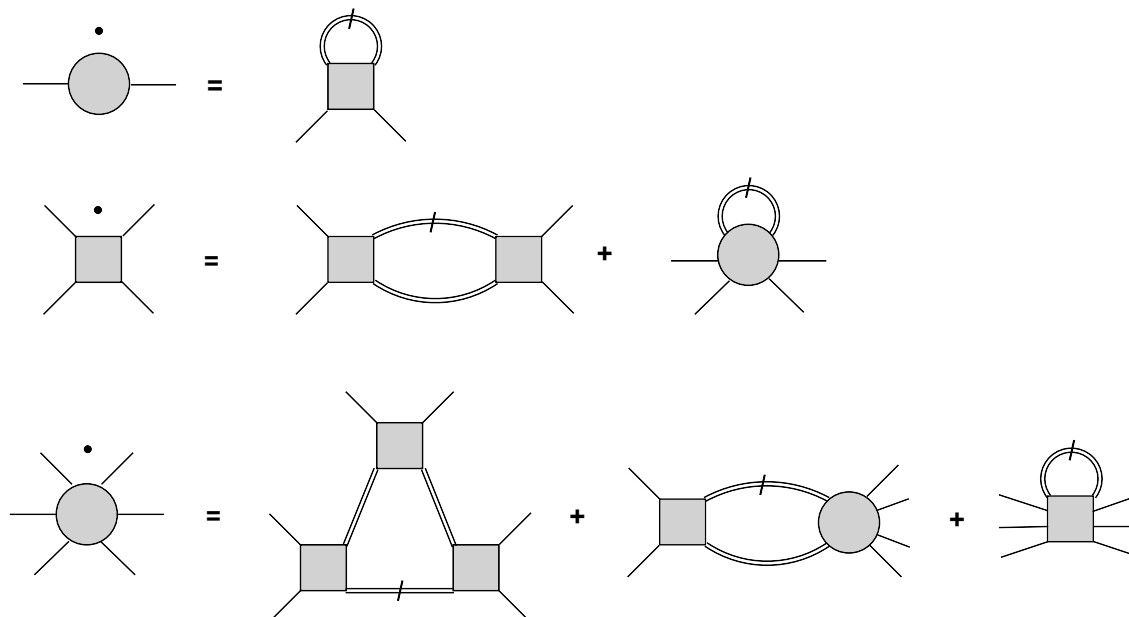


Figure 4.1: Graphical representation of the FRG flow equations for the first three 1PI vertex functions. The dot on the left hand side denotes the derivate with respect to the cutoff Λ . Propagatos containing a stroke on the right hand side represent the single scale propagator S^Λ as defined in equ. 4.27.

we arrive at the desired hierarchy of coupled flow equations. The first three of these flow equations are depicted graphically in Fig. 4.1. Only for the two lowest orders $n = 1$ and $n = 2$, i.e. for the self energy and the vertex function, which is often referred to as the effective interaction we write down these flow equations explicitly.

$$\partial_\Lambda \Sigma^\Lambda(k'_1 k_1) = -\frac{1}{\beta} \sum_{k_2, k'_2} S^\Lambda(k_2, k'_2) \gamma_2^\Lambda(k'_1, k'_2; k_1, k_2) \quad (4.25)$$

$$\begin{aligned} \partial_\Lambda \gamma_2^\Lambda(k'_1, k'_2; k_1, k_2) &= \frac{1}{\beta} \sum_{k_3, k'_3} \sum_{k_4, k'_4} G^\Lambda(k_3, k'_3) S^\Lambda(k_4, k'_4) [\gamma_2^\Lambda(k'_1, k'_2; k_3, k_4) \gamma_2^\Lambda(k'_3, k'_4; k_1, k_2) \\ &\quad - \gamma_2^\Lambda(k'_1, k'_4; k_1, k_3) \gamma_2^\Lambda(k'_3, k'_2; k_4, k_2) + \gamma_2^\Lambda(k'_2, k'_4; k_1, k_3) \gamma_2^\Lambda(k'_3, k'_1; k_4, k_2) \\ &\quad + (k_3 \leftrightarrow k_4, k'_3 \leftrightarrow k'_4)] \end{aligned} \quad (4.26)$$

where the first term on the right hand side of the equation for the vertex function represents the particle-particle channel and the following two the particle-hole channels, respectively. The last bracket indicates that the two two previous terms have to be repeated with changes of indices as declared. Furthermore we have introduced the so-called single-scale propagator

$$S^\Lambda = G^\Lambda Q^\Lambda G^\Lambda. \quad (4.27)$$

There is a technical detail and a significantly simplification of the FRG flow equations regarding this object: if we choose the sharp frequency cutoff (4.18) the integrals on the

right hand side of the flow equations can be performed analytically. The propagators contain both $\Theta(|\omega| - \Lambda)$ and $\delta(|\omega| - \Lambda) = -\partial_\Lambda \Theta(|\omega| - \Lambda)$ functions, which at a first look seems to be ambiguous, because the Θ -function has a discontinuity precisely where the δ -function has support. This ambiguity, however, becomes well defined and unique if the sharp cutoff is implemented as a limit of increasingly broadened cutoff function $\Theta_b(\omega)$ (cf. equ. (4.19)), with the broadening parameter b tending to zero. Using the following relation introduced by Morris [48]

$$\delta_b(x - \Lambda)f(\Theta_b(x - \Lambda)) \rightarrow \delta(x - \Lambda) \int_0^1 f(t)dt \quad (4.28)$$

which is valid for an arbitrary continuous function f , the expression on the right hand of the FRG equation may be conventionally evaluated. For the establishment of the boundary conditions we may either use the relation

$$\Gamma^{\Lambda_0}(\bar{\chi}, \chi) = V(\bar{\chi}, \chi), \quad (4.29)$$

which is proved in a lengthy but straightforward calculation or by the following diagrammatic and less systematic argument: For $\Lambda = \Lambda_0$ no modes are “turned on”, i.e. $G_0^{\Lambda_0} = 0$, such that in the diagrammatic expressions for the n -particle vertex functions only the bare interaction vertices remain. Thus for $\Lambda = \Lambda_0$ we have the conditions

$$\gamma_1(k', k) = -\Sigma(k', k) = v_{k', k}^p \quad (4.30)$$

$$\gamma_2(k'_1, k'_2; k_1, k_2) = v_{k'_1, k'_2; k_1, k_2} \quad (4.31)$$

$$\gamma_n(k'_1, \dots, k'_n; k_1, \dots, k_n) = 0 \quad \text{for } m \geq 3, \quad (4.32)$$

where v^p denotes a bare single-particle potential scattering term, possibly present in the Hamiltonian under consideration. The bare, antisymmetrized two-particle interaction v was introduced in equ. (4.6). In the absence of any higher order bare interaction vertices (e.g. three-particle interaction) the flow of the vertex functions γ_n with $n \geq 3$ starts at zero.

4.4 Keldysh Formalism and Propagators for the Kondo Dot Model

The whole equilibrium and $T = 0$ diagrammatic apparatus is inter alia based on the adiabatic hypothesis: Starting from the ground state of the non-interacting system at $t = -\infty$ and then switching on and off the perturbation (external potential, two-body interaction) adiabatically the systems is supposed to reach at $t = \infty$ again—up to some phase factor—its ground state, $e^{i\alpha}|0\rangle$.

In a nonequilibrium situation, as well as for $T \neq 0$ this assumption is no longer justified, since the final state consists of some superposition of excited states, i.e. the system evolves to some unpredictable state. To avoid this problem Schwinger suggested to take

the final state to be exactly the same as the initial one. That is one first let the the quantum system evolve in the forward direction in time and then reverses its time evolution, opposing its time direction. In other words, one extends the time contour, which—in the $T = 0$ formalism— consists of a simple forward branch, to a two-branch time contour \mathcal{C} , consisting of a forward branch \mathcal{C}_1 and a backward branch \mathcal{C}_2 . This contour \mathcal{C} is most often called Schwinger-, Keldysh- oder Keldysh-Schwinger-contour and is depicted in Fig. 4.2. This suggestion overcomes the above stated problem with the adiabatic hypothesis

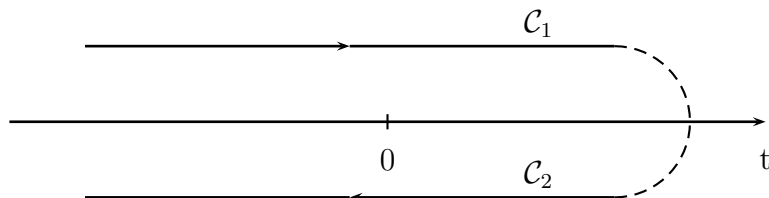


Figure 4.2: The Schwinger-contour consisting of a forward branch \mathcal{C}_1 and a backward branch \mathcal{C}_2 .

and allows for a usual diagrammatic treatment [49, 50, 51, 52, 46, 53, 54] of interacting quantum systems in the common sense. This advantage, however comes with a certain price: By doubling the time contour one automatically doubles the degrees of freedom. As shown subsequently the Green (and also higher correlation function) acquire an additional index structure, i.e. become matrices (or tensors) in the Keldysh-space.

4.4.1 Green Functions

The Green function within the Keldysh formalism is defined as usual by

$$G(r, t; r', t') = -i \langle T_{\mathcal{C}} \psi(r, t) \psi^\dagger(r', t') \rangle, \quad (4.33)$$

where $T_{\mathcal{C}}$ is the time-ordering operator with respect to the contour \mathcal{C} . There are four possibilities for the pair (t, t') to reside on the two branches of the Keldysh contour \mathcal{C} , which are explicitly given by

$$G(r, t; r', t') = \begin{cases} -i \langle T \psi(r, t) \psi^\dagger(r', t') \rangle & t \in \mathcal{C}_1, t' \in \mathcal{C}_1 \\ i \langle \psi^\dagger(r', t') \psi(r, t) \rangle & t \in \mathcal{C}_1, t' \in \mathcal{C}_2 \\ -i \langle \psi(r, t) \psi^\dagger(r', t') \rangle & t \in \mathcal{C}_2, t' \in \mathcal{C}_1 \\ -i \langle \tilde{T} \psi(r, t) \psi^\dagger(r', t') \rangle & t \in \mathcal{C}_2, t' \in \mathcal{C}_2 \end{cases}. \quad (4.34)$$

If both time arguments lie on the the forward branch \mathcal{C}_1 one obtains the usual time-ordered Green function $G^T(t, t')$, whereas if both time arguments lie on the backward

branch \mathcal{C}_2 one deals with the anti-time-ordered Green function $G^{\tilde{T}}(t, t')$. In the case where $t \in \mathcal{C}_1$ and $t' \in \mathcal{C}_2$, then always $t < t'$ and one obtains the lesser Green function $G^<(t, t')$, whereas in the case $t \in \mathcal{C}_2$ and $t' \in \mathcal{C}_1$, then always $t > t'$ and one ends up with the greater Green function $G^>(t, t')$.

This structure of the Green function regarding the Keldysh contour suggests to introduce indices $i, j \in \{1, 2\}$ with $t \in \mathcal{C}_i$ and $t' \in \mathcal{C}_j$ and to arrange the various components of the Green function in a matrix form

$$G(t, t') = \begin{pmatrix} G^T(t, t') & G^<(t, t') \\ G^>(t, t') & G^{\tilde{T}}(t, t') \end{pmatrix}_{ij}. \quad (4.35)$$

Furthermore it is convenient and will subsequently turn out to be an useful representation to introduce the advanced, the retarded and in addition the Keldysh Green function by

$$\begin{aligned} G^R(t, t') &= -i\Theta(t - t')\langle\{\psi(t), \psi^\dagger(t')\}\rangle \\ G^A(t, t') &= +i\Theta(t' - t)\langle\{\psi(t), \psi^\dagger(t')\}\rangle \\ G^K(t, t') &= -i\langle[\psi(t), \psi^\dagger(t')]\rangle. \end{aligned} \quad (4.36)$$

This functions are related to the contour Keldysh Green function via

$$\begin{aligned} G^R &= G^T - G^< = G^> - G^{\tilde{T}} \\ G^A &= G^T - G^> = G^< - G^{\tilde{T}} \\ G^K &= G^< + G^> = G^T + G^{\tilde{T}}. \end{aligned} \quad (4.37)$$

One of the major properties of the four contour Green functions is, that they are not independent. For $t \neq t'$ one may simply prove, that the following relation holds:

$$G^T(t, t') + G^{\tilde{T}}(t, t') = G^<(t, t') + G^>(t, t'). \quad (4.38)$$

Due to the relation equ. ((4.38)) one component of G^{ij} is redundant. This redundancy can be removed by a appropriate transformation, which was introduced by L. Keldysh [16] and its named after its originator Keldysh rotation. We will actually follow the notation and convention by Rammer and Smith [53] and deal with the following rotation matrices

$$L = \frac{1}{\sqrt{2}} \begin{pmatrix} 1 & 1 \\ 1 & -1 \end{pmatrix} \quad \text{and} \quad L^\dagger = \frac{1}{\sqrt{2}} \begin{pmatrix} 1 & 1 \\ -1 & 1 \end{pmatrix}. \quad (4.39)$$

Performing the rotation we obtain a new representation of the Keldysh matrix given by

$$G_K = (LGL^\dagger) = \begin{pmatrix} G_R & G^K \\ 0 & G_A \end{pmatrix}_{ij}. \quad (4.40)$$

Apart from the fact that the Green function is a matrix in the present formalism the relation to its 1PI part, i.e. the self energy part is identical to the equilibrium case and given by the usual Dyson equation

$$G = ((G^0)^{-1} - \Sigma)^{-1}. \quad (4.41)$$

Here G denotes the fully dressed and G_0 the bare Green function. The self energy part Σ has—in the contour representation—the same structure as the Green function itself and a similar redundancy-equation as equ. (4.38) holds

$$\Sigma = \begin{pmatrix} \Sigma^T & \Sigma^< \\ \Sigma^> & \Sigma^{\tilde{T}} \end{pmatrix}, \quad \Sigma^T + \Sigma^< + \Sigma^> + \Sigma^{\tilde{T}} = 0. \quad (4.42)$$

After performing the Keldysh rotation the self energy matrix takes the same form as equ. (4.40) for the Green function

$$\Sigma = \begin{pmatrix} \Sigma^R & \Sigma^K \\ 0 & \Sigma^A \end{pmatrix}. \quad (4.43)$$

Again we state the relations of the self energy components in the contour and the Keldysh rotated representation

$$\Sigma^R = \Sigma^T + \Sigma^< \quad (4.44)$$

$$\Sigma^A = \Sigma^T + \Sigma^> \quad (4.45)$$

$$\Sigma^K = \Sigma^T + \Sigma^{\tilde{T}}. \quad (4.46)$$

In the Keldysh rotated representation the Dyson equation may be written in the following component-wise form

$$G^R = ((G^{0,R})^{-1} - \Sigma^R)^{-1} \quad (4.47)$$

$$G^A = ((G^{0,A})^{-1} - \Sigma^A)^{-1} \quad (4.48)$$

$$G^K = G^R \Sigma^K G^A. \quad (4.49)$$

Further useful rules, which will be used in the following chapters of this work are

$$(\Sigma^R)^* = \Sigma^A, \quad (\Sigma^K)^* = -\Sigma^K \quad (4.50)$$

$$(\Sigma^<)^* = -\Sigma^<, \quad (\Sigma^>)^* = -\Sigma^>, \quad (\Sigma^T)^* = -\Sigma^{\tilde{T}}. \quad (4.51)$$

For later use we state at this point the bare propagators of the lead electrons and the pseudo fermion for the Kondo dot model. For the leads, which we assume to be in thermal equilibrium the bare Green function carries a lead index $\alpha = L, R$ and is only dependent on frequency, since the interaction is local and thus all momentum dependence can be integrated out. We assume a constant density of states in a band of width $2D = N_0^{-1}$, i.e.

$$N(\omega) = N_0 \Theta(D - \omega). \quad (4.52)$$

Furthermore (if the leads are not subject to any magnetic field) the lead electron Green functions do not depend on spin. The various components in the contour representation

are given by

$$G_{\alpha}^{0,<}(\omega) = 2\pi i f_{\alpha}(\omega) N_0 \Theta(D_0 - |\omega|) \quad (4.53)$$

$$G_{\alpha}^{0,>}(\omega) = -2\pi i (1 - f_{\alpha}(\omega)) N_0 \Theta(D_0 - |\omega|) \quad (4.54)$$

$$G_{\alpha}^{0,T}(\omega) = \frac{N_0}{2} \ln \left| \frac{\omega + D_0}{\omega - D_0} \right| - i\pi \tanh \left(\frac{\omega - \mu_{\alpha}}{2T} \right) N_0 \Theta(D_0 - |\omega|) \quad (4.55)$$

$$G_{\alpha}^{0,\tilde{T}}(\omega) = -\frac{N_0}{2} \ln \left| \frac{\omega + D_0}{\omega - D_0} \right| - i\pi \tanh \left(\frac{\omega - \mu_{\alpha}}{2T} \right) N_0 \Theta(D_0 - |\omega|). \quad (4.56)$$

Here $f_{\alpha}(\omega) = \frac{1}{\exp((\omega - \mu_{\alpha})/T) + 1}$ denotes the Fermi-function. Performing the Keldysh rotation one is led to the components

$$G_{\alpha}^{0,R}(\omega) = \frac{N_0}{2} \ln \left| \frac{\omega + D_0}{\omega - D_0} \right| - i\pi N_0 \Theta(D_0 - |\omega|) \quad (4.57)$$

$$G_{\alpha}^{0,A}(\omega) = \frac{N_0}{2} \ln \left| \frac{\omega + D_0}{\omega - D_0} \right| + i\pi N_0 \Theta(D_0 - |\omega|) \quad (4.58)$$

$$G_{\alpha}^{0,K}(\omega) = -2\pi i \tanh \left(\frac{\omega - \mu_{\alpha}}{2T} \right) N_0 \Theta(D_0 - |\omega|). \quad (4.59)$$

Note that in the Keldysh rotated representation only the Keldysh component depends on the occupation number ($\tanh(\omega/(2T)) = 1 - 2f(\omega)$).

For the pseudo fermions, which serve as a fermionic representation of the Kondo impurity spin the Green function depends (supposed the impurity is subject to a magnetic field B) on spin and in addition on frequency. The contour ordered components read

$$F_{\gamma}^{0,<}(\omega) = 2\pi i n_{\gamma\lambda} \delta(\omega + \gamma \frac{B}{2}) \quad (4.60)$$

$$F_{\gamma}^{0,>}(\omega) = -2\pi i (1 - n_{\gamma\lambda}) \delta(\omega + \gamma \frac{B}{2}) \quad (4.61)$$

$$F_{\gamma}^{0,T}(\omega) = \mathcal{P} \frac{1}{\omega + \gamma \frac{B}{2}} + i\pi (2n_{\gamma\lambda} - 1) \delta(\omega + \gamma \frac{B}{2}) \quad (4.62)$$

$$F_{\gamma}^{0,\tilde{T}}(\omega) = -\mathcal{P} \frac{1}{\omega + \gamma \frac{B}{2}} + i\pi (2n_{\gamma\lambda} - 1) \delta(\omega + \gamma \frac{B}{2}). \quad (4.63)$$

After Keldysh rotation the various components take the form

$$F_{\gamma}^{0,R} = \frac{1}{\omega + \gamma \frac{B}{2} + i0} = \mathcal{P} \frac{1}{\omega + \gamma \frac{B}{2}} - i\pi \delta(\omega + \gamma \frac{B}{2}) \quad (4.64)$$

$$F_{\gamma}^{0,A} = \frac{1}{\omega + \gamma \frac{B}{2} - i0} = \mathcal{P} \frac{1}{\omega + \gamma \frac{B}{2}} + i\pi \delta(\omega + \gamma \frac{B}{2}) \quad (4.65)$$

$$F_{\gamma}^{0,K} = -2\pi i (1 - 2n_{\gamma\lambda}(\omega)) \delta(\omega + \gamma \frac{B}{2}). \quad (4.66)$$

Note that here n_{γ} is the Fermi function if and only if the whole system is in equilibrium. An important quantity to be defined is the spectral function $A_{\gamma}(\omega)$ for the pseudo

fermions

$$A_\gamma(\omega) = i(F_\gamma^R(\omega) - F_\gamma^A(\omega)). \quad (4.67)$$

The bare pseudo fermion spectral functions reduces to a δ -function, peaked at the Zeeman splitting $\pm B/2$

$$A_\gamma^0(\omega) = 2\pi\delta(\omega + \gamma\frac{B}{2}). \quad (4.68)$$

The imaginary part of the retarded or advanced self energy, which will later on serve as a cutoff in the FRG equations is given by

$$\Gamma_\gamma(\omega) = i(\Sigma_\gamma^R(\omega) - \Sigma_\gamma^A(\omega)) = 2\text{Im}\Sigma_\gamma(\omega). \quad (4.69)$$

4.4.2 Interaction Vertices

How does the Keldysh diagrammatic language influence the structure of the bare vertex?

In the following we will assume a two-body interaction of the type $V = \sum_{kk'q} v_{kk'q} c_{k'+q}^\dagger c_{k-q}^\dagger c_{k'} c_k$.

In the setup of the diagrammatic rules this expression appears in the exponential of the time evolution operator whereas all the $c^{(\dagger)}(t)$ operators possess equal time arguments. Consequently, in the contour representation the only two out of 16 possibilities are the ones, where all four Keldysh indices are identical. Due to a change of the time integration limits the vertex with all Keldysh indices on the lower branch of the Schwinger contour acquires an extra minus sign

$$\Lambda_{ab}^{cd} = \delta_{a=b=c=d}(-1)^{a-1}. \quad (4.70)$$

Transferring to the Keldysh rotated representation the structure of the bare interaction vertex becomes

$$\Lambda_{ab}^{cd} = \frac{1}{2} (\delta_{ab}\tau_{cd}^x + \delta_{cd}\tau_{ab}^x). \quad (4.71)$$

Which of the two—contour or Keldysh—representation should be favored depends on the particular problem and the order of the perturbative expression under consideration. Whereas the interaction vertex is clearly seen to have a simply structure in the contour representation, giving rise to only a few Keldysh contractions when evaluating Feynman diagrams, in the Keldysh representation the number of Green function is reduced and obeys a much simpler structure. For instance, while performing bare perturbation theory [55] or higher order resummation of diagrams [56] for the Kondo dot model it turns out that for second-order calculations the contour representation is the the best choice, whereas for third- and higher-order calculation the Keldysh matrix structure is more convenient.

4.5 Nonequilibrium Functional Renormalization Group - Flow Equations for the Kondo Model

In this section we will first off all generalize the concept of the FRG, which was introduced in Section 4.3 to nonequilibrium situations. To this end we need a formulation that allows us to express the n -particle Keldysh vertex functions as functional derivatives of a generating functional. We will follow the approach introduced by Kamenev [26].

The setup of the path integral is analogous to the equilibrium case with the difference that the time integration changes from the finite integral over the imaginary time interval $[0, \beta]$ to an infinite real time integral along the Keldysh contour. On a formal level this leads to an additional Keldysh index structure as shown in Section 4.4. It is convenient to introduce the spinor field

$$\psi = \begin{pmatrix} \psi_1 \\ \psi_2 \end{pmatrix},$$

where the ψ_i ($i = 1, 2$) are Grassmann variables residing on the forward or backward branch, respectively. Another formal change in the nonequilibrium case are additional factors of i that arise from the real time formulation. The generalization of the functional integral representation of the partition function (c.f. equ. (4.5)) to nonequilibrium is

$$Z = \frac{1}{Z_0} \int D[\bar{\psi}, \psi] e^{i\{(\bar{\psi}, G_0^{-1}\psi) - V(\bar{\psi}, \psi)\}} \quad (4.72)$$

where G_0 denotes the contour or Keldysh matrix propagator. From there we may now construct the generating functionals for the various kinds of correlation function and—apart from the above named differences—subject it to the apparatus introduced in Section 4.3 which leads to the FRG flow equation. The resulting equations formally differ from the equilibrium equations by the additional Keldysh index structure, i.e. an enlarged and modified structure of the propagators, self energy parts and vertex functions. We shall not present this straightforward derivation here in detail but refer the reader to Ref. [43], where the technical details in this regard may be found.

However, since we are interested in the Kondo dot model we will give a profound derivation of the flow equation in this particular case. In this case the action S takes the form

$$S = (\bar{\psi}, G_0^{-1}\psi) + (\bar{\phi}, F_0^{-1}\phi) - V[\bar{\psi}, \psi, \bar{\phi}, \phi], \quad (4.73)$$

with the free inverse matrix propagators for the conduction electrons G_0^{-1} and pseudo fermions F_0^{-1} respectively. For later purposes we introduce multi-indices for the lead electrons and the pseudo fermions by

$$\text{leadelectrons :} \quad e = (\alpha, \sigma, \omega_e, c_e) \quad (4.74)$$

$$\text{pseudofermions :} \quad f = (\gamma, \omega_f, c_f), \quad (4.75)$$

where $\alpha = L, R$ is the lead index, $\sigma, \gamma = \uparrow, \downarrow$ denote the z-component of the spin, ω_e and ω_f are the corresponding frequencies and c_e, c_f represent the Keldysh index.

Apart from the fact that the Kondo model contains two kinds of particles, i.e. the lead electrons and the pseudo fermions, which causes the introduction of two flavors of source fields for the generation of correlation functions, which will be denoted by $\bar{\eta}, \eta$ for the conduction electrons and by $\bar{\xi}, \xi$ for the pseudo fermions, respectively, the apparatus to obtain the FRG flow equations stays unchanged. The generating functional for the n -particle Green functions takes the following form

$$Z[\bar{\eta}, \eta, \bar{\xi}, \xi] = \frac{1}{Z_0} \int D[\bar{\psi}, \psi] D[\bar{\phi}, \phi] e^{iS+(\eta, \bar{\psi})+(\psi, \bar{\eta})+(\xi, \bar{\phi})+(\phi, \bar{\xi})}. \quad (4.76)$$

Via the generating functional for the connected Green function

$$\mathcal{W}[\bar{\eta}, \eta, \bar{\xi}, \xi] = \ln \mathcal{G}[\bar{\eta}, \eta, \bar{\xi}, \xi], \quad (4.77)$$

subject to a Legendre transformation finally leads to desired functional for the generation of the 1PI vertex functions

$$\begin{aligned} \Gamma[\bar{\chi}, \chi, \bar{\theta}, \theta] &= -\mathcal{W}[\bar{\eta}, \eta, \bar{\xi}, \xi] - (\bar{\eta}, \chi) - (\bar{\chi}, \eta) - (\bar{\xi}, \theta) - (\bar{\theta}, \xi) \\ &\quad + i(\bar{\chi}, G_0^{-1} \chi) + i(\bar{\theta}, F_0^{-1} \theta). \end{aligned} \quad (4.78)$$

To enhance readability most of the subsequent derivation of the FRG flow equations, which is of purely technical matter, is moved to Appendix D.

We choose to renormalize the lead electrons, i.e. to replace G_0 by a cutoff dependent propagator G_0^Λ . We shall use a sharp cutoff

$$G_0^\Lambda(\omega) = G_0(\omega) \Theta^\Lambda(\omega), \quad \text{where} \quad \Theta^\Lambda(\omega) = \Theta(|\omega| - \Lambda). \quad (4.79)$$

Performing the steps described previously in Section 4.3 one obtains an equation for the flow of Γ^Λ

$$\frac{d\Gamma^\Lambda}{d\Lambda} = \text{Tr} \left(\frac{d(G_0^\Lambda)^{-1}}{d\Lambda} G_0^\Lambda \right) - \text{Tr} \left(G^\Lambda \frac{d(G_0^\Lambda)^{-1}}{d\Lambda} \mathcal{R}_{1,1} \right), \quad (4.80)$$

where $\mathcal{R}_{1,1}$ is given by equ. (D.15). An expansion of Γ^Λ in the fields

$$\begin{aligned} \Gamma^\Lambda[\bar{\chi}, \chi, \bar{\vartheta}, \vartheta] &= \sum_{m=1}^{\infty} \sum_{l=0}^m \frac{(-i)^l}{(l!)^2} \frac{(-i)^{m-l}}{((m-l)!)^2} \sum_{e_1 \dots e_l} \sum_{e'_1 \dots e'_l} \sum_{f_1 \dots f_{m-l}} \sum_{f'_1 \dots f'_{m-l}} \times \\ &\quad \times \gamma_m^\Lambda(e'_1 \dots e'_l, f'_1 \dots f'_{m-l} | e_1 \dots e_l, f_1 \dots f_{m-l}) \prod_{i=1}^l \bar{\chi}_{e'_i} \chi_{e_i} \prod_{j=1}^{m-l} \bar{\vartheta}_{f'_j} \vartheta_{f_j} \end{aligned} \quad (4.81)$$

where

$$\begin{aligned} &\gamma_m^\Lambda(e'_1 \dots e'_l, f'_1 \dots f'_{m-l} | e_1 \dots e_l, f_1 \dots f_{m-l}) \\ &= i^m \frac{\partial^{2l}}{\partial \bar{\chi}_{e'_1} \partial \chi_{e_1} \dots \partial \bar{\chi}_{e'_l} \partial \chi_{e_l}} \frac{\partial^{2(m-l)}}{\partial \bar{\vartheta}_{f'_1} \partial \vartheta_{f_1} \dots \partial \bar{\vartheta}_{f'_{m-l}} \partial \vartheta_{f_{m-l}}} \Gamma^\Lambda[\bar{\chi}, \chi, \bar{\vartheta}, \vartheta] \end{aligned} \quad (4.82)$$

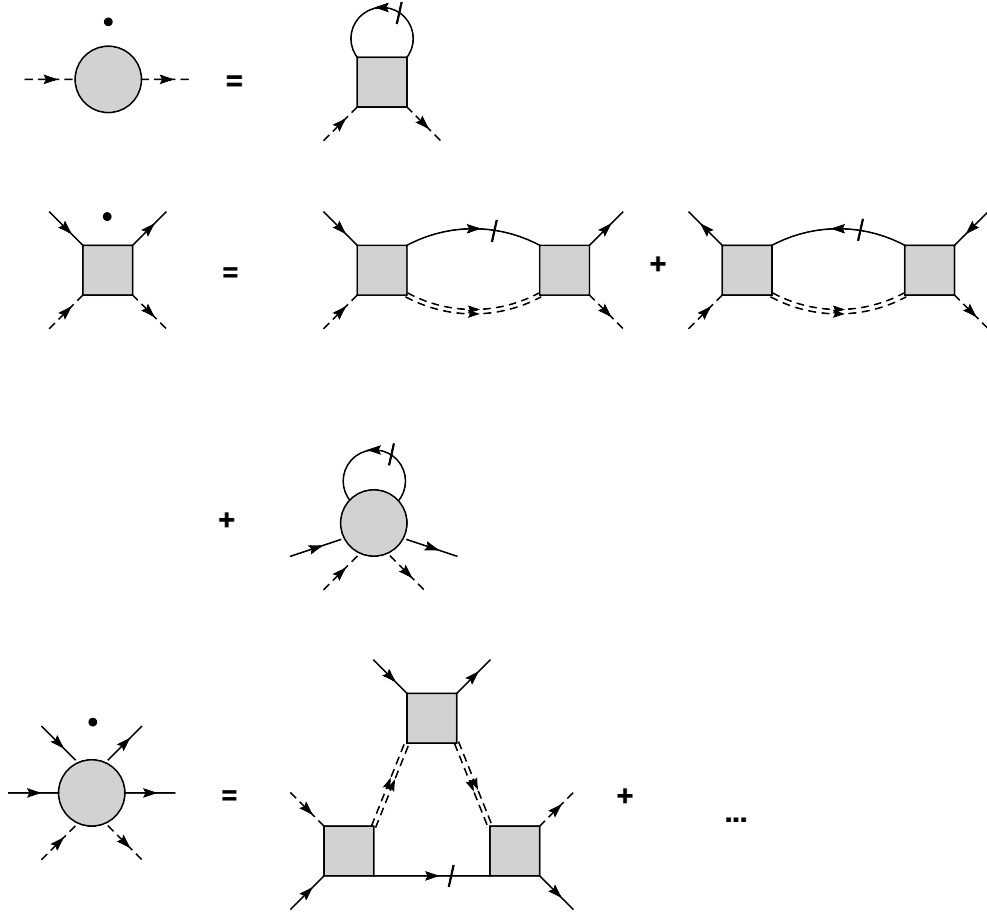


Figure 4.3: Graphical flow equation for the self energy γ_1 , the vertex function γ_2^Λ and the one particle irreducible six point function γ_3^Λ . Solid lines represent the lead electrons, whereas the dotted lines refer to the pseudo fermion propagator. Propagators containing a stroke symbolize the single scale propagator: since we have furnished the bare lead electron propagator with a cutoff function only this can turn into the single scale propagator

finally leads to an exact infinite hierarchy of flow equations for 1PI m -particle vertex functions γ_m , which appear as expansion coefficients in (4.81). A graphic representation of the resulting equations is depicted in Fig. 4.3. Therein solid lines represent the bare lead electron propagator, whereas the dotted lines refer to the fully dressed pseudo fermion propagator. Propagators containing a stroke symbolize the single scale propagator: since we have furnished the bare lead electron propagator with a cutoff function only this can turn into the single scale propagator.

In order to write down the FRG equations in a practical form we impose the following notation: since we include self energy effects only for the pseudo fermions we suppress a particular index which would declare that. Thus $\Sigma_\gamma^{ab,\Lambda}(\omega) = -\gamma_{\gamma,1}^{ab,\Lambda}$ denotes the spin γ and frequency ω dependent pseudo fermion self energy obeying the Keldysh indices a, b

at scale Λ . This notation can be transferred to the full pseudo fermion Green function $F_\gamma^{ab,\Lambda}(\omega)$. Similar the bare lead electron propagator $G_\alpha^{0,cd}(\omega)$ depends on the lead index α and not on spin (as long as the leads are not subject to a magnetic field), analogous for the single scale propagator $S_\alpha^{cd,\Lambda}(\omega) = \dot{C}^\Lambda(\omega)G_\alpha^{0,cd}(\omega)$. For the two-particle vertex function we shall suppress the index 2 and use γ instead of γ_2 . Hence $\gamma_{\gamma a, \gamma' b}^{\alpha \sigma c, \alpha' \sigma' d, \Lambda}(\omega_e, \omega_f; \omega'_e, \omega'_f)$ denotes the effective interaction at scale Λ where an electron from lead α with energy ω_e , spin σ and Keldysh index c interacts with a pseudo fermion with energy ω_f , spin γ and Keldysh index a and passes into an electron of lead α' with energy ω'_e , spin σ' and Keldysh index d and a pseudo fermion with energy ω'_f , spin γ' and Keldysh index b . Note that Kondo Hamiltonian implies energy and spin conservation, i.e.

$$\omega_e + \omega_f = \omega'_e + \omega'_f \quad (4.83)$$

$$\sigma + \gamma = \sigma' + \gamma'. \quad (4.84)$$

With this nomenclature at hand we are ready to write down the flow equations for the first two 1PI vertex functions. Explicitly these read

$$\partial_\Lambda \Sigma_\gamma^{ba,\Lambda}(\omega) = -\frac{1}{2\pi} \sum_{\alpha, \sigma, c, d, \epsilon} S_\alpha^{cd,\Lambda}(\epsilon) \gamma_{\gamma a, \gamma b}^{\alpha \sigma c, \alpha \sigma d, \Lambda}(\epsilon, \omega, \epsilon, \omega) \quad (4.85)$$

$$\begin{aligned} \partial_\Lambda \gamma_{\gamma a, \gamma' b}^{\alpha \sigma c, \alpha' \sigma' d, \Lambda}(\omega_e, \omega_f; \omega'_e, \omega'_f) &= -\frac{1}{2\pi} \sum_{\epsilon} \gamma_{\gamma a, \bar{\gamma} a'}^{\alpha \sigma c, \bar{\alpha} \bar{\sigma} c', \Lambda} S_{\bar{\alpha}}^{d' c', \Lambda}(\epsilon) F_{\bar{\gamma}}^{b' a', \Lambda}(\omega_e + \omega_f - \epsilon) \gamma_{\bar{\gamma} b', \gamma' b}^{\bar{\alpha} \bar{\sigma} d', \alpha' \sigma' d, \Lambda} \\ &+ \gamma_{\gamma a, \bar{\gamma} a'}^{\bar{\alpha} \bar{\sigma} d', \alpha' \sigma' d, \Lambda} S_{\bar{\alpha}}^{d' c', \Lambda}(\epsilon) F_{\bar{\gamma}}^{b' a', \Lambda}(\omega_f - \omega'_e + \epsilon) \gamma_{\bar{\alpha} b', \alpha' b}^{\alpha \sigma c, \bar{\alpha} \bar{\sigma} c', \Lambda} \end{aligned} \quad (4.86)$$

with the corresponding boundary conditions at $\Lambda_0 = D$

$$\Sigma_\gamma^{ba, \Lambda_0}(\omega) = 0 \quad (4.87)$$

$$\gamma_{\gamma a, \gamma' b}^{\alpha \sigma c, \alpha' \sigma' d, \Lambda_0}(\omega_e, \omega_f; \omega'_e, \omega'_f) = i \frac{J}{4} \vec{T}_{\sigma \sigma'} \vec{T}_{\gamma \gamma'} \Lambda_{ab}^{cd}. \quad (4.88)$$

For sake of simplicity and readability we have occasionally omitted the frequency dependence of the two-particle vertex functions on the right hand side of equ. (4.86). Furthermore, since in this equation all repeated indices are summed over (in contrast to equ. (4.86) where γ on the right hand side—as the outer spin variable—is not summed over) we have implied the Einstein summation convention. Additionally \sum_{ϵ} denotes the internal frequency integration. Here and in the following we will refer the first term on the right hand side of equ. (4.86) as the Cooper channel and the second term as the Peierls channel. The forms equ. (4.85) and (4.86) may be used for any cut-off function $C^\Lambda(\omega)$ or, respectively, corresponding single scale propagator $S^\Lambda(\omega)$. In the particular case of a sharp cutoff $C^\Lambda(\omega) = \Theta(|\omega| - \Lambda)$ the single scale propagator $S^\Lambda(\omega) = \dot{C}^\Lambda(\omega)G^0(\omega) = -\delta(|\omega| - \Lambda)G^0(\omega)$ singles out precisely the frequencies at $\omega = \pm\Lambda$ which involves the following replacement

$$\sum_{\epsilon} S^\Lambda(\epsilon) \rightarrow \sum_{\epsilon = \pm\Lambda} G^0(\epsilon). \quad (4.89)$$

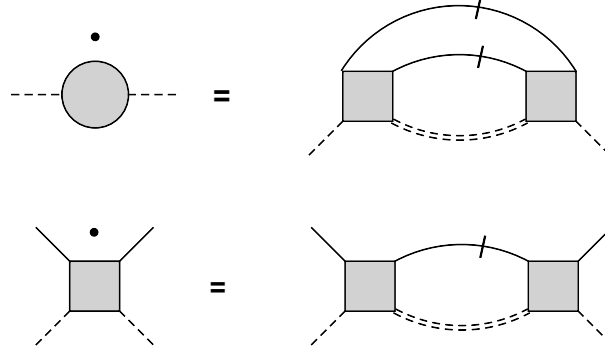


Figure 4.4: Graphical representation of the FRG equations for the self energy γ_1 and the vertex function γ_2^Λ that correspond to the integral forms (4.93) and (4.94). The digram on the right hand side of the equation for Σ^Λ contains one single scale propagator at scale Λ at another one at scale Λ' . This can be—as we do not include self energy corrections to the lead electron Green function—circumvented as stated in equ. (4.93)

Hence, by choosing a sharp cutoff no internal frequency integration is left on the right hand side of equ. (4.85) and (4.86).

In the case of a smooth cutoff function as for instance given by equ. (4.18) this set of equations may be rewritten in a more suitable form. To this end we first of all suppress, expect for the Λ -scale dependence, all prefactors, indices, internal frequency integrations and index summations. To begin with we integrate the flow equation for the two-particle vertex function (4.86) from $\Lambda_0 = D$ to Λ to obtain

$$\gamma^\Lambda = \int_{\Lambda_0}^{\Lambda} d\Lambda' \gamma^{\Lambda'} S^{\Lambda'} F^{\Lambda'} \gamma^{\Lambda'}. \quad (4.90)$$

Here and in the following the right hand side of this equation acts as a short hand representative for the sum of the Cooper and the Peierls channel. If we plug this expression in the equation for the pseudo fermion self energy (4.86) and integrate it from Λ_0 to 0 we obtain

$$\begin{aligned} \Sigma^{\Lambda=0} &= \int_{\Lambda_0}^0 d\Lambda S^\Lambda \int_{\Lambda_0}^{\Lambda} d\Lambda' \gamma^{\Lambda'} S^{\Lambda'} F^{\Lambda'} \gamma^{\Lambda'} \\ &= \int_{\Lambda_0}^0 d\Lambda \dot{C}^\Lambda \int_{\Lambda_0}^{\Lambda} d\Lambda' G^0 \gamma^{\Lambda'} S^{\Lambda'} F^{\Lambda'} \gamma^{\Lambda'} \\ &= \int_{\Lambda_0}^0 d\Lambda \dot{C}^\Lambda \int_{\Lambda_0}^{\Lambda} d\Lambda' R^{\Lambda'} \quad \text{with} \quad R^{\Lambda'} = G^0 \gamma^{\Lambda'} S^{\Lambda'} F^{\Lambda'} \gamma^{\Lambda'}. \end{aligned} \quad (4.91)$$

Since the only Λ dependence is contained in the derivative of the cutoff function we may subject the last line of equ. (4.91) to a partial integration [57]

$$\begin{aligned} \int_{\Lambda_0}^0 d\Lambda \dot{C}^\Lambda \int_{\Lambda_0}^\Lambda d\Lambda' R^{\Lambda'} &= C^\Lambda \int_{\Lambda_0}^\Lambda d\Lambda' R^{\Lambda'} \Big|_{\Lambda_0}^0 - \int_{\Lambda_0}^0 d\Lambda C^\Lambda R^\Lambda \\ &= C^0 \int_{\Lambda_0}^0 d\Lambda' R^{\Lambda'} - \int_{\Lambda_0}^0 d\Lambda C^\Lambda R^\Lambda \end{aligned} \quad (4.92)$$

and circumvent the double Λ integral of the previous form. Hence the final expression for Σ at the end of the flow

$$\Sigma^{\Lambda=0} = \int_{\Lambda_0}^0 d\Lambda' [C^0 - C^{\Lambda'}] G^0 \gamma^{\Lambda'} S^{\Lambda'} F^{\Lambda'} \gamma^{\Lambda'} \quad (4.93)$$

contains the two vertex functions and the pseudo fermion propagator at scale Λ and may be integrated along with the vertex function which we also write for completeness in a short hand and integral form as

$$\gamma^{\Lambda=0} = \int_{\Lambda_0}^0 d\Lambda' \gamma^{\Lambda'} S^{\Lambda'} F^{\Lambda'} \gamma^{\Lambda'}. \quad (4.94)$$

Again we want to stress that the expression (4.93) and (4.94) are most suitable when dealing with a soft cutoff since this forms reduces the numerical effort drastically, also when dealing with a frequency dependent pseudo fermion self energy.

5 The FRG to the Kondo Dot Model

5.1 Introduction

In this chapter we present the main body of our work, the application of the FRG to the Kondo dot model in and out of equilibrium. To begin with, however, we start this chapter with a prelude 5.2 where in Section 5.2.1 we review second order perturbative expressions for the self energy and the vertex function, respectively. These perturbative expressions serve on the one hand as a guide to the FRG equations for large values of Λ , on the other hand they may be taken as a check of the FRG equations as discussed in Section 5.2.2. In the subsequent Section 5.2.3 we show how Anderson's poor man scaling equations [27] are obtained from the FRG equations. In Section 5.2.4 we briefly summarize a perturbative renormalization group formalism by Rosch *et. al* [17, 18] which applies as well to the inclusion of a finite bias voltage (nonequilibrium) or a finite magnetic field. We shall later (at the end of Section 5.3.1) show how this scheme is reobtained or included, respectively within the FRG formalism.

In Section 5.3 we then turn towards the application of the FRG to the Kondo dot model. Initially in Section 5.3.1 we extract leading logarithmic terms from the vertex function and show that the resulting vertex function obeys upon keeping track only of the leading components the structure of the bare vertex. This is seen to simplify the FRG equations, i.e. the flow equations for the imaginary part of the pseudo fermion self energy and the effective interaction, substantially. In Section 5.3.2 we give approximated flow equation for Γ and a frequency independent g . In the following two Sections 5.3.3 and 5.3.4 we focus on a solution of the FRG equations in the weak coupling regime $T, V \gg T_K$. First, we solve the equations in the case of a frequency independent vertex and extract the (linear) conductance and the imaginary part of the self energy as function of temperature or voltage, respectively. In both cases Γ is seen to be not crucial as a cutoff for the FRG flow as in the weak coupling regime the temperature or the voltage serve as a cutoff for the frequency independent coupling. In a second step we determine the flow of the the frequency independent vertex function $g(\omega)$. Whereas the imaginary part of the pseudo fermion self energy is again not crucial for the equilibrium case even for zero frequency it is instrumental to cut off the divergencies at the resonance frequencies $\omega = \pm \frac{V}{2}$. We shall furthermore analyze the behavior and the breakdown of our approximated set of FRG equation as the strong coupling regime $T, V \lesssim T_K$ is reached. In Section 5.4 we address the question under which conditions the strong coupling regime may be approached and give preliminary results in case of equilibrium and in case of nonequilibrium.

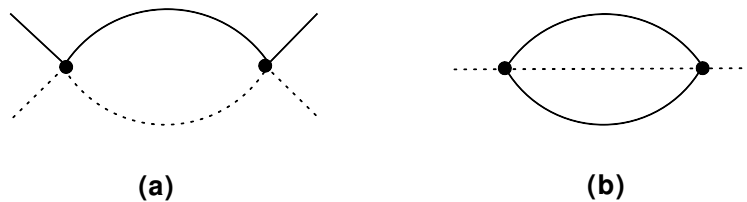


Figure 5.1: Second order perturbative expressions for (a) the vertex function and (b) the self energy part of the pseudo fermions.

5.2 Prelude

5.2.1 Perturbative Expressions

In this chapter we provide a short overview of second order perturbative expressions for the vertex function and the real- and imaginary part of the pseudo fermion self energy. A detailed derivation and discussion may be found in [55]. The corresponding unlabeled Feynman diagrams are depicted in Fig. 5.1. The diagram for the vertex function Fig. 5.1 (a) contributes with both directions on the pseudo fermion loop, which are referred to as the Cooper (parallel) and Peierls (anti-parallel) channel, respectively. The logarithmic terms stem from the convolution of the real part of the retarded or advanced component of the pseudo fermion propagator with the Keldysh Green function of the lead electrons. The resulting analytical expression reads

$$g_{\gamma\gamma'}^{\sigma\sigma'(2)} = -i \frac{g^2}{16} (\tau_{\sigma\sigma'}^i \tau_{\gamma\gamma'}^i \pm 3\tau_{\sigma\sigma'}^0 \tau_{\gamma\gamma'}^0) \sum_{\alpha,\gamma} \ln \frac{D^2}{(\epsilon - \mu_\alpha - \gamma B/2)^2 + T^2}, \quad (5.1)$$

where the upper sign refers to the Peierls and the lower one to the Cooper channel, respectively. The first non vanishing contribution to the pseudo fermion self energy is the second order diagram shown in Fig. 5.1 (b). Its frequency dependent imaginary part may for $B = V = 0$ and symmetric couplings be written as

$$\Gamma^{(2)}(\omega) = 3\pi g^2 \omega (1 + N(\omega)), \quad (5.2)$$

with $N(\omega)$ being the Bose function. For the zero frequency case we obtain

$$\Gamma^{(2)} = \begin{cases} \frac{3\pi}{4} g^2 V & \text{for } B = T = 0 \\ 3\pi g^2 T & \text{for } B = V = 0 \end{cases} \quad \text{and} \quad \Gamma_\gamma^{(2)} = \begin{cases} 2\pi g^2 B & \text{for } T = V = 0, \gamma = \downarrow \\ 0 & \text{for } T = V = 0, \gamma = \uparrow \end{cases} \quad (5.3)$$

Note that in the presence of a finite magnetic field (i.e. $V = T = 0$) only the upper spin level $\gamma = \downarrow$ is broadened, whereas broadening of the lower spin level $\gamma = \uparrow$ occurs in higher order in g .

The second order real part of the self energy, which we will denote by $R(\omega)$ may be written as

$$R_\gamma(\omega) = -\frac{g_{\alpha\alpha'}^2}{32} \Theta_{\gamma\gamma'} \int_{-D}^D d\epsilon \tanh\left(\frac{\epsilon + \omega - \mu_{\alpha'}}{2T}\right) \ln\left(\frac{D^2}{(\epsilon - \mu_\alpha - \gamma' \frac{B}{2})^2 + T^2}\right), \quad (5.4)$$

with the spin tensor $\Theta_{\gamma\gamma'} = \delta_{\gamma\gamma'} + 2\tau_{\gamma\gamma'}^x$. For later application we will need the wavefunction renormalization factor or Z-factor $Z_\gamma = (1 - \partial_\omega R(\omega = 0))^{-1}$. To obtain $\partial_\omega R(\omega = 0)$ we take the derivative of equ. (5.4) with respect to ω and obtain for $B = V = 0$

$$\partial_\omega R(\omega = 0) \approx -\frac{3}{2}g^2 \ln\left(\frac{D}{T}\right) \quad (5.5)$$

valid for $T \ll D$ (note: $1/(2T)1/\cosh^2(\epsilon/(2T)) \approx 2\delta(\epsilon)$).

5.2.2 Recovering Second Order Perturbation Theory

To exemplify the rederivation of the perturbative results from Section 5.2.1 from the FRG flow equations (4.85) and (4.86) we focus on the second order imaginary part of the self energy $\Gamma^{(2)}(\omega)$ for $V = B = 0$. The corresponding analytical expressions are given by equ. (5.2) and equ. (5.3). We shall work in the contour representation and use the Θ cutoff function. We start from equ. (4.93) and take on the right hand side bare propagators for the lead electrons as well as for the pseudo fermions. Furthermore we use bare vertices $J_{\alpha\alpha'}\vec{\tau}_{\sigma\sigma'}\vec{\tau}_{\gamma\gamma'}$ for the two vertex functions. Assuming symmetric couplings and performing the spin sums we obtain

$$\begin{aligned} \Gamma(\omega) &= i\Sigma^>(\omega) = \frac{-i6g^2}{8\pi^2} \int_{-D}^D d\epsilon \int_{-D}^D d\bar{\epsilon} \int_{\Lambda_0}^0 d\Lambda \Theta(\Lambda - |\epsilon|) G_0^<(\epsilon) F_0^>(\omega + \epsilon - \bar{\epsilon}) S^\Lambda(\bar{\epsilon}) \\ &= \frac{-i6g^2}{8\pi^2} \int_{-D}^D d\Lambda \int_{-\Lambda}^{\Lambda} d\epsilon G^<(\epsilon) G^>(\Lambda) F_0^>(\omega + \epsilon - \Lambda) \\ &= \frac{-i3g^2}{8\pi^2} \int_{-D}^D d\bar{\epsilon} \int_{-D}^D d\epsilon G^<(\epsilon) G^>(\bar{\epsilon}) F_0^>(\omega + \epsilon - \bar{\epsilon}) \\ &= \frac{3g^2}{4\pi} \int_{-D}^D d\epsilon G^<(\epsilon) G^>(\omega + \epsilon) = 3\pi g^2 \int_{-D}^D d\epsilon f(\epsilon)(1 - f(\omega + \epsilon)). \end{aligned} \quad (5.6)$$

With the help of equ. (E.2) one finally obtains the second order result equ. (5.2) or, putting ω to zero equ. (5.3). The second order real part of the self energy (equ. (5.4)) may be obtained in complete analogy but this time working in the Keldysh representation and noting that $R(\omega) = \text{Re}[\Sigma^{R/A}(\omega)]$. For illustration in Fig. 5.2 we show results where we have solved the FRG equations numerically with the above named simplifications and compare it to the exact analytical expression.

5.2.3 Poor Man's Scaling Limit

At zero temperature, in the absence of a magnetic field and a bias voltage Anderson's scaling equation [11] for the bandwidth-dependent coupling function described in Section

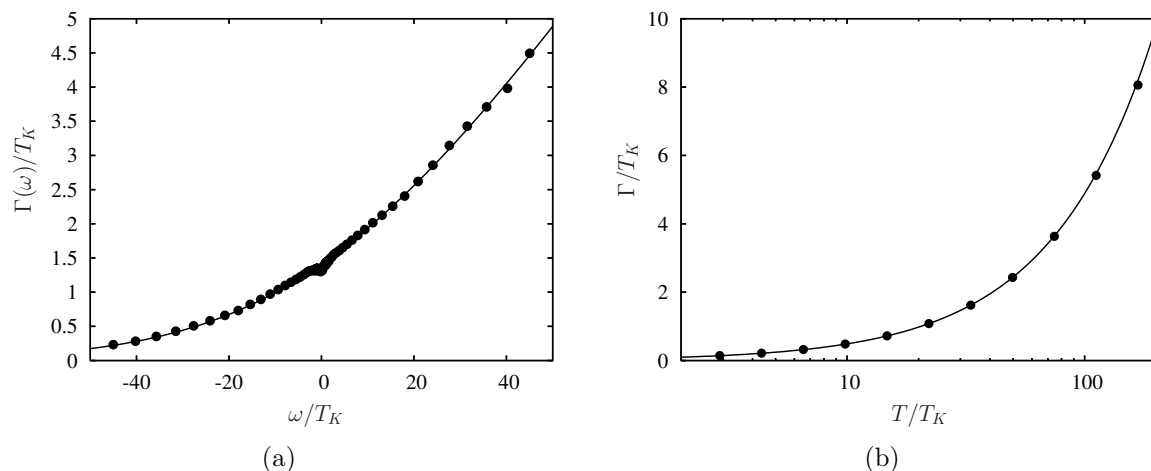


Figure 5.2: Rederivation of the perturbative results via the FRG flow equations: (a) shows the ω -dependence of the second order imaginary part of the self energy $\Gamma(\omega)$ for $B = V = 0$ and $T/T_K = 20$, whereas (b) depicts the temperature dependence of Γ at zero frequency and $B = V = 0$ for several values of T/T_K . In each figure the analytical expressions are represented by the solid lines whereas the numerical values (obtained by solving the FRG equations as stated in the text) are given by the dots.

3.5.2 may be derived as a certain limit from the FRG equations by means of the following simplifications: to begin with we neglect the influence of the three-particle and all higher order vertex functions. Further we do not take into account any self energy effects, i.e. we use bare propagators for both the pseudo fermions and the lead electrons. Hence, the set of equations (4.85) and (4.86) reduces to the one (4.86) for the vertex function only which we take as fully frequency independent. Most importantly the leading logarithmic (i.e. scale dependent) terms in Keldysh space stem from the convolution of the Keldysh lead electron propagator with the retarded advanced component of the pseudo fermion Green function. In this case the Peierls and Cooper bubble reduce to

$$C^\Lambda = \sum_{\epsilon=\pm\Lambda} \frac{-2\pi i \text{sign}(\epsilon)}{-\epsilon} = i4\pi \frac{1}{\Lambda} = -\Pi^\Lambda. \quad (5.7)$$

If we parameterize the residual Keldysh component of the vertex function as

$$N_0 \gamma_{\gamma\gamma'}^{\sigma\sigma'\Lambda}(0, 0; 0, 0) \equiv g^\Lambda \vec{\tau}_{\sigma\sigma'} \vec{\tau}_{\gamma\gamma'} \quad (5.8)$$

we are left with a single flow equation for g^Λ

$$\begin{aligned} \frac{\partial g^\Lambda \vec{\tau}_{\sigma\sigma'} \vec{\tau}_{\gamma\gamma'}}{\partial \Lambda} &= -i \frac{4}{\Lambda} (g^\Lambda)^2 \sum_{\bar{\sigma}\bar{\gamma}} [(\vec{\tau}_{\sigma\bar{\sigma}} \vec{\tau}_{\bar{\sigma}\gamma})(\vec{\tau}_{\bar{\sigma}\sigma'} \vec{\tau}_{\bar{\gamma}\gamma'}) - (\vec{\tau}_{\sigma\sigma'} \vec{\tau}_{\bar{\sigma}\gamma})(\vec{\tau}_{\bar{\sigma}\bar{\sigma}} \vec{\tau}_{\bar{\gamma}\gamma'})] \\ &= -i \frac{8}{\Lambda} (g^\Lambda)^2 \end{aligned} \quad (5.9)$$

where we performed the spin sums with the aid of (A.8) and (A.9). If we additionally perform the transformation $g^\Lambda \rightarrow i\frac{g^\Lambda}{4}$ we finally recover the scaling equation

$$\frac{\partial g^\Lambda}{\partial \ln(\Lambda)} = -2(g^\Lambda)^2 \quad \text{with} \quad g^{\Lambda_0=D} = g, \quad (5.10)$$

with the solution

$$g^\Lambda = \frac{1}{2 \ln(\Lambda/T_K)}, \quad T_K = D e^{-1/(2g)}. \quad (5.11)$$

Keeping the temperature T in (5.7), which is achieved by the replacement $\text{sign}(\epsilon) \rightarrow \tanh(\epsilon/2T)$ the RG equation (5.10) passes into the equation $\partial_\Lambda g^\Lambda = -2(g^\Lambda)^2 \tanh(\Lambda/2T)/\Lambda$ which, with the aid of the basic integral

$$\int_{-D}^D dx \frac{\tanh\left(\frac{x}{2T}\right)}{x} = 2 \ln(D/T) \quad (5.12)$$

can for $T > T_K$ be integrated down to $\Lambda = 0$ to yield

$$g(T) = \frac{1}{2 \ln(T/T_K)}. \quad (5.13)$$

Hence, for $T \gg T_K$ we stay in the weak coupling regime where $g(T) \ll 1$ and we may calculate physical quantities of interest by replacing the bare interaction vertices with the renormalized vertex (5.13). For instance the conductance of the Kondo dot model turns into

$$G(T) = \frac{3\pi^2}{16} \frac{1}{\ln^2(T/T_K)}. \quad (5.14)$$

5.2.4 Perturbative Renormalization Group

A more refined version of a perturbative renormalization group scheme in the spirit of Anderson's poor man scaling but generalized to the case of a finite bias voltage V or the inclusion of a magnetic field was invented by Rosch *et. al.* [17, 18] by investigating directly the scaling properties of second order diagrams. All leading logarithmic terms in perturbation theory stem from the vertex renormalization, when the real part of the pseudo fermions Green's function ($\sim 1/(\omega \pm B/2)$) is convoluted with the Keldysh component of the electronic line ($\sim N_0 \tanh[(\omega \pm V/2)/(2T)]$). Using the simplification

$$\frac{\partial}{\partial \ln D} \int_{-D}^D \frac{\text{sign}\omega}{\omega - \Delta\omega} \approx 2\Theta(D - |\Delta\omega|) \quad (5.15)$$

and arguing that within this approximation it is sufficient to keep track only of the real parts of the coupling functions on one Keldysh contour, which shall be denoted by

$g_{\gamma\omega_f;\gamma'\omega'_f}^{\alpha\sigma\omega_e;\alpha'\sigma'\omega'_e}$ in the following, the RG flow equations take the form

$$\begin{aligned} \frac{\partial g_{\gamma\omega_f;\gamma'\omega'_f}^{\alpha\sigma\omega_e;\alpha'\sigma'\omega'_e}}{\partial \ln D} &= \frac{1}{8} \sum_{\beta;\tau,\delta;\lambda=\pm} \left[g_{\gamma\omega_f;\delta*}^{\alpha\sigma\omega_e;\beta\tau\mu_\beta+\lambda D} g_{\delta*;\gamma'\omega'_f}^{\beta\tau\mu_\beta+\lambda D;\alpha'\sigma'\omega'_e} \Theta_{\omega_e+\omega_f-\mu_\beta+\delta\frac{B}{2}} \right. \\ &\quad \left. - g_{\delta*;\gamma'\omega'_f}^{\alpha\sigma\omega_e;\beta\tau\mu_\beta+\lambda D} g_{\gamma\omega_f;\delta*}^{\beta\tau\mu_\beta+\lambda D;\alpha'\sigma'\omega'_e} \Theta_{\omega'_f-\omega_e+\mu_\beta+\delta\frac{B}{2}} \right], \end{aligned} \quad (5.16)$$

with the short hand notation $\Theta_\omega = \Theta(D - |\omega|)$. This form of the perturbative RG equations is readily derived from the FRG flow equations in the same manner as we have demonstrated it in the previous section 5.2.3, i.e. by taking into account the flow equation for the vertex function only and neglecting self energy effects completely. Further simplifications of equ. (5.16) towards a smooth solution is achieved by using on-shell frequencies for the pseudo fermions (i.e. ω_f is assumed to be given by $-\gamma\frac{B}{2}$) and separating spin-flip processes g_\perp from non-flip processes g_z . The resulting equations are in detail presented and discussed in [17, 18].

Since no self energy effects have been taken into account so far the resulting coupling functions (i.e. the solutions for the RG equations in the limit $D \rightarrow 0$) show divergences for resonance frequencies $\omega = \pm V/2 \pm B/2$ or $\omega = \pm V/2 \pm B$. It is argued that the RG flow will be cut off and controlled by the dephasing of coherent spin flips. This spin relaxation rate $\Gamma = \frac{1}{T_2}$ is calculated by a second order expression using renormalized couplings

$$\begin{aligned} \Gamma = \frac{1}{T_2} &= \frac{\pi}{8\hbar} \sum_{\gamma\sigma\alpha\alpha'} \int d\omega f_\omega^\alpha (1 - f_\omega^{\alpha'}) [g_{z\sigma}^{\alpha\alpha'}]^2 \\ &\quad + f_\omega^\alpha (1 - f_{\omega-\gamma B}^{\alpha'}) \left[g_{\perp,-\gamma}^{\alpha\alpha'} \left(\omega - \frac{\gamma B}{2} \right) \right]^2, \end{aligned}$$

which a posteriori is incorporated in the RG equations by replacing

$$\Theta_\omega \rightarrow \Theta(D - \sqrt{\omega^2 + \Gamma^2}).$$

These equations for the coupling function and the decoherence rate are solved iteratively until convergence it reached.

5.3 Weak Coupling Regime

5.3.1 Vertex Function Structure

One basic ingredient of the perturbative RG by Rosch *et. al.* [17, 18] is the use of one single component in Keldysh space which we will analyze in the following. First of all we extract the leading components of the vertex function γ in Keldysh space and will see that upon keeping track only of these components there are no other Keldysh components generated such that we are allowed to deal with only one single amplitude.

Starting point for the following considerations is equation (4.86) in the Keldysh rotated form. To begin with we again note that the leading logarithmic terms in the FRG equation for γ originate from the product of the Keldysh component of the lead electron G^K with the real part of the retarded or advanced pseudo fermion propagator $F^{R,A}$. If we keep only these two terms in the sum over Keldysh indices on the right hand side of equ. (4.86) and neglect the Λ dependence that appears in the energy arguments of the vertex function we may write this equation in a short hand notation as

$$\partial_\Lambda \gamma_{ab}^{cd} = \sum_{a'=1,2} \Pi_{R,A}^K \gamma_{aa'}^{1d} \gamma_{a'b}^{c2} + \sum_{a'=1,2} C_{R,A}^K \gamma_{aa'}^{c2} \gamma_{a'b}^{1d}. \quad (5.17)$$

Here Π and C denote the Peierls and the Cooper bubble, respectively, and the leading components stem from its imaginary part. However, for completeness we state both the imaginary as well as the real part. To this end we decompose the individual channels as

$$C_{R,A}^K = \pm C_r + iC_i \quad (5.18)$$

$$\Pi_{R,A}^K = \pm \Pi_r + i\Pi_i, \quad (5.19)$$

where the single contributions are explicitly given by

$$C_i \equiv -2\pi N_0 \sum_{\epsilon=\pm\Lambda} \frac{\tanh(\frac{\epsilon-\mu\bar{\alpha}}{2T})(\omega_f + \omega_e - \epsilon + \bar{\gamma}\frac{B}{2})}{(\omega_f + \omega_e - \epsilon + \bar{\gamma}\frac{B}{2})^2 + \left(\frac{\Gamma_\gamma}{2}\right)^2} \quad (5.20)$$

$$\Pi_i \equiv -2\pi N_0 \sum_{\epsilon=\pm\Lambda} \frac{\tanh(\frac{\epsilon-\mu\bar{\alpha}}{2T})(\omega'_f - \omega_e + \epsilon + \bar{\gamma}\frac{B}{2})}{(\omega'_f - \omega_e + \epsilon + \bar{\gamma}\frac{B}{2})^2 + \left(\frac{\Gamma_\gamma}{2}\right)^2} \quad (5.21)$$

and

$$C_r \equiv -\pi N_0 \sum_{\epsilon=\pm\Lambda} \frac{\tanh(\frac{\epsilon-\mu\bar{\alpha}}{2T})\Gamma_\gamma}{(\omega_f + \omega_e - \epsilon + \bar{\gamma}\frac{B}{2})^2 + \left(\frac{\Gamma_\gamma}{2}\right)^2} \quad (5.22)$$

$$\Pi_r \equiv -\pi N_0 \sum_{\epsilon=\pm\Lambda} \frac{\tanh(\frac{\epsilon-\mu\bar{\alpha}}{2T})\Gamma_\gamma}{(\omega'_f - \omega_e + \epsilon + \bar{\gamma}\frac{B}{2})^2 + \left(\frac{\Gamma_\gamma}{2}\right)^2}. \quad (5.23)$$

To simplify matters we have already assumed a energy independent imaginary part of the pseudo fermion self energy Γ_γ and furthermore dropped the real part of the self energy. Again we want to emphasize that $C_i, \Pi_i \propto \frac{1}{\Lambda}$ and hence produce the leading components, whereas $C_r, \Pi_r \propto \frac{1}{\Lambda^2}$ give rise to subleading corrections. In the following we neglect contributions from C_r and Π_r and focus on the leading components only. Hence, we are left to the equation

$$\partial_\Lambda \gamma_{ab}^{cd} = \Pi_i \sum_{a'=1,2} \gamma_{aa'}^{1d} \gamma_{a'b}^{c2} + C_i \sum_{a'=1,2} \gamma_{aa'}^{c2} \gamma_{a'b}^{1d}. \quad (5.24)$$

To examine the behavior under the FRG we perform a Picard-Lindelöf like iteration, i.e. we start with the bare vertex structure $\gamma_{ab}^{cd} = \Lambda_{ab}^{cd} = \frac{1}{2}(\delta_{ab}\tau_{cd}^1 + \tau_{ab}^1\delta_{cd})$ on the right

hand side of equ. (5.24). By performing the sum over Keldysh indices we can infer that in the Cooper channel this structure is reproduced

$$\begin{aligned}
\sum_{a'=1,2} \gamma_{aa'}^{c2} \gamma_{ab}^{1d} &= \frac{1}{4} \{ (\delta_{a1} \tau_{c2}^1 + \tau_{a1}^1 \delta_{c2}) (\delta_{1b} \tau_{1d}^1 + \tau_{1b}^1 \delta_{1d}) \\
&+ (\delta_{a2} \tau_{c2}^1 + \tau_{a2}^1 \delta_{c2}) (\delta_{2b} \tau_{1d}^1 + \tau_{2b}^1 \delta_{1d}) \} \\
&= \frac{1}{4} \{ \tau_{c2}^1 \tau_{1d}^1 [\delta_{a1} \delta_{1b} + \delta_{a2} \delta_{2b}] + \delta_{c2} \delta_{1d} [\tau_{a1}^1 \tau_{1b}^1 + \tau_{a2}^1 \tau_{2b}^1] \\
&+ \tau_{c2}^1 \delta_{1d} [\delta_{a1} \tau_{1b}^1 + \delta_{a2} \tau_{2b}^1] + \delta_{c2} \tau_{1d}^1 [\tau_{a1}^1 \delta_{1b} + \tau_{a2}^1 \delta_{2b}] \} \\
&= \frac{1}{4} \{ \tau_{c2}^1 \tau_{1d}^1 \delta_{ab} + \delta_{c2} \delta_{1d} \delta_{ab} + \tau_{c2}^1 \delta_{1d} \tau_{ab}^1 + \delta_{c2} \tau_{1d}^1 \tau_{ab}^1 \} \\
&= \frac{1}{4} \{ \tau_{cd}^1 \delta_{ab} + \delta_{cd} \tau_{ab}^1 \}. \tag{5.25}
\end{aligned}$$

Likewise for the Peierls channel where a similar calculation gives

$$\begin{aligned}
\sum_{a'=1,2} \gamma_{aa'}^{1d} \gamma_{ab}^{c2} &= \frac{1}{4} \{ (\delta_{a1} \tau_{1d}^1 + \tau_{a1}^1 \delta_{1d}) (\delta_{1b} \tau_{c2}^1 + \tau_{1b}^1 \delta_{c2}) \\
&+ (\delta_{a2} \tau_{1d}^1 + \tau_{a2}^1 \delta_{1d}) (\delta_{2b} \tau_{c2}^1 + \tau_{2b}^1 \delta_{c2}) \} \\
&= \frac{1}{4} \{ \tau_{c2}^1 \tau_{1d}^1 [\delta_{a1} \delta_{1b} + \delta_{a2} \delta_{2b}] + \delta_{c2} \delta_{1d} [\tau_{a1}^1 \tau_{1b}^1 + \tau_{a2}^1 \tau_{2b}^1] \\
&+ \tau_{c2}^1 \delta_{1d} [\tau_{a1}^1 \delta_{1b} + \tau_{a2}^1 \delta_{2b}] + \delta_{c2} \tau_{1d}^1 [\delta_{a1} \tau_{1b}^1 + \delta_{a2} \tau_{2b}^1] \} \\
&= \frac{1}{4} \{ \tau_{c2}^1 \tau_{1d}^1 \delta_{ab} + \delta_{c2} \delta_{1d} \delta_{ab} + \tau_{c2}^1 \delta_{1d} \tau_{ab}^1 + \delta_{c2} \tau_{1d}^1 \tau_{ab}^1 \} \\
&= \frac{1}{4} \{ \tau_{cd}^1 \delta_{ab} + \delta_{cd} \tau_{ab}^1 \}. \tag{5.26}
\end{aligned}$$

Hence, by considering only the leading components in Keldysh space, we conclude that there is only one invariant amplitude, with the structure of the bare vertex

$$\gamma_{ab}^{cd} \sim \gamma \Lambda_{ab}^{cd}. \tag{5.27}$$

To reobtain the perturbative RG scheme [17, 18] from the FRG equation (4.86) the following additional steps would have to be performed: To begin with the imaginary part of the pseudo fermion self energy is dropped from the denominator of equ. (5.20) and (5.21). Moreover the energies of the pseudo fermions are put on-shell, i.e. $\omega_f = -\gamma B/2$. Hence, the coupling function becomes dependent only on a single frequency, the frequency of the incoming electron, which simplifies matters substantially. Finally the cutoff dependence of the Cooper and Peierls channel (equ. (5.20) and (5.21)) are approximated by a window function

$$\sum_{\epsilon=\pm\Lambda} \frac{\text{sign}(\epsilon)}{\epsilon - \Delta\omega} = 2 \frac{\Lambda}{\Lambda^2 - (\Delta\omega)^2} \approx \frac{2}{\Lambda} \Theta(\Lambda - |\Delta\omega|) \tag{5.28}$$

as more detailed described in [17, 18]. Here $\Delta\omega$ depends on V, B and the incoming and outgoing frequencies. Finally, in order to incorporate decoherence effects, which serve

as a cutoff for the RG flow, a mixture of both self energy and vertex correction Γ is built in a posteriori in equ. (5.28) by replacing $\Theta(\Lambda - |\Delta\omega|)$ with $\Theta(\Lambda - \sqrt{(\Delta\omega)^2 + \Gamma^2})$, where Γ in turn is calculated by a second order golden rule expression with renormalized vertices. These two equations (i.e. for the coupling function and the decoherence rate Γ) are then solved iteratively, until one reaches convergence.

In the following chapters the incorporation or generation of this decoherence rate (to be more precise the imaginary part of the pseudo fermion self energy which is part of the decoherence rate) in a systematic way will play a major role. To this end we first approximate the coupled equations (4.85) and (4.86) in an appropriate way and then solve these equations for different parameter regimes.

5.3.2 Approximated Flow Equations with Frequency Independent Couplings

In this chapter we will derive a set of coupled differential equations for the imaginary part of the pseudo fermion self energy Γ and the effective interaction γ . To begin with we neglect the frequency dependence of the leading component of the vertex function completely and hence are let to the following equation

$$\partial_\Lambda \gamma_{\gamma;\gamma'}^{\alpha\sigma;\alpha'\sigma'} = -\frac{1}{2\pi} \sum_{\bar{\alpha}\bar{\gamma}\bar{\sigma}} \left[\gamma_{\gamma;\bar{\gamma}}^{\alpha\sigma;\bar{\alpha}\bar{\sigma}} \gamma_{\bar{\gamma};\gamma'}^{\bar{\alpha}\bar{\sigma};\alpha'\sigma'} C_{\bar{\gamma}}^{\bar{\alpha}}(\Lambda) + \gamma_{\gamma;\bar{\gamma}}^{\bar{\alpha}\bar{\sigma};\alpha\sigma} \gamma_{\bar{\gamma};\gamma'}^{\alpha\sigma;\bar{\alpha}\bar{\sigma}} \Pi_{\bar{\gamma}}^{\bar{\alpha}}(\Lambda) \right], \quad (5.29)$$

where

$$C_{\bar{\gamma}}^{\bar{\alpha}}(\Lambda) = -2\pi N_0 \sum_{\epsilon=\pm\Lambda} \frac{\tanh(\frac{\epsilon-\mu_{\bar{\alpha}}}{2T})(-\epsilon + \bar{\gamma}\frac{B}{2})}{(-\epsilon + \bar{\gamma}\frac{B}{2})^2 + \left(\frac{\Gamma_{\bar{\gamma}}}{2}\right)^2} \quad (5.30)$$

$$\Pi_{\bar{\gamma}}^{\bar{\alpha}}(\Lambda) = -2\pi N_0 \sum_{\epsilon=\pm\Lambda} \frac{\tanh(\frac{\epsilon-\mu_{\bar{\alpha}}}{2T})(\epsilon + \bar{\gamma}\frac{B}{2})}{(\epsilon + \bar{\gamma}\frac{B}{2})^2 + \left(\frac{\Gamma_{\bar{\gamma}}}{2}\right)^2}. \quad (5.31)$$

For the imaginary part of the pseudo fermion self energy $\Gamma = i(\Sigma^R - \Sigma^A) = i\Sigma^>$ we need from equ. (4.85) the vertex function $\gamma_{\gamma a, \gamma b}^{\alpha, \sigma c; \alpha \sigma d}(\epsilon, 0; \epsilon, 0)$ with $\epsilon = \pm\Lambda$. Note that if we simply substitute this vertex function by an energy independent one of the form (5.27) the imaginary part of the pseudo fermion self energy turns out to vanish identically. However, on the right hand side of the equation for $\gamma(\epsilon, 0; \epsilon, 0)$ we use the leading components, i.e. the form equ. (5.27). To distinguish $\gamma(\epsilon, 0; \epsilon, 0)$ from the leading component γ we shall define $\gamma(\epsilon, 0; \epsilon, 0) = \tilde{\gamma}(\epsilon)$. Hence, the equation for $\tilde{\gamma}(\epsilon)$ takes the form

$$\begin{aligned} \partial_\Lambda \tilde{\gamma}_{\gamma a; \gamma b}^{\alpha \sigma c; \alpha \sigma d}(\epsilon) = & -\frac{1}{2\pi} \sum_{\bar{\alpha}\bar{\sigma}\bar{\gamma}} \sum_{a'b'c'd'} \left[\gamma_{\gamma;\bar{\gamma}}^{\alpha\sigma;\bar{\alpha}\bar{\sigma}} \gamma_{\bar{\gamma};\gamma}^{\bar{\alpha}\bar{\sigma};\alpha\sigma} \Lambda_{aa'}^{cc'} \Lambda_{b'b}^{d'd} \tilde{C}_{a'b'\bar{\gamma}}^{c'd'\bar{\alpha}}(\Lambda, \epsilon) \right. \\ & \left. + \gamma_{\gamma;\bar{\gamma}}^{\bar{\alpha}\bar{\sigma};\alpha\sigma} \gamma_{\bar{\gamma};\gamma}^{\alpha\sigma;\bar{\alpha}\bar{\sigma}} \Lambda_{aa'}^{d'd} \Lambda_{b'b}^{cc'} \tilde{\Pi}_{a'b'\bar{\gamma}}^{c'd'\bar{\alpha}}(\Lambda, \epsilon) \right] \quad (5.32) \end{aligned}$$

where the Cooper and Peierls bubble read

$$\tilde{C}_{a'b'\bar{\gamma}}^{c'd'\bar{\alpha}}(\Lambda, \epsilon) = \sum_{\tilde{\epsilon}=\pm\Lambda} G_{\bar{\alpha}}^{d'c'}(\tilde{\epsilon}) F_{\bar{\gamma}}^{b'a'}(\epsilon - \tilde{\epsilon}) \quad (5.33)$$

$$\tilde{\Pi}_{a'b'\bar{\gamma}}^{c'd'\bar{\alpha}}(\Lambda, \epsilon) = \sum_{\tilde{\epsilon}=\pm\Lambda} G_{\bar{\alpha}}^{d'c'}(\tilde{\epsilon}) F_{\bar{\gamma}}^{b'a'}(\epsilon + \tilde{\epsilon}). \quad (5.34)$$

With the aid of (5.32) the equation for the imaginary part of the pseudo fermion self energy may be cast in the form

$$\partial_{\Lambda}\Gamma_{\gamma} = -\frac{i}{2\pi} \sum_{\epsilon=\pm\Lambda} \left(\tilde{\gamma}_{\gamma 1; \gamma 1}^{\alpha\sigma c; \alpha\sigma d}(\epsilon) - \tilde{\gamma}_{\gamma 2; \gamma 2}^{\alpha\sigma c; \alpha\sigma d}(\epsilon) \right) G_{\alpha}^{cd}(\epsilon) \quad (5.35)$$

Hence equ. (5.29), (5.32) and (5.35) provide the desired system of coupled differential equations for the vertex function and the imaginary part of the pseudo fermion self energy. Note that all these equations are given in the Keldysh rotated representation. Optionally we may switch to use contour ordered representation for equ. (5.32) and (5.35). In this case equ. (5.32) keeps its structure but with the replacement of the bare vertex structure from the Keldysh rotated form (4.71) to the contour ordered one (4.70). Additionally the propagators have to be changed. The equation for the imaginary part of the self energy changes according to

$$\partial_{\Lambda}\Gamma_{\gamma} = i\dot{\Sigma}_{\gamma}^{\dot{>}} = -\frac{i}{2\pi} \sum_{\epsilon=\pm\Lambda} \tilde{\gamma}_{\gamma 1; \gamma 2}^{\alpha\sigma c; \alpha\sigma d}(\epsilon) G_{\alpha}^{cd}(\epsilon) \quad (5.36)$$

Starting from these equations we will in the following sub-chapters consider different parameter regimes, in particular for the temperature T and the bias voltage V . Alternatively we could have also made use of equ. (4.93). If we for each of the two vertex functions on the right hand side of this equation plug in the leading component obeying the form (5.27) then, together with the flow equation (5.29), we obtain directly a coupled system of two equations for the imaginary part Γ and the vertex function γ . As already stated in Section 4.5 in case of a soft cutoff the latter turns out to be more suitable whereas in case of a sharp cutoff the above proposed set of three equations is more appropriate.

5.3.3 Weak Coupling and Linear Response at Finite Temperature

Frequency Independent Couplings

To begin with a quantitative analysis we focus on the weak coupling regime $T/T_K \gg 1$ and $B = V = 0$. In this case the Cooper and Peierls channel (5.30) and (5.31) simplify to

$$C(\Lambda) = 2\pi N_0 \sum_{\epsilon=\pm\Lambda} \frac{\epsilon \tanh(\frac{\epsilon}{2T})}{\epsilon^2 + (\Gamma_{\gamma}/2)^2} = 4\pi N_0 \frac{\Lambda \tanh(\frac{\Lambda}{2T})}{\Lambda^2 + (\Gamma_{\gamma}/2)^2} = -\Pi(\Lambda). \quad (5.37)$$

For the following analysis we introduce the dimensionless quantity $g = N_0\gamma$ and parameterize the coupling g as $g_{\gamma; \gamma'}^{\alpha\sigma; \alpha'\sigma'} = g_{\alpha\alpha'} \vec{\tau}_{\sigma\sigma'} \vec{\tau}_{\gamma\gamma'}$. We furthermore assume the couplings

to be equal and perform the internal spins sums with the aid of (A.8) and (A.9). Then equ. (5.29) turns into

$$\partial_\Lambda g = -2g^2 \tanh\left(\frac{\Lambda}{2T}\right) \frac{\Lambda}{\Lambda^2 + (\Gamma/2)^2}, \quad (5.38)$$

with the initial condition $g^{\Lambda_0=D} = g_0 = N_0 J$. For the imaginary part of the pseudo fermion self energy we make use of equ. (5.36) together with (5.32). Due to the bare vertex structure (4.70) equ. (5.32) for the Cooper and the Peierls channel in each case picks out just a single contribution with regard to the Keldysh structure. These contributions, however, in combination with equ. (5.36) produce equal results and may be simply added up. Additionally, as we do not include a magnetic field, we may already perform the internal spin sum both for $\tilde{\gamma}$ and Γ and hence we are left with the following simplified set of FRG equations

$$\partial_\Lambda \tilde{g}(\epsilon) = 3g^2 \sum_{\tilde{\epsilon}=\pm\Lambda} f(-\tilde{\epsilon}) \frac{\Gamma}{(\epsilon - \tilde{\epsilon})^2 + (\Gamma/2)^2} \quad (5.39)$$

$$\partial_\Lambda \Gamma = \sum_{\epsilon=\pm\Lambda} f(\epsilon) \tilde{g}(\epsilon). \quad (5.40)$$

In this case the corresponding initial conditions read

$$\tilde{\gamma}^{\Lambda_0=D}(\epsilon) = 0 \quad \text{and} \quad \Gamma^{\Lambda_0=D} = 0. \quad (5.41)$$

For the numerical treatment of these equations, however, we have to take a small but finite value for Γ^{Λ_0} initially since otherwise no finite Γ would be generated along the FRG flow. This fact may be substantiated by the following reasoning: In order to rederive the perturbative, second order results as depicted in Section 5.2.2 we have inter alia to use bare propagators. Consequently the decoherence broadened spectral functions $\Gamma/(\omega^2 + \Gamma^2)$ would pass into the bare one, given by $A(\omega) = \delta(\omega)$. For a numerical treatment, however, we have to broaden the δ -functions, i.e. we again bring it into the form $\Gamma_0/(\omega^2 + \Gamma_0^2)$ with a small but finite Γ_0 . It turns out that the solution of the FRG equations does not depend crucially on the choice of the initial value of Γ^{Λ_0} as long as it is taken to be sufficiently small. We will render this statement more precisely in a moment.

We now solve the FRG equations for values of $T/T_K \gg 1$ and obtain results as shown in Fig. 5.3. The left panel displays the conductance as a function of T/T_K which is obtained via the leading component by the relation $G = \frac{3\pi^2}{4} g^2$. Hence, this curve resembles the behavior of the leading component g as a function of T/T_K . The dots represent the results from the numerical evaluation of the FRG equations which perfectly agree with the solid line, corresponding to the expected analytical result (5.14). In the right panel we show the imaginary part of the pseudo fermion self energy in units of T_K as a function of T/T_K . The solid line corresponds to the analytical form $\Gamma = 3\pi T \frac{1}{(2 \ln(T/T_K))^2}$. The FRG result shows a small discrepancy compared to the analytical result. We shall discuss this at the end of Section 5.3.4.

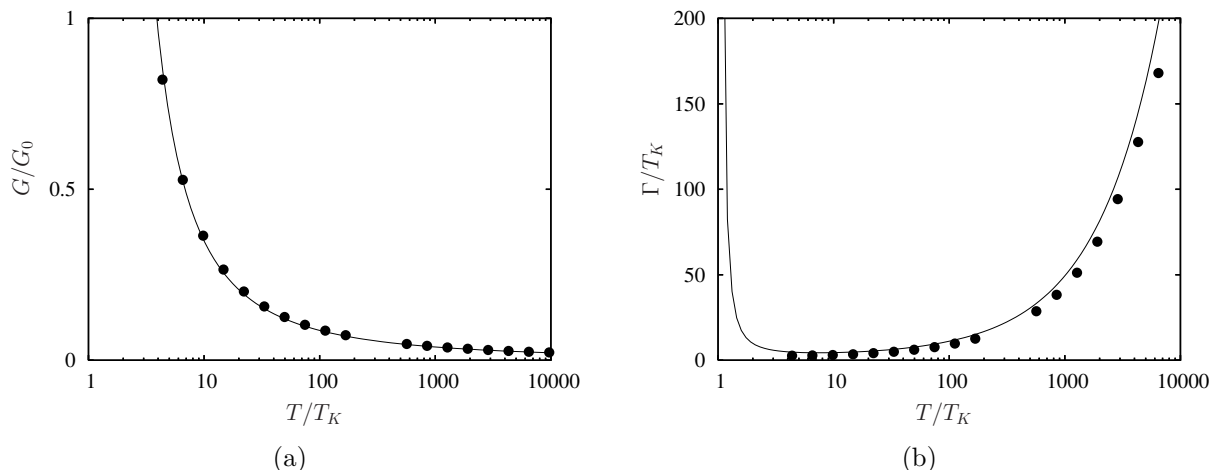


Figure 5.3: (a) Conductance in units of $G_0 = 2e^2/h$ as a function of T/T_K . Dots denote the result obtained by solving the FRG equations numerically. The solid line corresponds to the weak coupling form $G/G_0 = \frac{3\pi^2}{16} \frac{1}{\ln^2(T/T_K)}$. (b) Imaginary part of the self energy Γ as a function of T/T_K . Dots represent again the results from the FRG, the solid line is given by $\Gamma = 3\pi T \frac{1}{(2\ln(T/T_K))^2}$. In both cases we can report good agreement with the expected analytical behavior.

Let us at this point return to the above statement for the initial value of Γ : For the present examples we took an initial value $\Gamma^{\Lambda_0=D} = 0.1 T_K$. The lowest value of Γ in Fig. 5.3 amounts approximately to $2.5 T_K$. At a fixed temperature T/T_K any larger initial value would roughly speaking simply add on the present value of Γ (likewise any smaller value would have to be subtracted). In other words the curve of $\Gamma(T/T_K)$ is shifted by the initial value. From this arguments we may infer the quantitative statement: as long as $\Gamma^{\Lambda_0=D}/T_K \ll 1$ and hence is much smaller than the smallest occurring value for Γ the solution of the FRG equations in the regime T/T_K does not depend crucially on the initial value $\Gamma^{\Lambda_0=D}$.

Finally we will turn our attention to the region $T/T_K \gtrsim 1$. In the left panel of Fig. 5.4 we show the imaginary part of the pseudo fermion self energy for values of T/T_K down to ≈ 0.7 . In contrast to the analytical form the result obtained from the numerical evaluation of the FRG equations does not diverge as $T/T_K \rightarrow 1$. Likewise from Fig. 5.5 (a) for $T/T_K \gtrsim 1$ the leading component of the coupling function g is seen to stay finite, it leaves, however, the weak coupling regime where $g \ll 1$ as soon as the temperature crosses T_K . In Fig. 5.5 (b) we show the flow of g for various values of T/T_K . As long as T/T_K is still large compared to unity the temperature serves as a cutoff for the flow of the coupling function. For values of the order of the Kondo temperature, however, the effect of the imaginary part of the pseudo fermion self energy is crucial to maintain a weak coupling behavior of the vertex function. On the basis of this lifetime effect the

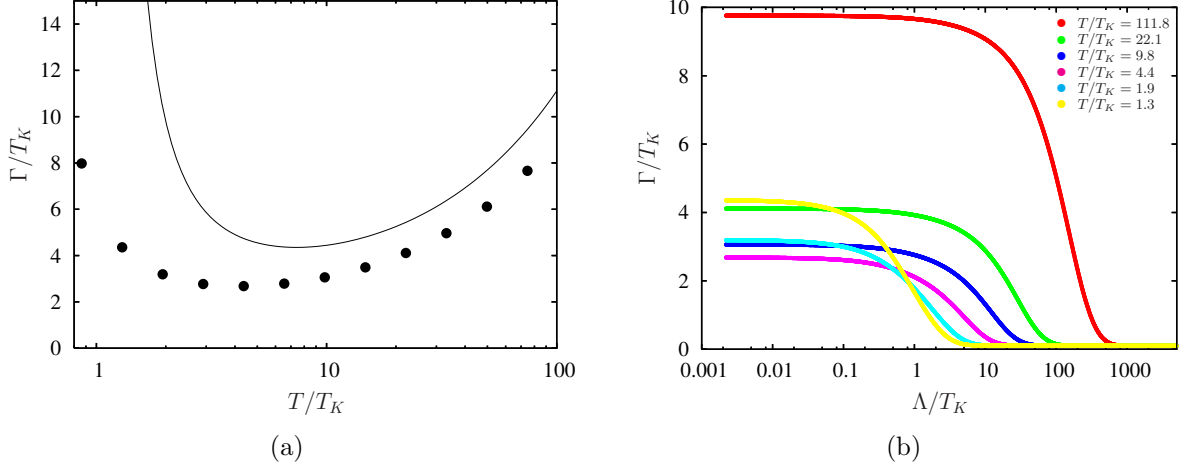


Figure 5.4: (a) Imaginary part of the self energy Γ as a function of T/T_K for values down to $T/T_K \approx 1$. Dots represent the results from the numerical evaluation of the FRG, the solid line is given by $\Gamma = 3\pi T \frac{1}{(2\ln(T/T_K))^2}$. (b) Flow of the imaginary part of the self energy for various values of T/T_K .

coupling function with regard to its Λ dependence is suspected to behave as

$$g^\Lambda \approx \frac{1}{2 \ln \left(\frac{\sqrt{\Lambda^2 + T^2} + (\Gamma/2)^2}{T_K} \right)} \quad (5.42)$$

which implies the form

$$g \approx \frac{1}{2 \ln \left(\frac{\sqrt{(\Gamma/2)^2 + T^2}}{T_K} \right)} \quad (5.43)$$

at the end of the flow. We shall take this both approximated forms for the vertex part to exemplify our subsequent reasoning. The crucial point in equ. (5.42) is the Λ dependence of the imaginary part and the question how, in terms of at which scale, it is generated. To begin with we direct our attention to Fig. 5.4 (b) where we display the flow of the imaginary part of the pseudo fermion self energy for the same set of values for T/T_K as above for the vertex function. It can be seen that the growth of Γ^Λ in each case sets in significantly not until Λ reaches $\approx T$. This behavior follows from the form of the kernel on the r.h.s. of (5.39) together with (5.40):

$$f(\epsilon)(1 - f(\tilde{\epsilon}))A_\Gamma(\epsilon - \tilde{\epsilon}) \quad (5.44)$$

Here A_Γ denotes again the decoherence broadened spectral function. In each case Γ^{Λ_0} is initially much smaller than temperature, which renders the spectral function to pass approximately into a δ -function. Hence, equ. (5.44) reduces to $f(\epsilon)(1 - f(\epsilon))$. From equ. (5.42) we can infer that for temperatures of the order of T_K we need a sufficiently large

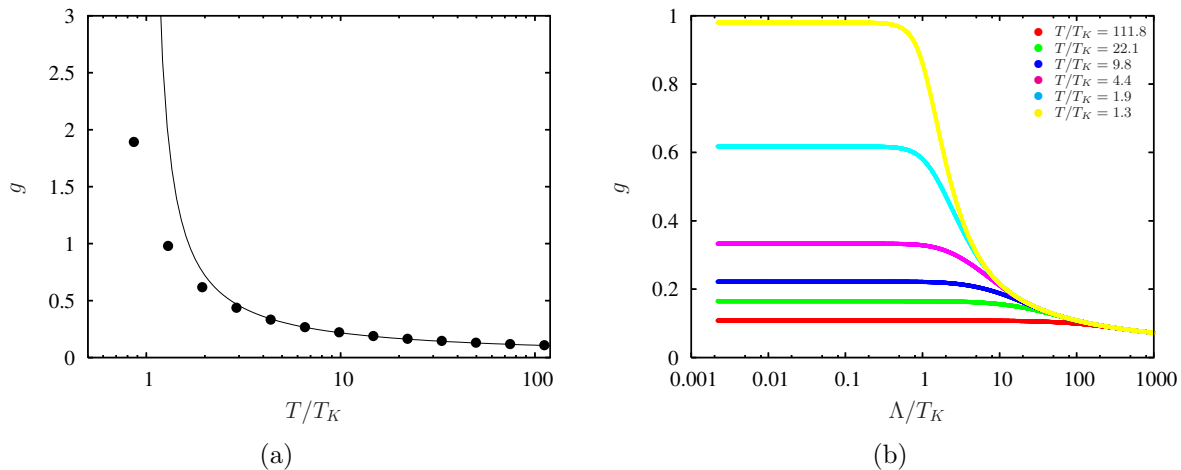


Figure 5.5: (a) Leading component of the coupling function g as a function of T/T_K for values down to $T/T_K \approx 1$. Dots represent the results from the numerical evaluation of the FRG, the solid line is given by $g = \frac{1}{2 \ln(T/T_K)}$. (b) Flow of the leading component of the vertex function for various values of T/T_K .

Γ , to be more accurate of the order of T_K , as the cutoff Λ reaches T_K in order to prevent the flow towards the strong coupling regime. This would, however, imply that we have already generated such a coupling which, by means of equation (5.44), is not possible as soon as the cutoff resides at values above T/T_K . This behavior could be entitled as a “delayed growth of the decoherence rate”.

Frequency Dependent Couplings

In this part we shall implement the frequency dependence of the vertex function. To this end we follow Rosch *et. al.* [17, 18] and we keep track only of a single frequency, the one of the incoming electron which will be denoted by ω . Further we put the external pseudo fermion energies on shell, i.e. $\omega_f = 0$ in case of zero magnetic field. Finally we approximate the Cooper and Peierls channel equ. (5.20) and (5.21) by a window function, i.e.

$$\sum_{\epsilon=\pm\Lambda} \frac{\tanh(\frac{\epsilon}{2T})(\omega - \epsilon)}{(\omega - \epsilon)^2 + (\frac{\Gamma}{2})^2} \approx \frac{\tanh(\frac{\Lambda}{2T})}{\Lambda} \Theta(\Lambda - \sqrt{\omega^2 + (\Gamma/2)^2}) \quad (5.45)$$

Hence, we obtain the following equation for the leading component

$$\partial_\Lambda g(\omega) = -2g^2(0) \frac{\tanh(\frac{\Lambda}{2T})}{\Lambda} \Theta(\Lambda - \sqrt{\omega^2 + (\Gamma/2)^2}). \quad (5.46)$$

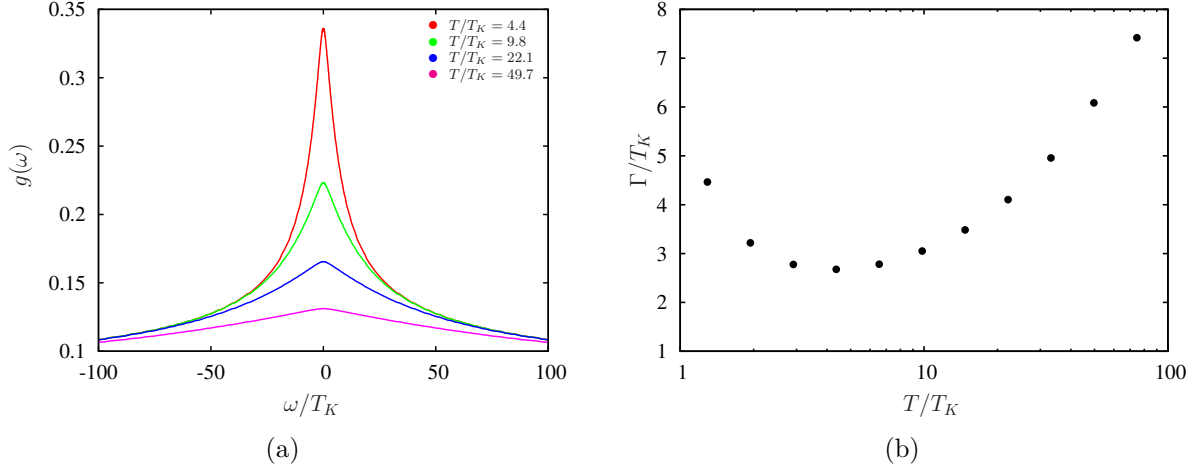


Figure 5.6: (a) Vertex function $g(\omega)$ for various temperatures which shows a pronounced peak at the resonance frequency $\omega = 0$. (b) Imaginary part of the pseudo fermion self energy as a function of T/T_K .

For the imaginary part of the pseudo fermion self energy we obtain

$$\partial_\Lambda \tilde{g}(\epsilon) = 3g^2(0) \sum_{\tilde{\epsilon}=\pm\Lambda} f(-\tilde{\epsilon}) \frac{\Gamma}{(\epsilon - \tilde{\epsilon})^2 + (\Gamma/2)^2} \quad (5.47)$$

$$\partial_\Lambda \Gamma = \sum_{\epsilon=\pm\Lambda} f(\epsilon) \tilde{g}(\epsilon). \quad (5.48)$$

In Fig. 5.6 (a) we show the vertex function for various values of the temperature as a function of ω . As expected around the resonance frequency $\omega = 0$ the vertex function shows a pronounced peak which increases in height and decreases in width as the temperature is lowered. Due to the structure of equ. 5.46 the vertex function is cut off for all frequencies by the frequency itself or by temperature in the weak coupling regime. In nonequilibrium this changes drastically (c.f. Section 5.3.4).

5.3.4 Weak Coupling at Finite Bias Voltage

In case of a finite bias voltage it is known [17, 18] that the frequency dependence of the vertex function is crucial as it—provided that one keeps track of the lead electron energy—exhibits pronounced peaks at the resonance frequencies $\omega = \pm V/2$. However, in this Section we shall begin with a brief discussion of the case of a frequency independent coupling before we turn to the frequency dependent vertex.

Frequency Independent Couplings

In the case of zero temperature and magnetic field but a finite bias voltage with $V/T_K \gg 1$ we discuss the calculations and results more briefly than in the last chapter, since the

reasoning presented in the finite temperature case can be transferred to the present case by simply replacing $T \leftrightarrow V$. To begin with we state analogous to equations (5.38), (5.39) and (5.40) the set of three equations for the leading component component of the vertex function, the imaginary part of the pseudo fermion self energy and \tilde{g} . This time we likewise assume equal couplings and already perform the spin sums. Hence, we are led to the equations

$$\partial_{\Lambda} g = - \sum_{\alpha} g^2 \tanh\left(\frac{\Lambda - \mu_{\alpha}}{2T}\right) \frac{\Lambda}{\Lambda^2 + \Gamma^2} \quad (5.49)$$

$$\partial_{\Lambda} \tilde{g}(\epsilon) = \frac{3}{2} g^2 \sum_{\tilde{\epsilon}=\pm\Lambda} \sum_{\alpha} f_{\alpha}(-\tilde{\epsilon}) \frac{\Gamma}{(\epsilon - \tilde{\epsilon})^2 + (\Gamma/2)^2} \quad (5.50)$$

$$\partial_{\Lambda} \Gamma = \sum_{\epsilon=\pm\Lambda} \sum_{\alpha} f_{\alpha}(\epsilon) \tilde{g}(\epsilon), \quad (5.51)$$

with the voltage shifted Fermi function

$$f_{\alpha}(\epsilon) = \frac{1}{\exp\left(\frac{\epsilon - \mu_{\alpha}}{T}\right) + 1}, \quad \mu_{\alpha} = \pm V/2. \quad (5.52)$$

In Fig. 5.7(a) we display the conductance G/G_0 as a function of V/T_K . Again, the dots represent the numerical evaluation of the FRG equation, whereas the solid line represents the expected analytical form $G/G_0 = \frac{3\pi^2}{16} \frac{1}{2 \ln^2(V/2T_K)}$. In Fig. 5.7 (b) we show the imaginary part of the pseudo fermion self energy as a function of V/T_K . In both cases we obtain perfect agreement with the analytical forms. As already noted, by further considerations towards the regime $V/T_K \approx 1$ we would encounter the same reasoning argued in Section 5.3.3. Hence, we will refrain from it and turn towards another domain of the weak coupling regime, namely, where we assume a sufficiently large temperature $T/T_K \gg 1$. For temperatures $T/T_K = 50, 10, 5$ we show the corresponding conductance G/G_0 in each case as a function of V/T_K in Fig. 10.1 (a). Dots are the FRG results, whereas the solid line represents the form $G/G_0 = \frac{3\pi^2}{4} g^2$ with the vertex function

$$g \approx \frac{1}{2 \ln \frac{\sqrt{(V/2)^2 + T^2}}{T_K}}. \quad (5.53)$$

As one would have expected the best agreement with the FRG solution is found for large temperatures. The dependence on V/T_K of the imaginary part of the self energy Γ is depicted in Fig. 10.1 (b). As can be seen Γ saturates to a value of the order of T_K as soon as the voltage falls below the present temperature.

Let us at the end of this section return to the discrepancies of the imaginary part of the pseudo fermion self energy in case of a vanishing and in case of a finite bias voltage. As already pointed out in Section 5.3.3 in case of a finite temperature T and vanishing bias voltage the result from the solution of the FRG equations differs slightly from the expected analytical behavior (cf. Fig. 5.3 (b)). However, in case of a finite bias voltage V and vanishing temperature the result from FRG agrees perfectly well with the expected

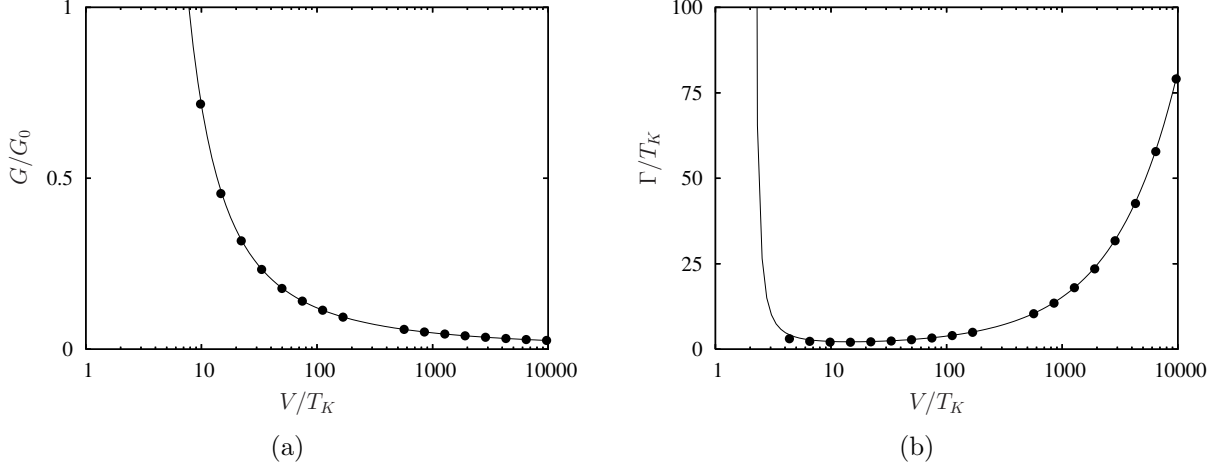


Figure 5.7: (a) Conductance in units of $G_0 = 2e^2/h$ as a function of V/T_K . Dots denote the result obtained by solving the FRG equations numerically. The solid line corresponds to the weak coupling form $G/G_0 = \frac{3\pi^2}{16} \frac{1}{\ln^2(V/2T_K)}$. (b) Imaginary part of the self energy Γ as a function of V/T_K . Dots represent again the results from the FRG, the solid line is given by $\Gamma = \frac{3}{4}\pi V \frac{1}{(2\ln(V/2T_K))^2}$. In both cases we can report good agreement with the expected analytical behavior.

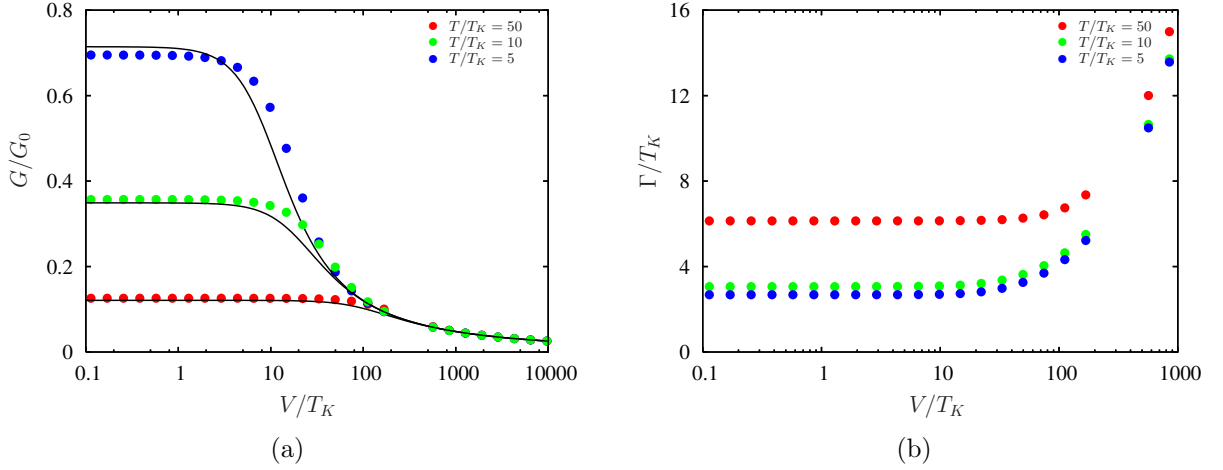


Figure 5.8: (a) Conductance in units of $G_0 = 2e^2/h$ as a function of V/T_K . Dots denote the result obtained by solving the FRG equations numerically. The solid line corresponds to the weak coupling form $G/G_0 = \frac{3\pi^2}{16} \frac{1}{\ln^2\left(\frac{\sqrt{(V/2)^2 + T^2}}{T_K}\right)}$. (b) Imaginary part of the self energy Γ as a function of V/T_K . Dots represent again the results from the FRG.

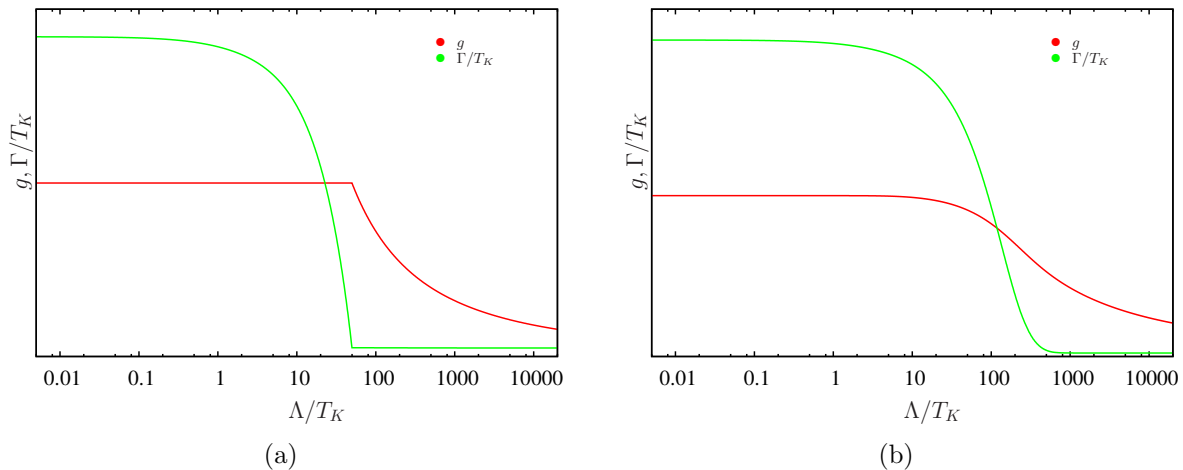


Figure 5.9: (a) Flow of the leading component g and the imaginary part of the pseudo fermion self energy for $T = 0$ and $V/T_K = 100$. (b) Flow of the leading component g and the imaginary part of the pseudo fermion self energy for $V = 0$ and $T/T_K = 100$.

analytical form (cf. Fig 5.7 (b)). To understand and illustrate this different behavior in Fig. 5.9 we show the flow of the leading component g and Γ as functions of the cutoff Λ for a finite bias $V/T_K = 100$ (Fig. 5.9 (a)) and a finite temperature $T/T_K = 100$ (Fig. 5.9 (b)). As a reminder we quote the analytical result for the imaginary part of the pseudo fermion self energy

$$\Gamma \propto \beta \frac{1}{(2 \ln(\beta/T_K))^2}, \quad \text{with } \beta = T, V/2,$$

and note again, that $\frac{1}{(2 \ln(\beta/T_K))^2}$ derives from the renormalized vertex function whereas the prefactor β arises from the integration over the Fermi functions (cf. equ. (5.44)). In case of a finite bias voltage the coupling function is seen to be cutoff sharply at $\Lambda = V/2$ —representing the sharpness of the sign-function—and the imaginary part of the pseudo fermion self energy is seen to start growing not until Λ reaches $V/2$. Hence, at $\Lambda = V/2$ the factor $1/(2 \ln(V/2T_K))^2$ has been already produced and the prefactor V is generated as $\Lambda \rightarrow 0$, thus leading precisely to the analytical form.

In case of a finite temperature this behavior appears to be different. As $\tanh(\Lambda/2T)$ is a smooth function the growths of Γ sets in already before Λ crosses T and the cutoff of the coupling function is no longer sharp. Hence, the final result appears to be smaller than the expected analytical form as during the growth of Γ the leading function is still increasing and has not yet reached its final value $1/(2 \ln(T/T_K))$.

Frequency Dependent Couplings

In the following analysis we shall follow [17, 18] and maintain the frequency of the lead electron for the vertex function. Performing the internal spin sums equ. (5.20) and

(5.21) combine and are—according to equ. (5.28)—approximated as

$$\sum_{\epsilon=\pm\Lambda} \tanh\left(\frac{\epsilon}{2T}\right) \frac{\epsilon - \Delta\omega}{(\epsilon - \Delta\omega)^2 + (\Gamma/2)^2} \approx 2 \tanh\left(\frac{\Lambda}{2T}\right) \Theta(\Lambda - \sqrt{(\Delta\omega)^2 + (\Gamma/2)^2}) \quad (5.54)$$

where $\Delta\omega = \omega - \mu_\alpha$. Hence, the equations for the leading component of the vertex function, $g(\omega)$, the imaginary part of the pseudo fermion self energy Γ and the subleading vertex component \tilde{g} take the form

$$\partial_\Lambda g(\omega) = -g^2(\omega) \frac{1}{\Lambda} \sum_\alpha \Theta(\Lambda - \sqrt{(\omega - \mu_\alpha)^2 + (\Gamma/2)^2}) \quad (5.55)$$

$$\partial_\Lambda \tilde{g}(\epsilon) = \frac{3}{2} g^2(0) \sum_{\tilde{\epsilon}=\pm\Lambda} \sum_\alpha f_\alpha(-\tilde{\epsilon}) \frac{\Gamma}{(\epsilon - \tilde{\epsilon})^2 + (\Gamma/2)^2} \quad (5.56)$$

$$\partial_\Lambda \Gamma = \frac{1}{2} \sum_{\epsilon=\pm\Lambda} \sum_\alpha f_\alpha(\epsilon) \tilde{g}(\epsilon), \quad (5.57)$$

where

$$f_\alpha(\epsilon) = \frac{1}{\exp\left(\frac{\epsilon - \mu_\alpha}{T}\right) + 1}, \quad \mu_\alpha = \pm eV/2.$$

Results of a numerical solution of these RG equations are shown in Fig. 5.10 and Fig. 5.11. In Fig. 5.10 we display $g(\omega)$ for various values of V/T_K . Fig. 5.11 shows the imaginary part of the pseudo fermion self energy Γ (dots) with the analytical behaviour $\Gamma = \frac{3\pi V}{4} \frac{1}{\log^2(V/2T_K)}$ (solid line), which is seen to agree very well in the regime $V \gg T_K$. At finite voltage the charge current I_c is approximately given by

$$I_c = \frac{3\pi^2 e}{2\hbar} \int \frac{d\omega}{2\pi} \int \frac{d\omega'}{2\pi} \int \frac{d\epsilon}{2\pi} |g(\omega, \epsilon; \omega', \epsilon + \omega - \omega')|^2 [f_L(\omega) - f_R(\omega)] A(\epsilon) A(\epsilon + \omega - \omega'). \quad (5.58)$$

In the approximation of vanishing relaxation rate Γ , the above expression simplifies to

$$I_c = \frac{3\pi e}{4\hbar} \int d\omega |g(\omega, 0; \omega, 0)|^2 [f_L(\omega) - f_R(\omega)]. \quad (5.59)$$

In Fig. 5.12 we show the conductance $G = I_c/V$ in units of G_0 as obtained from equ. (5.59) versus V/T_K . Again, dots represent the numerical evaluation of the FRG equations, whereas the solid line represents an approximate analytical form $G/G_0 = \frac{3\pi^2}{16} \frac{1}{\ln^2(V/2T_K)}$. We would obtain this analytical result if we consider only $g(\omega = 0)$ in equ. (5.55). However, due to the distinctive form of $g(\omega)$ which exhibits pronounced peaks at the resonance frequencies $\omega = \pm V/2$ the resulting $G(V)/G_0$ is slightly enlarged compared to the analytical form. In Fig. 5.14 results on the conductance G/G_0 versus V/T_K are presented for temperatures $T/T_K = 50, 10, 5$, such that one remains in the

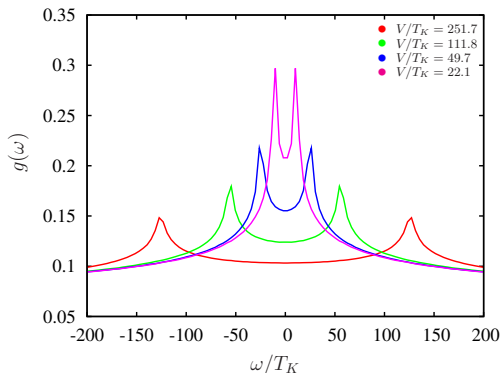


Figure 5.10: Leading component of the coupling function $g(\omega)$ versus ω/T_K for various values of V/T_K .

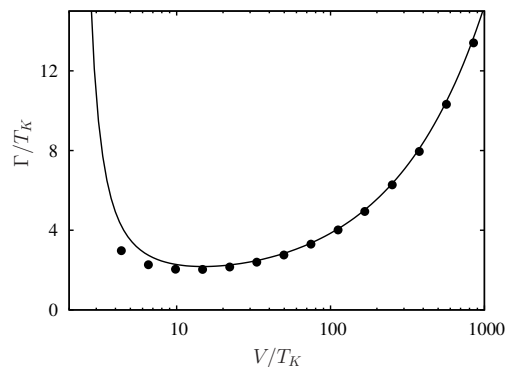


Figure 5.11: Imaginary part of the self energy Γ versus V/T_K . Dots: numerical results from FRG; solid line: $\Gamma = \frac{3\pi}{4} V \frac{1}{(2 \log(V/2T_K))^2}$.

perturbative regime even in the limit $V \rightarrow 0$. Dots are the FRG results, whereas the solid line represents $G/G_0 = \frac{3\pi^2}{4} g^2$ with the approximate vertex function

$$g(\omega = 0) \approx \frac{1}{2 \ln \frac{\sqrt{(V/2)^2 + T^2}}{T_K}}. \quad (5.60)$$

The frequency dependence of $g(\omega)$ together with the integration over the difference of the Fermi functions in the left and right lead in equ. (5.59) lead to a distinct discrepancy between the FRG result and the analytical form for $V \lesssim T$. In Fig. 5.15 results on Γ versus V/T_K in the same temperature regime as in Fig. 5.14 are shown. As can be seen, in the temperature range $3K \lesssim T \lesssim 10K$ Γ saturates to a value of the order of T_K when the voltage falls below the corresponding temperature.

5.4 Towards the Strong Coupling Regime

From the previous considerations, i.e. the analysis and the solution of the approximated set of FRG equations (5.29), (5.32) and (5.35) it can be inferred that this set of equations in its present form is not appropriate to capture the physics in the strong coupling regime, i.e. values of $T, V \ll T_K$. There are two major deficiencies in the approximate RG equations

- (i) the unitarity limit on the conductance $G \leq G_0$ is not respected since the frequency independent leading component g diverges and therewith G being proportional to g^2
- (ii) the spin relaxation rate Γ is found to rise with decreasing temperature/voltage in

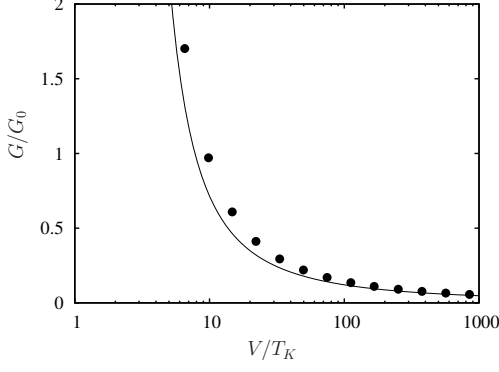


Figure 5.12: Conductance $G/G_0 = I/V$ versus V/T_K . Dots: numerical result from FRG; solid line: $G/G_0 = \frac{3\pi^2}{16 \log^2(V/2T_K)}$.

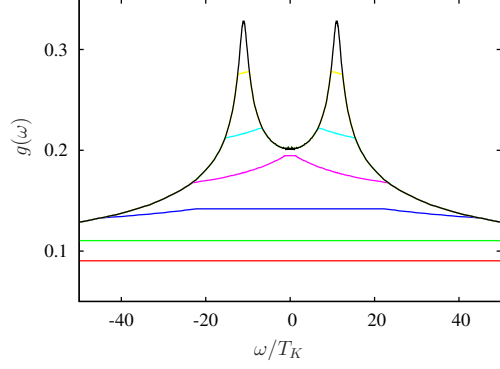


Figure 5.13: Flow of $g(\omega)$ for various values of the cutoff Λ reaching from D to 0 at $V/T_K = 30$.

the strong coupling regime, whereas Γ is expected to saturate to a value of order T_K

We shall begin our discussion by quoting an example in the literature [58, 9, 59] where the authors propose a strong coupling solution for the Kondo model in equilibrium using self-consistently renormalized pseudo fermion propagators and vertices. To this end the imaginary part of the pseudo fermion self energy $\Delta = \Gamma/2$ and the frequency independent coupling function g are calculated in second order with dressed pseudo fermion propagators and renormalized vertices by means of a so called reduced graph expansion [9, 59]. The following two equations are obtained

$$\Delta = \frac{3}{8} \Delta \frac{\left[\frac{\pi T}{\Delta} + \Psi\left(\frac{1}{2} + \frac{\Delta}{2\pi T}\right) - \Psi\left(1 + \frac{\Delta}{2\pi T}\right) \right]}{\left[\ln\left(\frac{2\pi T}{T_K}\right) + \Psi\left(\frac{1}{2} + \frac{\Delta}{2\pi T}\right) \right]^2}, \quad g = \frac{1}{2} \frac{1}{\left[\ln\left(\frac{2\pi T}{T_K}\right) + \Psi\left(\frac{1}{2} + \frac{\Delta}{2\pi T}\right) \right]}$$

where $\Psi(x)$ denotes the digamma function. In the weak coupling regime $T/T_K \gg 1$ the solutions of these self-consistent equations have the correct analytical asymptotics $\Gamma \propto T/\ln^2(T/T_K)$ and $g \propto 1/\ln(T/T_K)$. In the strong coupling regime the following solutions are obtained

$$\Delta \approx T_k + \frac{\pi\sqrt{3}}{4}T \quad \text{and} \quad g \approx \frac{4\Delta}{\pi\sqrt{3}} \frac{1}{T} \quad \text{for} \quad T/T_K \ll 1.$$

Whereas the imaginary part of the pseudo fermion self energy Δ drops down to a value of T_K , the leading logarithmic coupling constant diverges as $1/T$ as $T \rightarrow 0$, i.e. it exhibits a strong coupling form. However, when calculating the resistivity this divergency is cancelled by the pseudo fermion loop integration in the second order diagram for the conduction electron T-matrix and the low temperature Fermi-liquid result $R/R_0 \approx 1 - \frac{\pi^2}{4}(\frac{T}{T_K})^2$ is recovered and hence the unitarity limit reached as $T \rightarrow 0$.

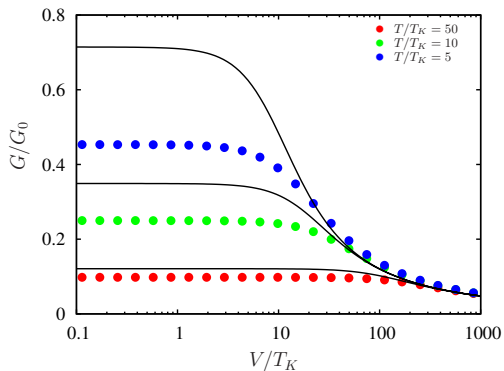


Figure 5.14: Conductance in units of $G_0 = 2e^2/h$ as a function of V/T_K . Dots denote the result obtained by solving the fRG equations numerically. The solid line corresponds to the weak coupling form $G/G_0 = 3\pi^2/16 \log^2\left(\frac{\sqrt{(V/2)^2 + T^2}}{T_K}\right)$.

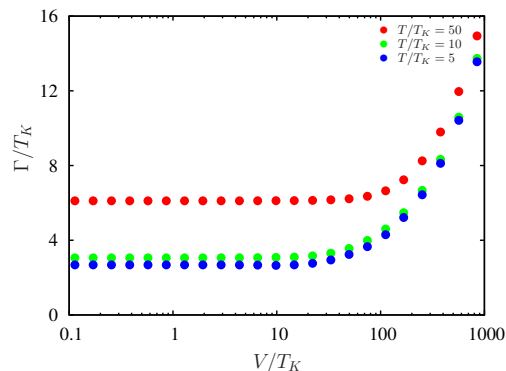


Figure 5.15: Imaginary part of the self energy Γ as a function of V/T_K . Dots represent again the results from the fRG.

A generalization of this procedure to nonequilibrium using the Keldysh technique may seem straightforward. However, in this case we would go astray as we aim for generating our results, in particular the imaginary part of the pseudo fermion self energy from a first principal method by the FRG. Nonetheless we have done such a calculation in equilibrium by means of the following self-consistent iteration: Starting point are equations (5.38), (5.39) and (5.40). We begin with a finite decoherence rate $\Delta = \Gamma/2$ and solve equ. (5.38) to obtain a renormalized coupling constant g . With this coupling constant (and the initially assumed Δ) we enter equ. (5.39) and (5.39) and, on integrating, obtain a new Δ_n

$$\Delta_n = \frac{3}{2}g^2 \int_{-D}^D \int_{-D}^D d\epsilon d\tilde{\epsilon} f(\epsilon)(1 - f(\tilde{\epsilon})) \frac{\Delta}{(\epsilon - \tilde{\epsilon})^2 + \Delta^2}.$$

We then iterate until convergence is reached. The results are shown in Fig. 5.16. The imaginary part of the pseudo fermion self energy is seen to saturate to a value of $(\Gamma/2)/T_K \approx 3.4$ after it passed through a minimum at $T/T_K \approx 6$. The leading component g and therewith the conductance saturate to values which are close to the unitarity limit.

Returning to the FRG we shall now focus on the effect of higher order correlation functions which is neglected in the approximation scheme discussed so far. The additional terms in the RG equation for the coupling function $g(\omega = 0)$ generated thereby are similar, but not identical, to the higher order loop corrections to the poor man's scaling approach and may be expected to slow down the growth of the coupling near the energy scale T_K . A quantitative control of these terms within FRG appears to be out of reach. Nonetheless, in the following we shall explore the consequences of a model

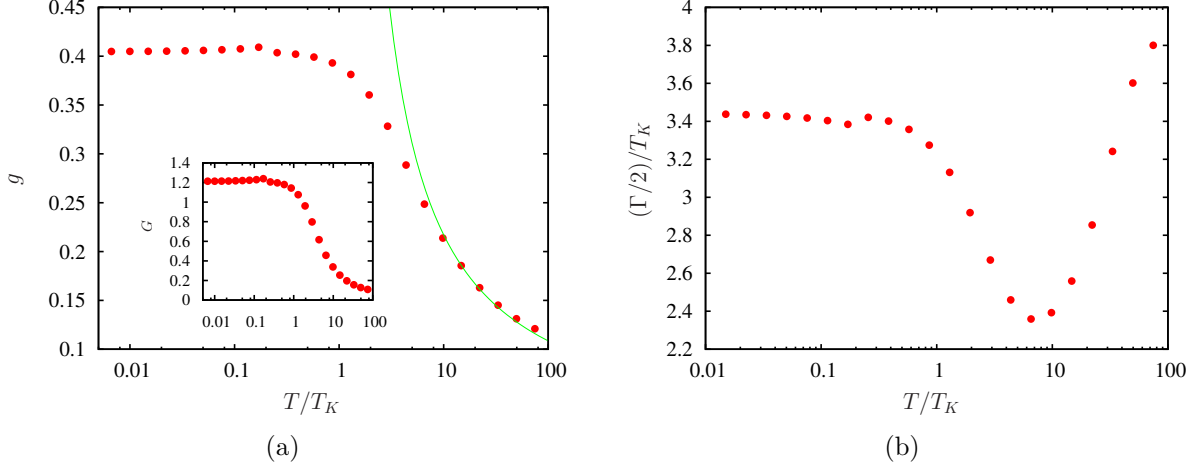


Figure 5.16: Results for the self-consistent solution as described in the text: (a) Leading component g (dots) and the weak coupling solution $g = 1/(2 \ln(T/T_K))$. The inset shows the conductance as a function of T/T_K . (b) Imaginary part of the pseudo fermion self energy Γ/T_K as functions of T/T_K .

assumption including higher order terms. To this end on the right hand side of equation for the vertex function (cf. equ. (5.38) or (5.55)) we replace g^2 by

$$g^2(1 - \alpha g - \beta g^2 - \dots). \quad (5.61)$$

with coefficients α, β to be determined by requiring that the unitarity limit be satisfied and that the resulting conductance fits the corresponding NRG result [60] best. We find that taking $\alpha = 0$ and putting $\beta = g_u^2 = 4/(3\pi)$, in equ. (5.61) leads to the best agreement with the NRG data on the linear response conductance [60]. The FRG equations (cf. 5.29, 5.32 and 5.35) then take the following form

$$\partial_\Lambda g = -g^2 [1 - (g/g_u)^2] \frac{\Lambda}{\Lambda^2 + \Gamma^2(\Lambda)} \sum_\alpha \tanh\left(\frac{\Lambda - \mu_\alpha}{2T}\right) \quad (5.62)$$

$$\partial_\Lambda \Gamma(\omega) = \frac{1}{2} \sum_{\epsilon=\pm\Lambda} \sum_\alpha [f_\alpha(\epsilon) \tilde{g}^>(\epsilon, \omega) + (1 - f_\alpha(\epsilon)) \tilde{g}^<(\epsilon, \omega)] \quad (5.63)$$

$$\partial_\Lambda \tilde{g}^>(\epsilon, \omega) = \frac{3}{4} g^2 \sum_{\tilde{\epsilon}=\pm\Lambda} \sum_\alpha \frac{\Gamma(\omega + \epsilon - \tilde{\epsilon})}{(\omega + \epsilon - \tilde{\epsilon})^2 + \Gamma^2(\omega + \epsilon - \tilde{\epsilon})} (1 - f_\alpha(\tilde{\epsilon})) \quad (5.64)$$

$$\partial_\Lambda \tilde{g}^<(\epsilon, \omega) = \frac{3}{4} g^2 \sum_{\tilde{\epsilon}=\pm\Lambda} \sum_\alpha \frac{\Gamma(\omega + \epsilon - \tilde{\epsilon})}{(\omega + \epsilon - \tilde{\epsilon})^2 + \Gamma^2(\omega + \epsilon - \tilde{\epsilon})} f_\alpha(\tilde{\epsilon}). \quad (5.65)$$

Here we keep the frequency dependence of $\Gamma(\omega)$. Within the pseudo fermion projection scheme using the limit $\lambda \rightarrow \infty$ the self energy acquires a highly asymmetric form, which causes problems in the numerical solution. We therefore choose an alternative

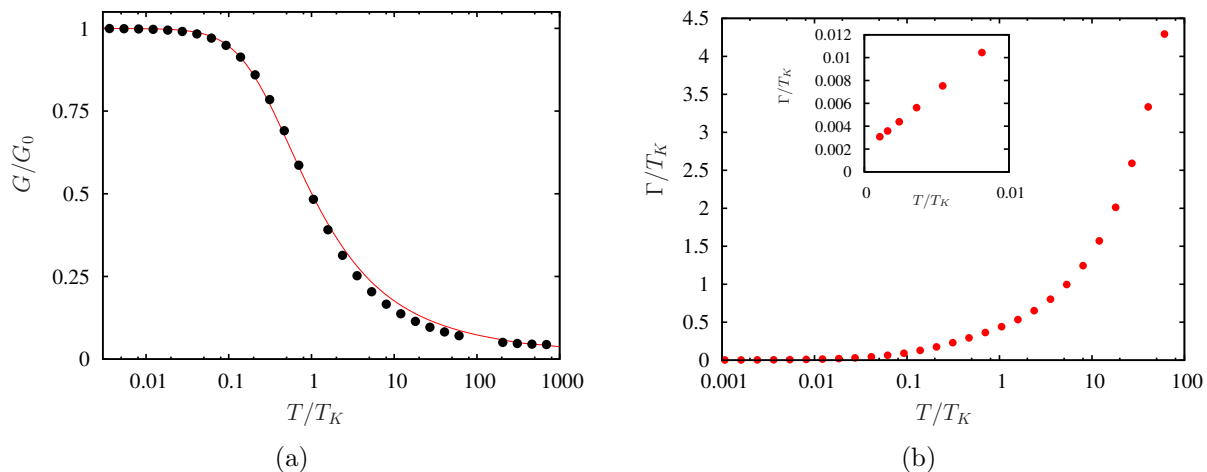


Figure 5.17: (a) Comparison of the linear conductance $G(T)$ from FRG (dots) with the result obtained via the NRG [60]. Here, the Kondo temperature is defined by $G(T_K) = G_0/2$. (b) Imaginary part of the pseudo fermion self energy at $\omega = 0$ as a function of T/T_K on a logarithmic scale. Inset: Region near $T/T_K = 0$ on a linear scale.

projection with $\lambda = 0$, which requires to introduce normalization factors accounting for the difference in the impurity partition function with and without projection. In the calculation of $\Gamma(\omega)$ in the absence of a magnetic field these factors are not necessary. This choice has the advantage of particle-hole symmetry, i.e. $\Gamma(\omega) = \Gamma(-\omega)$.

Fig. 5.17(a) shows a comparison of the linear conductance from FRG (dots) with the NRG data [60]. For the purpose of this comparison we adopted the definition of a Kondo temperature T_K^* used in [60]: $G(T_K^*) = G_0/2$. This differs from our previous definition of $T_K = D_0 \exp(-1/(2g_0))$ by a factor $T_K^*/T_K \approx 2.76$. We find excellent agreement between the FRG and NRG results. In Fig. 5.17(b) we show the imaginary part of the pseudo fermion self energy $\Gamma(\omega = 0)$ as a function of T/T_K . The inset shows the region $T \ll T_K$, where Γ again decreases almost linearly with decreasing temperature, down to a similar residual value of $\Gamma/T_K \approx 0.002$ as found from the weak coupling FRG equation above.

We now turn to the nonequilibrium situation: In Fig. 5.18(a) we show the conductance as a function of the voltage. The lines indicate the half width at half maximum which amounts to $\Delta V = 1.93T_K$. Fig. 5.18(b) shows $\Gamma(\omega = 0)$ as a function of V/T_K . In the inset Γ is seen to drop linearly with decreasing voltage at $V \ll T_K$, down to a residual value of $\Gamma/T_K \approx 0.002$.

To summarize, adding a fourth order term with adjusted coefficient to the β -function of the RG equation for the coupling $g(\omega = 0)$ leads to good agreement with the exactly known conductance in the limit $V \rightarrow 0$. The relaxation rate $\Gamma(\omega = 0)$, however, comes out three orders of magnitude too small. We conclude that higher order terms in the β -function are not sufficient to cure the problem with Γ . In addition, the frequency

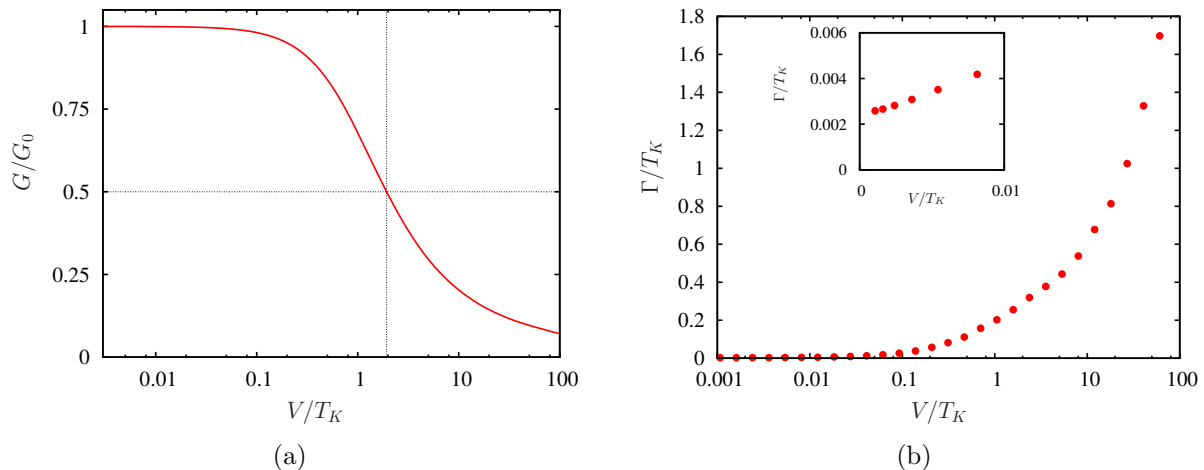


Figure 5.18: (a) Conductance $G(V)$ at zero temperature obtained from FRG. The lines indicate the half width at half maximum which amounts to $\Delta V = 1.93T_K$. (b) Imaginary part of the pseudo fermion self energy at $\omega = 0$ as a function of V/T_K on a logarithmic scale. Inset: Region near $V/T_K = 0$ on a linear scale.

dependence of both, g and Γ is essential in reaching the Fermi liquid regime, as we now sketch.

First we note that unitarity does not require $g(\omega)$ to be bounded at all frequencies. It appears possible to have $g(\omega = 0)$ growing large or even diverging at strong coupling, while the conductance G remains finite. This is because $G = dI_c/dV$ with the charge current I_c as given by equ. (5.58) is given by integrating the product of two g 's over energy. The energy integration removes any singular behavior of $g(\omega)$ at $\omega = 0$ provided the singularity is not too strong. Secondly, a sufficiently strong relaxation rate Γ might suppress the unphysical growth of G . As discussed in detail in Section 5.3.3 and 5.3.4 the RG equations in the approximation of taking all energies on shell do not generate a sufficiently strong $\Gamma(\omega = 0)$ at the scale $\Lambda \simeq T_K$, where it would be needed to cut off the growth of g , for the reasons discussed above. On the other hand, Γ at $\Lambda = 0$ turned out to grow too large at $T \ll T_K$. This deficient behavior may also be remedied by taking the energy dependence of Γ and g into account. Qualitatively one expects that the smearing of the sharp singular structures in $g(\omega)$ and $\Gamma(\omega)$ by integrations over ω within the width Γ specified by the pseudofermion spectral functions will be equivalent to replacing $g(\omega = 0)$ and $\Gamma(\omega = 0)$ by $g(\omega \simeq \Gamma)$ and $\Gamma(\omega \simeq \Gamma)$, which are both finite quantities of $O(1)$ and $O(T_K)$, respectively, not only at the end of the RG process (at $\Lambda = 0$), but already at $\Lambda \approx T_K$.

6 Experimental Overview

6.1 Introduction

Due to an immense progress in nanotechnology the Kondo effect experienced a “revival” [1, 32] during the last decade. It became possible to create so called quantum dots which confine a small droplet of electrons in a finite, tiny region of space. Contrary to the Kondo effect in metals, where a magnetic impurity is embedded in a bulk of conduction electrons the foundation of all experiments in the past few years was the imitation of the Kondo situation by pinching the impurity between two fermionic reservoirs, i.e. the spin of an unpaired electron on such a quantum dot device acts as the magnetic impurity. Depending on if these leads are subject to a finite bias voltage or if only the limit of vanishing bias voltage, the so called linear response regime, is considered the system represents either the nonequilibrium or the equilibrium Kondo dot model, respectively. In these quantum dot systems the Kondo effect manifests itself in an enhancement of the conductance as the temperature is decreased. Several attempts, where the experimentalists [19, 20, 21] found a weak Kondo effect, i.e. an enhancement of the conductivity of about 20% , were necessary until the strong Kondo effect, where the conductance reaches the unitary limit, was finally observed in 2000 by van der Wiel *et. al.* [22].

In this section we shall first give a short introduction about the mode of operation of such quantum dot devices and additionally provide a short overview of recent experiments [19, 22, 21, 20] in equilibrium in Section 6.2 before we turn to the nonequilibrium system [23] in Section 6.3.

6.2 Kondo Quantum Dots in Equilibrium

To begin with we consider a typical experimental setup [19, 20] as shown in Fig. 6.2. The fermionic leads, reservoirs of two-dimensional electron gases, which are located at top and bottom are referred to as source (S) and drain (V). As a finite bias voltage drives the system out of equilibrium, the limit of a vanishing bias voltage represents the equilibrium situation.

Three gate electrodes, the one on the right and the upper and lower ones on the left, control the tunnel amplitude Γ of electronic states on the dot to those in the leads. The middle electrode on the left is used as a gate to change the energy of the dot region relative to the leads. Hence, this gate voltage V_g controls the number of electrons N on the quantum dot (QD) as it shifts the corresponding energy levels of the dot region. This is illustrated in Fig. 6.2 (a). In Fig. 6.2 (b) we show the occupancy n_d of the lowest

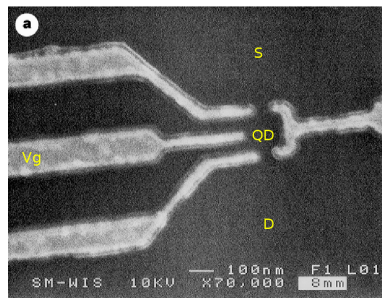


Figure 6.1: Experimental setup [19, 20] for a quantum dot (QD) with applied gate voltage (V_g) and a dc bias voltage between source (S) and drain (V). A set of electrodes, on the surface of a GaAs/AlGaAs heterostructure is used to to confine the electrons and create the tunnel barriers. The dot region itself has dimension of 100nm square.

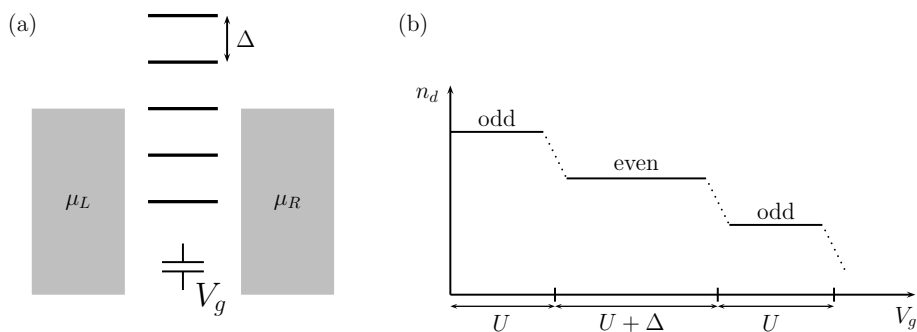


Figure 6.2: (a) Sketch of a quantum dot coupled to fermionic leads in the linear response regime where $\mu_L - \mu_R \approx 0$. The gate voltage V_g controls the position of the dot levels with respect to the Fermi energy of the lead electrons. The level spacing amounts to Δ . (b) Occupancy of the quantum dot n_d as a function of the gate voltage V_g .

occupied level of the quantum dot as a function of the gate voltage. As a variation of the gate voltage results in adding an electron to the dot each time V_g is increased by a fixed increment proportional to U and as current through the dot can flow only if the island is free to fluctuate between N and $N + 1$ electrons a plot of the conductance against the gate voltage shows periodically spaced peaks (cf. red curve of Fig. 6.3(a)) which are referred to as Coulomb oscillations. The regions between enhanced conductance peaks are known as Coulomb valleys. Hence, the peaks appear each time when the number of electrons on the dot changes from N to $N \pm 1$. The spacing between two peaks, which include a valley corresponding to an odd number of electrons, is given by U as the two electrons corresponding to this pair of peaks are added to the same spatial state. On the contrary, when the number of electrons is even the next electron must be placed in a different spatial state giving rise to a spacing of $U + \Delta$. If a spin-degenerate filling of the

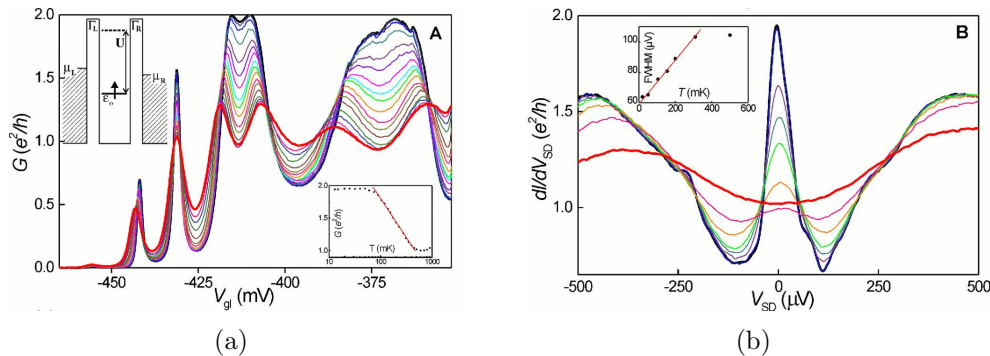


Figure 6.3: Measurements from [22] of the dependence of (a) the conductance G on the gate voltage V_g and (b) differential conductance $\frac{dI}{dV}$ on voltage V between source and drain. In both cases a temperature regime from $T \approx 15$ mK (black curve) up to $T = 900$ mK (red curve). The inset in (a) shows $G(T)$ for fixed $V_g = -413$ mV.

levels is assumed the total spin on the dot is zero and the dot is non-magnetic when N is even, whereas it is $\pm 1/2$ for odd N and the dot possess a net spin magnetic moment. Hence, one may use these “Quantum Dots as Tunable Kondo Impurities” [61, 21]. Let us return to Fig. 6.3(a), where the differential conductance $G = \frac{dI}{dV}$ is shown as a function of the gate voltage. For high temperatures (900 mK, red curve) again there is a clear evidence of Coulomb oscillations. Decreasing the temperature down to the base temperature (15 mK, black curve) manifests itself completely different in valleys with an even number of electrons and those with an odd number of electrons. If N is even the conductivity decreases as the temperature is lowered as one might have expected. However, if N is odd the unpaired electron with a free spin forms a singlet with electrons at the Fermi level of the leads. This results from effective spin flip processes which effectively screen the local spin and in turn lead to a macroscopically correlated state which gives rise to the Kondo effect. In a quantum dot, the Kondo effect derives from this correlation mediated narrow peak in the density of states at the Fermi level of the leads. This Kondo resonance gives rise to enhanced conductance through the dot.

Fixing the gate voltage at the middle of a Kondo plateau (inset of Fig. 6.3(a) at -413 mV) one can extract the $G(T)$ dependence which shows a logarithmic behavior before it saturates to the unitary limit $G_0 = 2e^2/h$. This is further investigated in Fig. 6.4(a) and Fig. 6.4(b). The upper panel of Fig. 6.4(a) shows an enlarged cutout of the $G(V_g)$ dependence within one Coulomb valley with an odd number of electrons. The lower panel shows the Kondo temperature versus V_g . For each gate voltage one obtains T_K by fitting G to the empirical Kondo form

$$G(T) = \frac{G_0}{\left[1 + \left(\frac{T}{T_K}\right)^2\right]^s}, \quad (6.1)$$

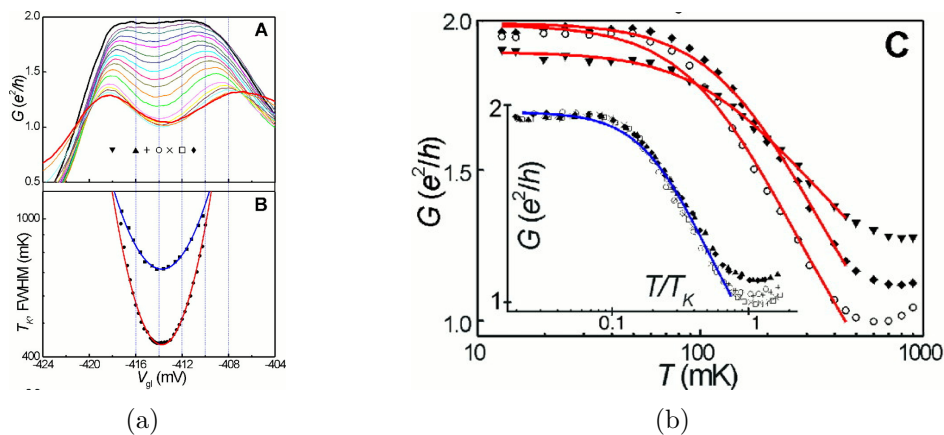


Figure 6.4: (a) Upper panel: Differential conductance $G(V_g)$ for T ranging from 15mK (black curve) up to 900mK (red curve). Lower panel: Kondo temperature T_K versus gate voltage. (b) Conductance $G(T)$ at fixed gate voltage for several values of V_g . The inset shows that G versus normalized temperature T/T_K scales to a single curve.

which in turn is a result of a fit to numerical renormalization group calculations [20, 62]. In this formula $T'_K = T_K/(2^{1/s} - 1)^{1/2}$ is defined such that T_K is given as the temperature at which the Kondo conductance is half of its extrapolated zero-temperature value $G(T_K) = G_0/2$. The parameter s , which determines the steepness of the conductance drop with increasing temperature amounts to $s \approx 0.2$. Fig. 6.4(b) finally contains the conductance versus temperature for various fixed values of the gate voltage (i.e. the temperature dependence along the thin vertical lines of Fig. 6.4(a)). If these functions are scaled by the Kondo temperature T_K as obtained from the lower panel of Fig. 6.4(a) the various curves are seen (cf. inset of Fig. 6.4(b)) to follow a universal form.

6.3 Kondo Quantum Dots out of Equilibrium

So far we have restricted our considerations to the the linear response regime, i.e. the limit of a vanishing external bias voltage. The experiments in [19, 22, 21, 20] already analyzed the case of a finite bias voltage (cf. also Fig. 6.3(b)) but could not provide any reliable low-energy scaling behavior as these existing experiments have focused on higher energies ($eV \sim kT_K$). A first close examination of the transport properties in the low bias and low temperature regime were performed in 2008 by Grobis *et. al.* [23]. It is found that the conductance at low energies is consistent with universality between temperature and bias and is characterized by a quadratic dependence. In Fig. 6.5(c) the dependence of the differential conductance $G(V)$ is shown as a function of the bias voltage for temperatures ranging from 205mK down to 13mK (the measurements have been performed in the middle of the Kondo plateau at $V_G = -213$ mV, cf. Fig.6.5(d)). For low temperatures (13mK, black curve) the differential conductance has a pronounced

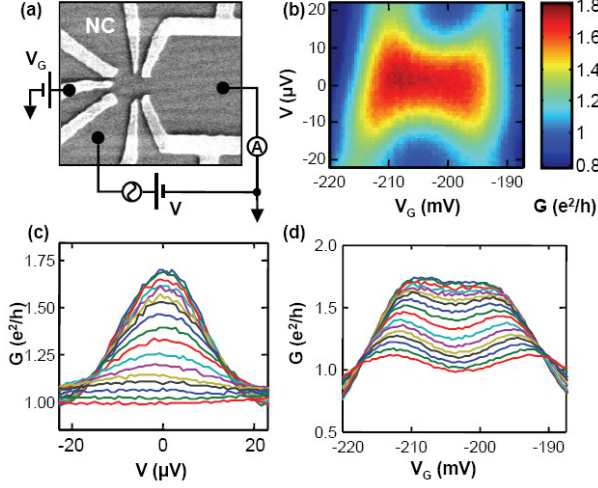


Figure 6.5: (a) Quantum dot device with an overlaid measurement schematic. (b) Differential conductance (G) measurements as a function of the gate voltage V_G and source-drain bias V at $T = 13\text{mK}$. (c) Temperature dependence of the Kondo peak in the conductance for $T = 13 - 205\text{mK}$ at $V_G = -203\text{mV}$. (d) Temperature dependence of the Kondo plateau for $T = 13 - 205\text{mK}$ at $V = 0\mu\text{V}$.

peak around $V = 0$, which is referred to as the “zero bias anomaly”. The following low bias expansion is found to be applicable over a wide temperature range [63, 64]

$$G(T, V) = G(T) \left(1 - \frac{c_T \alpha}{1 + c_T (\gamma/\alpha - 1) (T/T_K)^2} \left(\frac{V}{T_K} \right)^2 \right) \quad (6.2)$$

where $G(T)$ is given by the empirical Kondo form equ. (6.1) and the parameter $c_T \approx 5.49$ is determined from the low temperature expansion of this equation: $G(T) \approx (1 - c_T (T/T_K)^2)$. The form equ. (6.2) is chosen such that it reduces for small temperatures to the universal scaling function expansion which was suggested by Schiller *et. al.* [65]

$$\frac{G(T, 0) - G(T, V)}{c_T G_0} \approx \alpha \left(\frac{V}{T_K} \right)^2 - c_T \gamma \left(\frac{T}{T_K} \right)^2 \left(\frac{V}{T_K} \right)^2 \quad (6.3)$$

The coefficients α and γ characterize the zero-temperature curvature and the broadening of the Kondo peak respectively. The authors find $\alpha \approx 0.1$ and $\gamma \approx 0.5$.

7 Conclusion and Outlook

In the first part of this thesis we have extended the functional renormalization group method to nonequilibrium and have applied it to the Kondo dot model. As a first step we derived a set of coupled differential equations for the imaginary part of the pseudo fermion self energy and the two particle vertex function both obeying the full frequency dependence and Keldysh matrix structure. From this general set of equations we have in a second step extracted an approximated set of equations as we have focused on the leading logarithmic terms of the vertex function which eventually lead to the Kondo effect. Upon keeping track of the leading components only the Keldysh matrix structure of the coupling function was seen to reduce to the structure of the bare vertex which caused an enormous simplification of the FRG equations.

We then passed on to the solution and analysis of the approximated set of FRG equations in and out of equilibrium in the weak coupling regime $T, V \gg T_K$. In particular we have focussed on how the decoherence rate is generated and build in by the FRG. For a frequency dependent coupling in nonequilibrium this rate is instrumental as the coupling function is *not* for all frequencies cutoff by the voltage or the frequency itself, respectively. However, for frequency independent couplings the decoherence rate is not crucial since the flow of the leading component of the coupling function is cutoff by the voltage or, respectively, temperature. As a physical observable we have focused on the conductance which derives as an expression in terms of the renormalized coupling function. We obtain perfect agreement compared to known results for the conductance and—though not crucial as a cutoff—decoherence rate.

Towards the strong coupling regime we have first focused on the regime $T, V \approx T_K$, investigated the behavior and analyzed the breakdown of the present, approximated set of differential equations. The major problem hereby was caused by the decoherence rate which reveals some kind of “delayed growth” in order to cutoff the RG flow before the strong coupling regime is entered. We have discussed the approach to the strong coupling regime, that is under which condition the latter may be reached. Finally, we gave some preliminary results for the strong coupling regime which show a rather impressive accordance with numerical renormalization group results for the linear conductance.

Part II

Magnetic Excitations from Cite-Centered Stripes in CuO Superconductors

8 Introduction

Since its discovery in 1986 [66], high-transition-temperature superconducting compounds like lanthanum barium copper oxide (LBCO) have been in the focus of theoretical as well as experimental analysis. The main constituent of all these compounds are the CuO_2 -planes from which the interesting physics originates, leading to a rich phase diagram and possessing an extremely rich phenomenology. Starting from a perfect realization of a two dimensional antiferromagnet at zero doping and temperature [67, 68], the system enters a superconducting regime, whereas at a narrow region around $x = 1/8$ superconductivity is anomalously suppressed [69].

The present work refers to a neutron scattering experiment by Tranquada *et al.* [70] on the stripe ordered compound $\text{La}_{2-x}\text{Ba}_x\text{CuO}_4$ at a doping level of $x = 1/8$, finding that the excitation at energies near the magnetic resonance peak, and in particular for the entire region up to almost 200meV above, are quite similar to compounds without stripe order. This was a highly surprising result, since the spectrum for a stripe compound was predicted to look different, but even more though because it suddenly offered an explanation for the spectrum of YBaCuO in terms of stripes. This result has far reaching consequences: To begin with, it suggests that the stripes are bond-centered rather than site-centered, which is a long standing open question for the striped cuprates and suggests a possible relation to the fundamental mechanism of superconductivity in general [70]. The role of stripes in the framework of superconductivity and their characteristics has been discussed intensively [71, 72, 73, 74, 75].

More refined calculations showing that Tranquada's interpretation of the spectrum in terms of bond-centred stripes is fully consistent with the data were provided independently by Vojta *et al.* [76] and Uhrig *et al.* [77], performing a bond operator based spin wave analysis of ferromagnetically coupled two leg ladders. Extending this perspective, subsequent works addressed various issues related to the implications and characteristics of stripe phenomena in the cuprate compounds [78, 79, 80, 81, 82, 83, 84, 85, 86]. The fact that this apparently tentative explanation is consistent with the data, however, does not render it to be the only possible one. In fact, as we will show in our subsequent analysis, the data are equally well explained by assuming site-centred stripes and even more we shall show that there is a clear evidence for site- rather than bond-centered stripes (cf. Fig. 8.1).

In particular, in this work we perform a spin-wave analysis of coupled three-leg ladders through a bond operator representation of the rungs containing three spins each. Besides the conclusion of our study that there is evidence for site-centered stripes, which displayed one of the main open question ever since the discovery of the stripe phenomenology in general, even more importantly our result puts a question mark behind the second conclusion by Tranquada that stripe correlations are essential to high-transition-

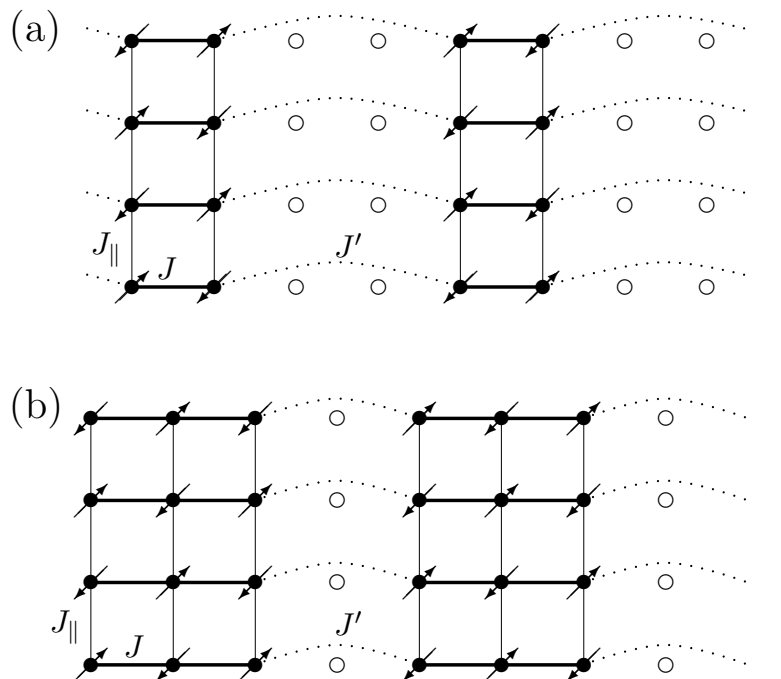


Figure 8.1: Bond- vs. site-centered stripe models: (a) Bond-centered stripes are modeled by ferromagnetically coupled two leg ladders whereas (b) site-centered stripes correspond to antiferromagnetically coupled three-leg spin ladders.

temperature superconductivity. If the spectrum observed can be explained with such widely different models - a model of ferromagnetically coupled, gapped two-leg spin ladders vs. a model of antiferromagnetically coupled, gapless three-leg ladder - it may just as well be that the spectrum, and in particular the high energy spectrum above 50 meV which was previously interpreted as evidence for two-leg ladders, is a generic property of the doped square-lattice antiferromagnet, and does not rely on stripe correlations at all.

This part of the work is organized as follows: In **Chapter 7** we introduce a bond-operator formalism for a single rung of a three leg spin ladder, i.e. three antiferromagnetically coupled $S = 1/2$ spins. The description of excitations out of the two-fold degenerate ground state, which we take to be an interpolation of the quantum ground state of the rung and the classically Néel ordered state is implemented by a set of bosonic creation and annihilation operators. By coupling these single rungs to form a three-leg spin ladder and then coupling these spin ladders antiferromagnetically we generate our spin model (cf. Fig. 8.1 (b)) and adjust the ground state in an appropriate way. We then perform a harmonic approximation of our model, i.e. we only keep bilinear terms in the expansion of the model via the bosonic operators, followed by a Fourier transform of the Hamiltonian. Subsequently, the excitation spectrum is obtained via a Bogoliubov transformation. **Chapter 8** contains the main body of the second part of this thesis, the analysis and discussion of the results. To begin with we present a method to estimate the antiferromagnetic coupling J' between the individual three-leg ladders. Additionally, we

estimate the ferromagnetic coupling for the case of coupled two-leg ladders, i.e. in case of the bond-centered model, and find that only the site-centered model orders. We then compare our calculated results for the lowest eigenmode and constant energy cuts for the spin susceptibility to the experimental data by Tranquada. Furthermore, we focus on the dependence of the saddle point energy at the antiferromagnetic wave vector $\omega(\pi, \pi)$ on the inter-ladder coupling J' . This part is finally closed by a conclusion in **Chapter 9**.

As in the first part of this thesis we shall postpone most of the technical and elaborate calculations and the formalism in the appendices. **Appendix F** provides a list of matrix elements of the spin operators on single rungs. **Appendix G** contains an analysis of the parts of the Hamiltonian which do not influence the low energy part of the excitation spectrum we are interested in. However, these parts are essential for the evaluation of the ground state energy. A detailed calculation of the neutron scattering intensity can be found in **Appendix H**. Finally **Appendix I** details how we calculate the staggered magnetization.

9 Theory and Method

9.1 Introduction

In this Chapter we provide the theoretical framework towards our main goal, the description of magnetic excitations from site-centered stripes in the CuO planes of high temperature superconductors. To begin with we introduce a bond operator formalism for three-leg ladders in Section 9.2. It is based on a set of bosonic operators that specify the excitations out of the doubly degenerate groundstate of a bipartite lattice which consists of single three-leg rungs. The ground state of the rungs is taken to be a superposition of the quantum ground state and the classical Néel state. In the subsequent Section 9.3 we couple the single rungs to form a spin ladder and afterwards link these individual ladders to produce our desired model, a two-dimensional array of antiferromagnetically coupled three-leg ladders. The ground state is thereby adjusted in a way such that terms linear in the bosonic operators, which occur as we expand the Hamiltonian, identically vanish. In Section 9.4, we expand the Hamiltonian in terms of the bosonic creation and annihilation operators and perform a harmonic approximation as we keep only terms which are bilinear in these operators. After a Fourier transformation we solve this Hamiltonian via a Bogoliubov transformation in Section 9.5.

9.2 Basis States for Three-Site Rungs

Consider a single rung of a three leg ladder, consisting of spins which are antiferromagnetically coupled with a coupling J we set to unity (see Fig. 9.1). For later purposes, let

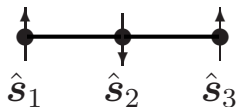


Figure 9.1: Single rung on sublattice \mathcal{A}

us assume this rung belongs to sublattice \mathcal{A} , i.e. set up conventions the rungs belonging to sublattice \mathcal{A} will inherit in the following sections. If we denoting the $SU(2)$ spin operators for the three spin $\frac{1}{2}$'s on the sites by $\mathbf{s}_1, \mathbf{s}_2$, and \mathbf{s}_3 , the Hamiltonian for the rung takes the form

$$\hat{H}^{\mathcal{A}} = \hat{\mathbf{s}}_1 \hat{\mathbf{s}}_2 + \hat{\mathbf{s}}_2 \hat{\mathbf{s}}_3. \quad (9.1)$$

Diagonalization yields the following eigenvalues and eigenvectors:

$$\begin{aligned}
E = -1 & \begin{cases} |b_{-1/2}\rangle &= -\frac{1}{\sqrt{6}}(|\uparrow\downarrow\downarrow\rangle - 2|\downarrow\uparrow\downarrow\rangle + |\downarrow\downarrow\uparrow\rangle) \\ |b_{1/2}\rangle &= -\frac{1}{\sqrt{6}}(|\downarrow\uparrow\uparrow\rangle - 2|\uparrow\downarrow\uparrow\rangle + |\uparrow\uparrow\downarrow\rangle) \end{cases} \\
E = 0 & \begin{cases} |a_{-1/2}\rangle &= \frac{1}{\sqrt{2}}(|\uparrow\downarrow\downarrow\rangle - |\downarrow\downarrow\uparrow\rangle) \\ |a_{1/2}\rangle &= \frac{1}{\sqrt{2}}(|\downarrow\uparrow\uparrow\rangle - |\uparrow\uparrow\downarrow\rangle) \end{cases} \\
E = \frac{1}{2} & \begin{cases} |c_{-3/2}\rangle &= |\downarrow\downarrow\downarrow\rangle \\ |c_{-1/2}\rangle &= \frac{1}{\sqrt{3}}(|\downarrow\downarrow\uparrow\rangle + |\downarrow\uparrow\downarrow\rangle + |\uparrow\downarrow\downarrow\rangle) \\ |c_{1/2}\rangle &= \frac{1}{\sqrt{3}}(|\uparrow\uparrow\downarrow\rangle + |\uparrow\downarrow\uparrow\rangle + |\downarrow\uparrow\uparrow\rangle) \\ |c_{3/2}\rangle &= |\uparrow\uparrow\uparrow\rangle. \end{cases} \tag{9.2}
\end{aligned}$$

Note that the two states $|a_{-1/2}\rangle$ and $|a_{1/2}\rangle$ are antisymmetric under spacial reflections interchanging sites 1 and 3 on the rung, while all other states are symmetric. This distinction will prove useful when expanding the Hamiltonian for the coupled ladders in Section 9.4 below. We denote the orthonormal basis formed by these eight states by

$$M = \{|b_{-1/2}\rangle, |b_{1/2}\rangle, |a_{-1/2}\rangle, |a_{1/2}\rangle, |c_{-3/2}\rangle, |c_{-1/2}\rangle, |c_{1/2}\rangle, |c_{3/2}\rangle\}. \tag{9.3}$$

In this basis, the Hamiltonian matrix is trivially given by

$$\begin{aligned}
\hat{H}^A &= -(|b_{-1/2}\rangle\langle b_{-1/2}| + |b_{1/2}\rangle\langle b_{1/2}|) \\
&+ \frac{1}{2}(|c_{-3/2}\rangle\langle c_{-3/2}| + |c_{-1/2}\rangle\langle c_{-1/2}| + |c_{1/2}\rangle\langle c_{1/2}| + |c_{3/2}\rangle\langle c_{3/2}|). \tag{9.4}
\end{aligned}$$

Neither of these exact eigenstates, however, is suited as a fiducial state for spin wave theory. We are hence led to define a vacuum state

$$\begin{aligned}
|\tilde{b}_{-1/2}\rangle &\equiv |b_{-1/2}\rangle \cos \phi + |c_{-1/2}\rangle \sin \phi \\
&= (|\uparrow\downarrow\downarrow\rangle + |\downarrow\downarrow\uparrow\rangle) \left(-\frac{1}{\sqrt{6}} \cos \phi + \frac{1}{\sqrt{3}} \sin \phi\right) + |\downarrow\uparrow\downarrow\rangle \left(\sqrt{\frac{2}{3}} \cos \phi + \frac{1}{\sqrt{3}} \sin \phi\right), \tag{9.5}
\end{aligned}$$

which interpolates between the quantum ground state $|b_{-1/2}\rangle$ of the isolated rung with $S^z = -\frac{1}{2}$ for $\phi = 0$ and the classically Néel ordered state $|\uparrow\downarrow\uparrow\rangle$ for $\phi = \arctan(\frac{1}{\sqrt{2}}) = 0.6155$. The parameter ϕ will depend on the coupling between the rungs and the ladders. The motivation for introducing the state $|\tilde{b}_{-1/2}\rangle$ will become clear as we determine ϕ self-consistently below. Since we wish $|\tilde{b}_{-1/2}\rangle$ to be one of our basis states, we replace (9.3) by

$$\begin{aligned}
M^A &= \{|\mu\rangle^A; \mu = 1, \dots, 8\} \\
&= \{|\tilde{b}_{-1/2}\rangle, |b_{1/2}\rangle, |a_{-1/2}\rangle, |a_{1/2}\rangle, |c_{-3/2}\rangle, |\tilde{c}_{-1/2}\rangle, |c_{1/2}\rangle, |c_{3/2}\rangle\}, \tag{9.6}
\end{aligned}$$

with

$$\begin{pmatrix} |b_{-1/2}\rangle \\ |c_{-1/2}\rangle \end{pmatrix} = \begin{pmatrix} u & -v \\ v & u \end{pmatrix} \begin{pmatrix} |\tilde{b}_{-1/2}\rangle \\ |\tilde{c}_{-1/2}\rangle \end{pmatrix} \tag{9.7}$$

and $u = \cos \phi$, $v = \sin \phi$. The relevant terms in the Hamiltonian (9.4) transform into

$$\begin{aligned} & (|b_{-1/2}\rangle, |c_{-1/2}\rangle) \begin{pmatrix} -1 & 0 \\ 0 & \frac{1}{2} \end{pmatrix} \begin{pmatrix} \langle b_{-1/2}| \\ \langle c_{-1/2}| \end{pmatrix} \\ &= (|\tilde{b}_{-1/2}\rangle, |\tilde{c}_{-1/2}\rangle) \begin{pmatrix} \frac{1}{2} - \frac{3}{2}u^2 & \frac{3}{2}uv \\ \frac{3}{2}uv & -1 + \frac{3}{2}u^2 \end{pmatrix} \begin{pmatrix} \langle \tilde{b}_{-1/2}| \\ \langle \tilde{c}_{-1/2}| \end{pmatrix}. \end{aligned} \quad (9.8)$$

As a next step, we introduce bosonic creation and annihilation operators $a_0^\dagger \equiv |a_{-1/2}\rangle\langle\tilde{b}_{-1/2}|$ etc., as indicated in Fig. 9.2(a). The subscripts of these operators refer to the change in the z -component of the total spin on the rung. Note that these operators do not obey the commutation relations of independent ladder operators, as we can create only one “particle” with either a_0^\dagger or a_1^\dagger or any other creation operator from the “vacuum” state $|\tilde{b}_{-1/2}\rangle$. Completeness and orthonormality of the basis (9.6) implies

$$|\tilde{b}_{-1/2}\rangle\langle\tilde{b}_{-1/2}| = (1 - b_1^\dagger b_1 - a_0^\dagger a_0 - a_1^\dagger a_1 - c_{-1}^\dagger c_{-1} - c_0^\dagger c_0 - c_1^\dagger c_1 - c_2^\dagger c_2). \quad (9.9)$$

With (9.7) and (9.9), the rung Hamiltonian (9.4) may be rewritten in terms of the bosonic operators:

$$\begin{aligned} \hat{H}^{\mathcal{A}} &= \left(\frac{1}{2} - \frac{3}{2}u^2\right) + \left(-\frac{1}{2} + \frac{3}{2}u^2\right) (a_0^\dagger a_0 + a_1^\dagger a_1) \\ &+ \frac{3}{2}uv (c_0^\dagger + c_0) + \frac{3}{2}(u^2 - v^2) c_0^\dagger c_0 - \frac{3}{2}v^2 b_1^\dagger b_1 + \frac{3}{2}u^2 (c_{-1}^\dagger c_{-1} + c_1^\dagger c_1 + c_2^\dagger c_2). \end{aligned} \quad (9.10)$$

On sublattice \mathcal{B} , we introduce a similar basis $M^{\mathcal{B}}$, with the only difference that the fiducial state $|\tilde{b}_{1/2}\rangle$ has $S^z = \frac{1}{2}$ instead of $s^z = -\frac{1}{2}$ for $|\tilde{b}_{-1/2}\rangle$ on sublattice \mathcal{A} :

$$\begin{aligned} M^{\mathcal{B}} &= \{|\mu\rangle^{\mathcal{B}}; \mu = 1, \dots, 8\} \\ &= \{|\tilde{b}_{1/2}\rangle, |b_{-1/2}\rangle, |a_{1/2}\rangle, |a_{-1/2}\rangle, |c_{3/2}\rangle, |\tilde{c}_{1/2}\rangle, |c_{-1/2}\rangle, |c_{-3/2}\rangle\}, \end{aligned}$$

with

$$\begin{pmatrix} |b_{1/2}\rangle \\ |c_{1/2}\rangle \end{pmatrix} = \begin{pmatrix} u & -v \\ v & u \end{pmatrix} \begin{pmatrix} |\tilde{b}_{1/2}\rangle \\ |\tilde{c}_{1/2}\rangle \end{pmatrix}. \quad (9.11)$$

We introduce a second set of bosonic creation and annihilation operators $A_0^\dagger \equiv |a_{1/2}\rangle\langle\tilde{b}_{1/2}|$ etc., as indicated in Fig. 9.2(b). The Hamiltonian $H^{\mathcal{B}}$ for a single rung belonging to sublattice \mathcal{B} is in analogy to (9.10) given by

$$\begin{aligned} \hat{H}^{\mathcal{B}} &= \left(\frac{1}{2} - \frac{3}{2}u^2\right) + \left(-\frac{1}{2} + \frac{3}{2}u^2\right) (A_{-1}^\dagger A_{-1} + A_0^\dagger A_0) \\ &+ \frac{3}{2}uv (C_0^\dagger + C_0) + \frac{3}{2}(u^2 - v^2) C_0^\dagger C_0 \\ &- \frac{3}{2}v^2 B_{-1}^\dagger B_{-1} + \frac{3}{2}u^2 (C_{-2}^\dagger C_{-2} + C_{-1}^\dagger C_{-1} + C_1^\dagger C_1). \end{aligned} \quad (9.12)$$

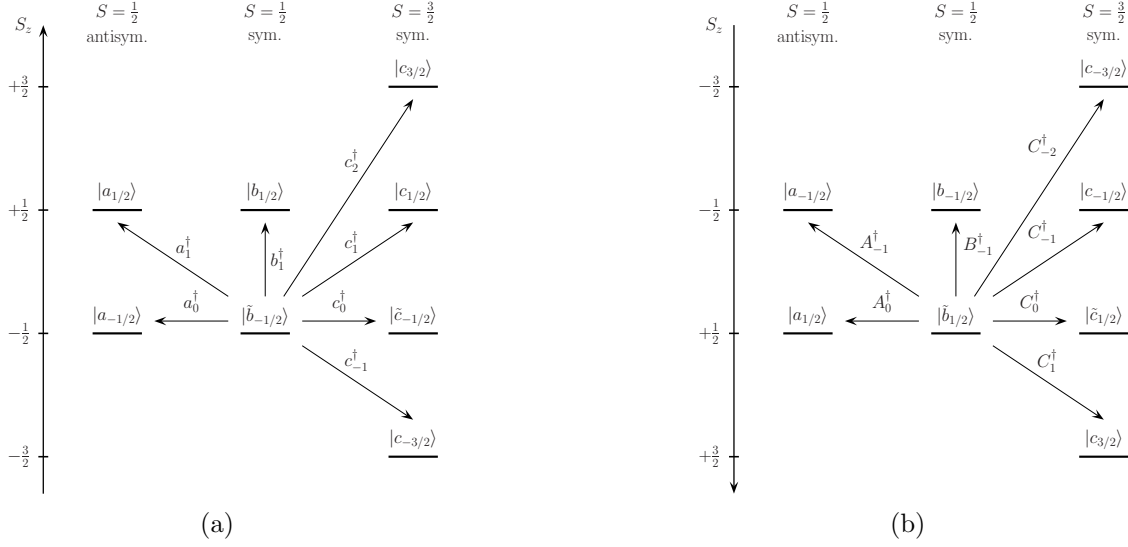


Figure 9.2: Description of the excitations out of the ground state on a particular rung via bosonic operators. (a) On sublattice \mathcal{A} the ground state is $|\tilde{b}_{-1/2}\rangle$ and we use small letters for the corresponding creation operators, whereas (b) On sublattice \mathcal{B} the ground state is $|\tilde{b}_{1/2}\rangle$ and capital letters denote the the corresponding operators.

For later purposes, we write the spin operators $\hat{s}_\alpha^\pm = \hat{s}_\alpha^x \pm i\hat{s}_\alpha^y$ and \hat{s}_α^z for the individual sites $\alpha = 1, 2, 3$ on rungs belonging to sublattice \mathcal{A} in terms of our bosonic creation and annihilation operators:

$$\begin{aligned}
 \hat{s}_\alpha^+ &= s_{\alpha,21}^+ b_1^\dagger + s_{\alpha,41}^+ a_1^\dagger + s_{\alpha,71}^+ c_1^\dagger + s_{\alpha,15}^+ c_{-1} \\
 &+ s_{\alpha,82}^+ c_2^\dagger b_1 + s_{\alpha,23}^+ b_1^\dagger a_0 + s_{\alpha,43}^+ a_1^\dagger a_0 \\
 &+ s_{\alpha,73}^+ c_1^\dagger a_0 + s_{\alpha,84}^+ c_2^\dagger a_1 + s_{\alpha,35}^+ a_0^\dagger c_{-1} \\
 &+ s_{\alpha,65}^+ c_0^\dagger c_{-1} + s_{\alpha,26}^+ b_1^\dagger c_0 + s_{\alpha,46}^+ a_1^\dagger c_0 \\
 &+ s_{\alpha,76}^+ c_1^\dagger c_0 + s_{\alpha,87}^+ c_2^\dagger c_1, \\
 \hat{s}_\alpha^- &= (\hat{s}_\alpha^+)^\dagger, \\
 \hat{s}_\alpha^z &= s_{\alpha,11}^z (1 - b_1^\dagger b_1 - a_0^\dagger a_0 - a_1^\dagger a_1 - c_0^\dagger c_0 - c_1^\dagger c_1 - c_{-1}^\dagger c_{-1} - c_2^\dagger c_2) \\
 &+ s_{\alpha,22}^z b_1^\dagger b_1 + s_{\alpha,55}^z c_{-1}^\dagger c_{-1} + s_{\alpha,66}^z c_0^\dagger c_0 \\
 &+ s_{\alpha,77}^z c_1^\dagger c_1 + s_{\alpha,88}^z c_2^\dagger c_2 \\
 &+ s_{\alpha,13}^z (a_0^\dagger + a_0) + s_{\alpha,16}^z (c_0^\dagger + c_0) \\
 &+ s_{\alpha,27}^z (b_1^\dagger c_1 + c_1^\dagger b_1) + s_{\alpha,24}^z (b_1^\dagger a_1 + a_1^\dagger b_1) \\
 &+ s_{\alpha,36}^z (a_0^\dagger c_0 + c_0^\dagger a_0) + s_{\alpha,47}^z (a_1^\dagger c_1 + c_1^\dagger a_1).
 \end{aligned} \tag{9.13}$$

The matrix elements

$$s_{\alpha,\mu\nu}^\tau = \langle \mu | \hat{s}_\alpha^\tau | \nu \rangle^{\mathcal{A}} \quad \text{with } \tau = +, -, z, \tag{9.14}$$

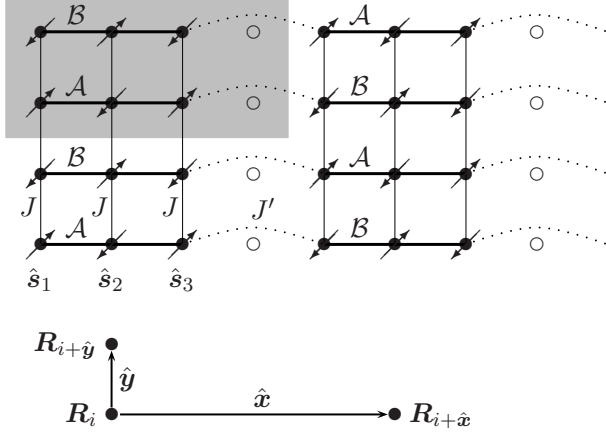


Figure 9.3: The microscopic model for site centered spin stripes, with intra-rung couplings set to unity, inter-rung-intra-ladder couplings J , and inter-ladder couplings J' . The real space unit cell contains two rungs and is indicated by the shaded area in gray.

and $|\mu\rangle^A$ as defined in (9.6) are written out explicitly in Appendix F. Similarly, the individual spin-operators \hat{S}_α^\pm and \hat{S}_z on rungs belonging to sublattice \mathcal{B} are given by:

$$\begin{aligned}
 \hat{S}_\alpha^- &= S_{\alpha,21}^- B_{-1}^\dagger + S_{\alpha,41}^- A_{-1}^\dagger + S_{\alpha,71}^- C_{-1}^\dagger + S_{\alpha,15}^- C_1 \\
 &+ S_{\alpha,82}^- C_{-2}^\dagger B_{-1} + S_{\alpha,23}^- B_{-1}^\dagger A_0 + S_{\alpha,43}^- A_{-1}^\dagger A_0 \\
 &+ S_{\alpha,73}^- C_{-1}^\dagger A_0 + S_{\alpha,84}^- C_{-2}^\dagger A_{-1} + S_{\alpha,35}^- A_0^\dagger C_1 \\
 &+ S_{\alpha,65}^- C_0^\dagger C_1 + S_{\alpha,26}^- B_{-1}^\dagger C_0 + S_{\alpha,46}^- A_{-1}^\dagger C_0 \\
 &+ S_{\alpha,76}^- C_{-1}^\dagger C_0 + S_{\alpha,87}^- C_{-2}^\dagger C_{-1}, \\
 \hat{S}_\alpha^+ &= (\hat{S}_\alpha^-)^\dagger, \\
 \hat{S}_\alpha^z &= S_{\alpha,11}^z (1 - B_{-1}^\dagger B_{-1} - A_0^\dagger A_0 - A_{-1}^\dagger A_{-1} - C_0^\dagger C_0 - C_{-1}^\dagger C_{-1} - C_1^\dagger C_1 - C_{-2}^\dagger C_{-2}) \\
 &+ S_{\alpha,22}^z B_{-1}^\dagger B_{-1} + S_{\alpha,55}^z C_1^\dagger C_1 + S_{\alpha,66}^z C_0^\dagger C_0 \\
 &+ S_{\alpha,77}^z C_{-1}^\dagger C_{-1} + S_{\alpha,88}^z C_{-2}^\dagger C_{-2} \\
 &+ S_{\alpha,13}^z (A_0^\dagger + A_0) + S_{\alpha,16}^z (C_0^\dagger + C_0) \\
 &+ S_{\alpha,27}^z (B_{-1}^\dagger C_{-1} + C_{-1}^\dagger B_{-1}) \\
 &+ S_{\alpha,24}^z (B_{-1}^\dagger A_{-1} + A_{-1}^\dagger B_{-1}) \\
 &+ S_{\alpha,36}^z (A_0^\dagger C_0 + C_0^\dagger A_0) \\
 &+ S_{\alpha,47}^z (A_{-1}^\dagger C_{-1} + C_{-1}^\dagger A_{-1}),
 \end{aligned} \tag{9.15}$$

with $S_{\alpha,\mu\nu}^\tau = \langle \mu | \hat{S}_\alpha^\tau | \nu \rangle^{\mathcal{B}}$ likewise given in Appendix F.

9.3 Coupling the Rungs

As a microscopic model for site centered spin stripes, we couple the three-site rungs into three-leg ladders, with the spins coupled antiferromagnetically with J along the ladders and with J' between neighboring ladders, as shown in Fig. 9.3. The sublattice indices assigned to each rung alternate in both directions, *i.e.*, under translation by either of

the primitive lattice vectors $\hat{\mathbf{x}} = (4a, 0)$ or $\hat{\mathbf{y}} = (0, a)$, where a is the lattice constant we herewith set to unity. The microscopic model is hence given by the Hamiltonian

$$\begin{aligned} \hat{H} &= \sum_{i \in \mathcal{A}} \left(\hat{H}_i^{\mathcal{A}} + J \sum_{\alpha=1}^3 \hat{\mathbf{s}}_{\alpha i} \hat{\mathbf{S}}_{\alpha i + \hat{\mathbf{y}}} + J' \hat{\mathbf{s}}_{3i} \hat{\mathbf{S}}_{1i + \hat{\mathbf{x}}} \right) \\ &+ \sum_{j \in \mathcal{B}} \left(\hat{H}_j^{\mathcal{B}} + J \sum_{\alpha=1}^3 \hat{\mathbf{S}}_{\alpha j} \hat{\mathbf{s}}_{\alpha j + \hat{\mathbf{y}}} + J' \hat{\mathbf{S}}_{3j} \hat{\mathbf{s}}_{1j + \hat{\mathbf{x}}} \right) \end{aligned} \quad (9.16)$$

When evaluating the spectrum of (9.16) below, we will set $J = 1$ (and thereby equal to the intra-rung couplings). The estimation of the inter-ladder coupling J' is presented in Section 10.2. We find $J' = 0.07$. For the moment, however, we keep the inter-rung and inter-ladder couplings J and J' as free parameter, as this makes it easier to trace the individual terms in the expansion below. The next step is to expand (9.16) in terms of our bosonic creation and annihilation operators, using (9.13), (9.15), and

$$\mathbf{s}_{\alpha} \mathbf{S}_{\beta} = \frac{1}{2} \left(\hat{s}_{\alpha}^{+} \hat{S}_{\beta}^{-} + \hat{s}_{\alpha}^{-} \hat{S}_{\beta}^{+} \right) + \hat{s}_{\alpha}^z \hat{S}_{\beta}^z. \quad (9.17)$$

We keep only terms up to second order in the operators. Since \hat{s}_{α}^z (and \hat{S}_{α}^z) contains a constant term with coefficient $s_{\alpha,11}^z$ as well as the linear terms

$$s_{\alpha,13}^z (a_0^{\dagger} + a_0) + s_{\alpha,16}^z (c_0^{\dagger} + c_0),$$

the expanded Hamiltonian will contain the linear term

$$\left(2J \sum_{\alpha=1}^3 S_{\alpha,11}^z s_{\alpha,16}^z + J' (S_{1,11}^z s_{3,16}^z + S_{3,11}^z s_{1,16}^z) \right) (c_0^{\dagger} + c_0) \quad (9.18)$$

in addition to the linear term

$$\frac{3}{2} uv (c_0^{\dagger} + c_0) \quad (9.19)$$

already contained in (9.10) for each rung i on sublattice \mathcal{A} . The terms proportional to $(a_0^{\dagger} + a_0)$ cancel since $s_{1,13}^z = -s_{3,13}^z$ and $s_{2,13}^z = 0$. This cancellation can also be inferred from symmetry considerations, as elaborated in the following section. We eliminate the linear terms (9.18) and (9.19) by adjusting the parameter ϕ , *i.e.*, by solving

$$\frac{3}{2} uv + 2J \sum_{\alpha=1}^3 S_{\alpha,11}^z s_{\alpha,16}^z + 2J' S_{1,11}^z s_{3,16}^z = 0 \quad (9.20)$$

with $J = 1$, $J' = 0.07$, $u = \cos \phi$, $v = \sin \phi$, and the matrix elements $s_{\alpha,\mu\nu}^z$ as given in Appendix F in terms of u and v . This yields

$$\sqrt{2} \frac{v}{u} \approx 0.5019 \quad \text{or} \quad \phi = 0.3410. \quad (9.21)$$

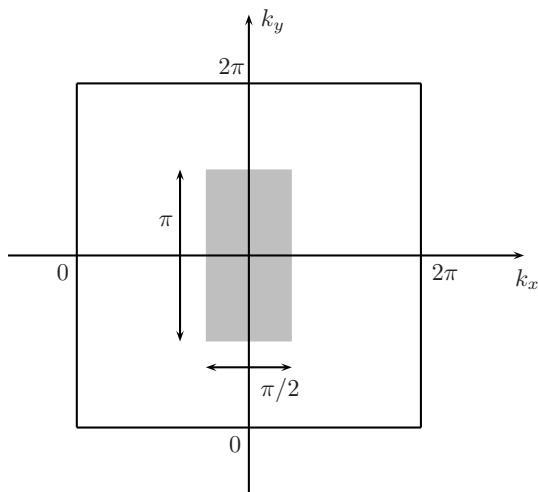


Figure 9.4: The reduced Brillouin zone corresponding to the real space unit cell indicated in Fig. 9.3 contains only 1/8th of the full Brillouin zone and is indicated by the shaded area.

On a formal level, the reason for rotating our basis states via (9.5), (9.7) and (9.11) to begin with was that this created the linear term (9.19) in H^A . Without this term, there would have been no way to eliminate (9.18), and the basis set would have been highly impractical for further analysis. On a physical level, the spontaneous breakdown of the SU(2) spin rotation symmetry leads us to expect that the fiducial state of the rungs is much closer to the classically ordered Néel state $|\uparrow\downarrow\uparrow\rangle$ than $|b_{-1/2}\rangle$. Not surprisingly, the spectrum evaluated below is gapless at some point in the Brillouin zone, as required by Goldstone's theorem for a state with a spontaneously broken continuous symmetry, if and only if ϕ assumes the value (9.21).

9.4 Expanding the Hamiltonian

To evaluate the spectrum of (9.16), we first define momentum space operators on sublattice \mathcal{A} according to

$$\begin{aligned} a_{0,\mathbf{k}} &= \sqrt{\frac{2}{N}} \sum_{i \in \mathcal{A}} e^{i\mathbf{k}\mathbf{R}_i} a_{0,i}, \\ a_{0,i} &= \sqrt{\frac{2}{N}} \sum_{\mathbf{k}} e^{-i\mathbf{k}\mathbf{R}_i} a_{0,\mathbf{k}}, \end{aligned} \quad (9.22)$$

where where N denotes the number of rungs and the sums over \mathbf{k} are taken over the reduced Brillouin zone indicated in gray in Fig. 9.4. Similarly, for the creation and annihilation operators on sublattice \mathcal{B} we introduce

$$\begin{aligned} A_{0,\mathbf{k}} &= \sqrt{\frac{2}{N}} \sum_{j \in \mathcal{B}} e^{-i\mathbf{k}\mathbf{R}_j} A_{0,j}, \\ A_{0,j} &= \sqrt{\frac{2}{N}} \sum_{\mathbf{k}} e^{i\mathbf{k}\mathbf{R}_j} A_{0,\mathbf{k}}, \end{aligned} \quad (9.23)$$

which differ from (9.22) only in that the sign of the phases is reversed. Since we are only interested in the one-particle spin wave spectrum, we neglect the effect of the Hilbert space restrictions for the real space creation and annihilation operators (*i.e.*, that we could create only one “particle” per rung) on the momentum space operators. As mentioned above, we only keep terms up to second order in the creation and annihilation operators in the Hamiltonian. When substituting the explicit expressions (9.13) and (9.15) into (9.16), we see immediately that many terms yield only higher orders, while others cancel. To begin with, since the spin flip operators only contain terms of first and second order in the creation and annihilation operators and are always multiplied with another spin-flip operator, we only need to keep terms of first order in the expressions for \hat{s}_α^+ and \hat{S}_α^- . The expansions of the $\hat{s}_\alpha^z \hat{S}_\beta^z$ terms are slightly more complicated, as \hat{s}_α^z and \hat{S}_β^z contain constant terms in addition to terms of first and second order in the creation and annihilation operators. We have adjusted the parameter ϕ such that the linear terms in the expansion cancel. Most of the quadratic terms result from multiplying the constant term $S_{\alpha,11}^z$ in the expansion of \hat{S}_α^z with the quadratic terms in \hat{s}_α^z and multiplying $s_{\alpha,11}^z$ with quadratic terms in \hat{S}_α^z . This yields seven diagonal terms (like $b_1^\dagger b_1$) and four off-diagonal terms (like $b_1^\dagger c_1 + c_1^\dagger b_1$) for each sublattice. Three of the off-diagonal terms, those linear in the antisymmetric operators a_1^\dagger or a_1 , vanish. This can be seen either from the explicit coefficients written out in Appendix F (*e.g.* $s_{1,24}^z = -s_{3,24}^z$ and $s_{2,24}^z = 0$ while $S_{1,11}^z = S_{3,11}^z$) or from a symmetry consideration. As the Hamiltonian is invariant under reflection symmetry interchanging the outer chains of each three-leg ladder (*i.e.*, sites 1 and 3 on each rung), there can only be terms containing an even number of the antisymmetric operators a_0^\dagger , a_0 , a_1^\dagger , a_1 , A_0^\dagger , A_0 , A_{-1}^\dagger , or A_{-1} in the expansion. In addition to this reflection symmetry, we have the SU(2) spin rotation symmetry of the Hamiltonian (9.16). The spin symmetry implies that the z -component of the total spin,

$$\hat{S}_{\text{tot}}^z = \sum_{i \in \mathcal{A}} \hat{s}_{\alpha i}^z + \sum_{j \in \mathcal{B}} \hat{S}_{\alpha j}^z, \quad (9.24)$$

must be conserved. This means that to second order in the creation and annihilation operators, only operators which change \hat{s}^z or \hat{S}^z by the same integer can appear in each term. For example, we can have a term $b_1^\dagger c_1$ or $b_1^\dagger c_{-1}^\dagger$, but not $b_1^\dagger c_0$. Both symmetries together imply that to second order, the Hamiltonian (9.16) decomposes into terms which contain only operators belonging to one particular group,

$$\hat{H} = \tilde{E}_0 + \hat{H}_{a0} + \hat{H}_{c0} + \hat{H}_{a1} + \hat{H}_{c2} + \hat{H}_{b1,c1,c-1}, \quad (9.25)$$

where \tilde{E}_0 is a contribution to the ground state energy, \hat{H}_{a0} contains only the operators a_0^\dagger , a_0 , A_0^\dagger , and A_0 , and so on. The low energy physics we are interested in is contained in $\hat{H}_{b1,c1,c-1}$, which we will analyze in detail below. As for the other terms, explicit expressions and expansions in terms of creation and annihilation operators are given in Appendix G. \hat{H}_{a0} and \hat{H}_{c0} describe almost dispersionless modes with energies of around 2.1 and 2.7 (in units of J_{exp} which we eventually set to $J_{\text{exp}} = 140$ meV). \hat{H}_{a1} describes a weakly dispersing mode of energy of about 2.0, with a bandwidth of about 0.2. \hat{H}_{c2} describes a completely dispersionless mode with energy 3.12. Cuts of the dispersions of

these modes are shown in Fig. G.1 in Appendix G. Since these modes occur at energies at which we consider our spin wave theory no longer reliable, we will not discuss them further. To evaluate the spectrum of $\hat{H}_{b1,c1,c-1}$, we write

$$\hat{H}_{b1,c1,c-1} = \sum_{\mathbf{k}} \left(\hat{\Psi}_{\mathbf{k}}^\dagger H_{\mathbf{k}} \hat{\Psi}_{\mathbf{k}} - \frac{1}{2} \text{tr}(H_{\mathbf{k}}) \right), \quad (9.26)$$

where

$$\begin{aligned} \hat{\Psi}_{\mathbf{k}}^\dagger &= (B_{-1,\mathbf{k}}^\dagger, b_{1,\mathbf{k}}, C_{-1,\mathbf{k}}^\dagger, c_{1,\mathbf{k}}, C_{1,-\mathbf{k}}, c_{-1,-\mathbf{k}}^\dagger), \\ \hat{\Psi}_{\mathbf{k}} &= (B_{-1,\mathbf{k}}, b_{1,\mathbf{k}}^\dagger, C_{-1,\mathbf{k}}, c_{1,\mathbf{k}}^\dagger, C_{1,-\mathbf{k}}^\dagger, c_{-1,-\mathbf{k}})^\text{T}. \end{aligned} \quad (9.27)$$

The 6×6 matrix $H_{\mathbf{k}}$ consists of the \mathbf{k} -independent diagonal terms

$$\begin{aligned} H_{\mathbf{k},11} = H_{\mathbf{k},22} &= -\frac{3}{2}v^2 + 2J \sum_{\alpha=1}^3 s_{\alpha,11}^z (S_{\alpha,22}^z - S_{\alpha,11}^z) + 2J' s_{3,11}^z (S_{1,22}^z - S_{1,11}^z), \\ H_{\mathbf{k},33} = H_{\mathbf{k},44} &= \frac{3}{2}u^2 + 2J \sum_{\alpha=1}^3 s_{\alpha,11}^z (S_{\alpha,77}^z - S_{\alpha,11}^z) + 2J' s_{3,11}^z (S_{1,77}^z - S_{1,11}^z), \\ H_{\mathbf{k},55} = H_{\mathbf{k},66} &= \frac{3}{2}u^2 + 2J \sum_{\alpha=1}^3 s_{\alpha,11}^z (S_{\alpha,55}^z - S_{\alpha,11}^z) + 2J' s_{3,11}^z (S_{1,55}^z - S_{1,11}^z). \end{aligned} \quad (9.28)$$

The off-diagonal terms are of the general form

$$H_{\mathbf{k},ij} = H_{\mathbf{k},ji} = H_{ij}^0 + H_{ij}^x \cos(4k_x) + H_{ij}^y \cos(k_y).$$

The \mathbf{k} -independent coefficients

$$H_{13}^0 = H_{24}^0 = 2J \sum_{\alpha=1}^3 s_{\alpha,11}^z S_{\alpha,27}^z + 2J' s_{3,11}^z S_{1,27}^z \quad (9.29)$$

result from the $\hat{s}_\alpha^z \hat{S}_\beta^z$ terms. Expansion of the $\hat{s}_\alpha^+ \hat{S}_\beta^-$ terms yields the coefficients

$$\begin{aligned} H_{12}^x &= J s_{3,21}^+ S_{1,21}^-, & H_{14}^x &= J s_{3,71}^+ S_{1,21}^-, \\ H_{16}^x &= J s_{3,15}^+ S_{1,21}^-, & H_{23}^x &= J s_{3,21}^- S_{1,71}^+, \\ H_{25}^x &= J s_{3,21}^- S_{1,51}^+, & H_{34}^x &= J s_{3,71}^+ S_{1,71}^-, \\ H_{36}^x &= J s_{3,15}^+ S_{1,71}^-, & H_{45}^x &= J s_{3,71}^- S_{1,51}^+, \\ H_{56}^x &= J s_{3,15}^+ S_{1,15}^-, \end{aligned} \quad (9.30)$$

and

$$\begin{aligned}
H_{12}^y &= J \sum_{\alpha=1}^3 s_{\alpha,21}^+ S_{\alpha,21}^-, & H_{14}^y &= J \sum_{\alpha=1}^3 s_{\alpha,71}^+ S_{\alpha,21}^-, \\
H_{16}^y &= J \sum_{\alpha=1}^3 s_{\alpha,15}^+ S_{\alpha,21}^-, & H_{23}^y &= J \sum_{\alpha=1}^3 s_{\alpha,12}^- S_{\alpha,17}^+, \\
H_{25}^y &= J \sum_{\alpha=1}^3 s_{\alpha,21}^+ S_{\alpha,15}^-, & H_{34}^y &= J \sum_{\alpha=1}^3 s_{\alpha,71}^+ S_{\alpha,71}^-, \\
H_{36}^y &= J \sum_{\alpha=1}^3 s_{\alpha,15}^+ S_{\alpha,71}^-, & H_{45}^y &= J \sum_{\alpha=1}^3 s_{\alpha,17}^- S_{\alpha,51}^+, \\
H_{56}^y &= J \sum_{\alpha=1}^3 s_{\alpha,15}^+ S_{\alpha,15}^-.
\end{aligned} \tag{9.31}$$

All other off-diagonal elements of $H_{\mathbf{k},ij}$ vanish.

9.5 Solution by Bogoliubov Transformation

The Hamiltonian (9.26) can be diagonalized with a $2n$ dimensional Bogoliubov transformation [87]. We begin with a brief review of the formalism. At each point in \mathbf{k} -space, we wish to write the Hamiltonian in terms of a diagonal matrix Ω ,

$$\hat{H} = \hat{\Psi}^\dagger H \hat{\Psi} = \hat{\Gamma}^\dagger \Omega \hat{\Gamma}, \tag{9.32}$$

with

$$\hat{\Psi} = M \hat{\Gamma}, \quad \Omega = M^\dagger H M. \tag{9.33}$$

The components of $\hat{\Gamma}$ satisfy the same commutation relations as the components of $\hat{\Psi}$:

$$[\hat{\Psi}_i, \hat{\Psi}_j^\dagger] = [\hat{\Gamma}_i, \hat{\Gamma}_j^\dagger] = T_{ij} \tag{9.34}$$

with

$$T = \text{diag}(1, -1, 1, -1, -1, 1). \tag{9.35}$$

This implies

$$T_{ij} = [\hat{\Psi}_i, \hat{\Psi}_j^\dagger] = \sum_{l,m} [M_{il} \hat{\Gamma}_l, \hat{\Gamma}_m^\dagger (M^\dagger)_{mj}] = \sum_{l,m} M_{il} [\hat{\Gamma}_l, \hat{\Gamma}_m^\dagger] M_{mj}^\dagger = \sum_{l,m} M_{il} T_{lm} M_{mj}^\dagger,$$

or

$$T = M T M^\dagger. \tag{9.36}$$

Multiplying (9.36) from the right by $H M$ yields with (9.33)

$$T H M = M T \Omega, \tag{9.37}$$

or in components

$$\sum_l (T H)_{il} M_{lj} = M_{ij} (T \Omega)_{jj}, \tag{9.38}$$

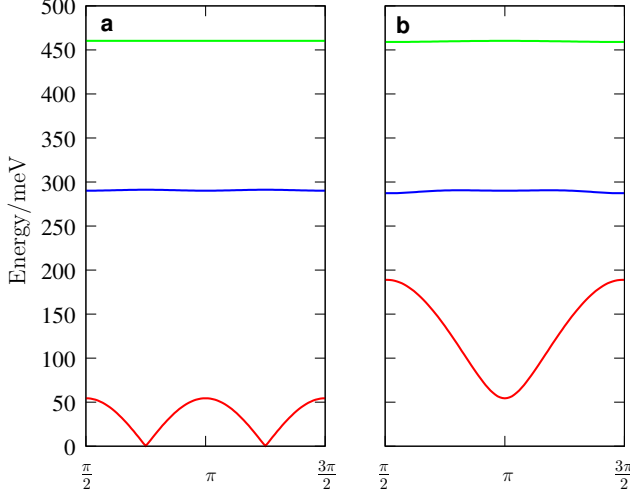


Figure 9.5: Modes described by $\hat{H}_{b1,c1,c-1}$ plotted as cuts (a) along (k_x, π) and (b) along (π, k_y) using $J_{\text{exp}} = 140$ meV.

i.e., the j -th column of M is given by an eigenvector of TH with eigenvalue $T_{jj}\Omega_{jj}$. This specifies M up to the normalization of the eigenvectors. To obtain the normalization, it is propitious to rewrite (9.36) as

$$T = M^\dagger T M. \quad (9.39)$$

(To obtain (9.39), multiply (9.36) by TM^{-1} from the left and by TM from the right and use $T^2 = 1$.) Each column j of M_{ij} must hence be normalized such that

$$T_{jj} = \sum_i T_{ii} |M_{ij}|^2. \quad (9.40)$$

Diagonalization of (9.26) using this formalism at each point in \mathbf{k} space with

$$\begin{aligned} \hat{\Gamma}_{\mathbf{k}}^\dagger &= (\gamma_{1,\mathbf{k}}^\dagger, \gamma_{2,\mathbf{k}}^\dagger, \gamma_{3,\mathbf{k}}^\dagger, \gamma_{4,\mathbf{k}}^\dagger, \gamma_{5,\mathbf{k}}^\dagger, \gamma_{6,\mathbf{k}}^\dagger), \\ \hat{\Gamma}_{\mathbf{k}} &= (\gamma_{1,\mathbf{k}}, \gamma_{2,\mathbf{k}}^\dagger, \gamma_{3,\mathbf{k}}, \gamma_{4,\mathbf{k}}^\dagger, \gamma_{5,\mathbf{k}}, \gamma_{6,\mathbf{k}})^\text{T}, \end{aligned} \quad (9.41)$$

yields

$$\hat{H}_{b1,c1,c-1} = \sum_{\mathbf{k},i} \left[\omega_{\mathbf{k},i} \gamma_{i,\mathbf{k}}^\dagger \gamma_{i,\mathbf{k}} + \frac{1}{2} (\omega_{\mathbf{k},i} - H_{\mathbf{k},ii}) \right]. \quad (9.42)$$

This Hamiltonian describes three two-fold degenerate modes $\omega_{\mathbf{k},i}$, which we have plotted assuming $J_{\text{exp.}} = 140$ meV as cuts along (k_x, π) and (π, k_y) in Fig. 9.5. The two-fold degeneracy of each mode corresponds to spin waves with $S_z = \pm 1$. Since we expect our spin wave theory to be reliable only for energies up to $J_{\text{exp.}}$, we will disregard the higher modes along with those analyzed in Appendix G. The lowest mode $\omega_{\mathbf{k},1} = \omega_{\mathbf{k},2} := \omega(\mathbf{k})$ is shown as a 3D plot for half of the reduced Brillouin zone in Fig. 10.3. The Hamiltonian (9.42) further contains a contribution

$$E_{b1,c1,c-1} = \sum_{\mathbf{k},i} \frac{1}{2} (\omega_{\mathbf{k},i} - H_{\mathbf{k},ii}) = -0.22116 N \quad (9.43)$$

to the ground state energy. (Here N denotes the number of rungs, which implies that the sum extends over $\frac{N}{2}$ values for \mathbf{k} .)

10 Results and Discussion

10.1 Introduction

In this chapter we shall present the main body of the second part, the presentation and the comparison with experiment of our results. To begin with we shall give a detailed description how we estimate the interladder coupling in case of the bond- as well as in case of the site-centered model in Section 10.2. We will find the resulting couplings give rise to magnetic order only in case of the site-centered model. In Section 10.3 we then present and compare our results to the experimental data by Tranquada *et. al.*. We shall begin with the dispersion of the magnetic excitations for the lowest lying eigenmode and will find perfect agreement with the experiment. Likewise we calculate the magnetic scattering intensity which we also compare and find best accordance to the experimental data. Finally, though not important for our studies and conclusions, we focus on the dependence of the saddle point energy $\omega(\pi, \pi)$ as a function of the inter-ladder coupling J' which we find to be given by a square-root dependence as long as J' is not comparable to the intra-ladder coupling J . We shall argue that this may be understood in terms of spinons in a confining potential.

10.2 Estimating the Interladder Coupling

To determine the effective coupling J' between the two- and three-leg ladders representing bond- or site-centred stripes, respectively, we have exactly diagonalised 16 site clusters of itinerant spin 1/2 antiferromagnets described by the t - J model[88, 89] with $J = 0.4t$, two holes, and periodic boundary conditions (PBCs), in which the stripes are localised through a staggered magnetic field B as shown in Figs. 10.2a and 10.2b. We then compare the ground state energies we obtain for clusters with the unfrustrated PBCs shown in Fig. 10.2 with the ground state energies we obtain for clusters with frustrated PBCs, in which the 16-site unit cells shown on the right are shifted by one lattice spacing to the top, such that sites 15 and 1, 16 and 2, etc. are nearest neighbours. We then consider spin-only Heisenberg models of two- and three-leg ladders (consisting of only the sites in the on-shaded areas in Figs. 10.2a and 10.2b) subject to the same staggered field B and couple them ferromagnetically or antiferromagnetically by J' , respectively, as indicated. We again compare the ground state energies for unfrustrated PBCs, where J' couples sites 6 and 1, 7 and 2, etc. for the two leg ladders shown in Fig. 10.2a, with frustrated PBCs, where J' couples sites 7 and 1, 8 and 2, etc. Finally, we determine J' such that the difference in the ground state energies between frustrated and unfrustrated PBCs in the t - J clusters matches this difference in the spin-only ladder

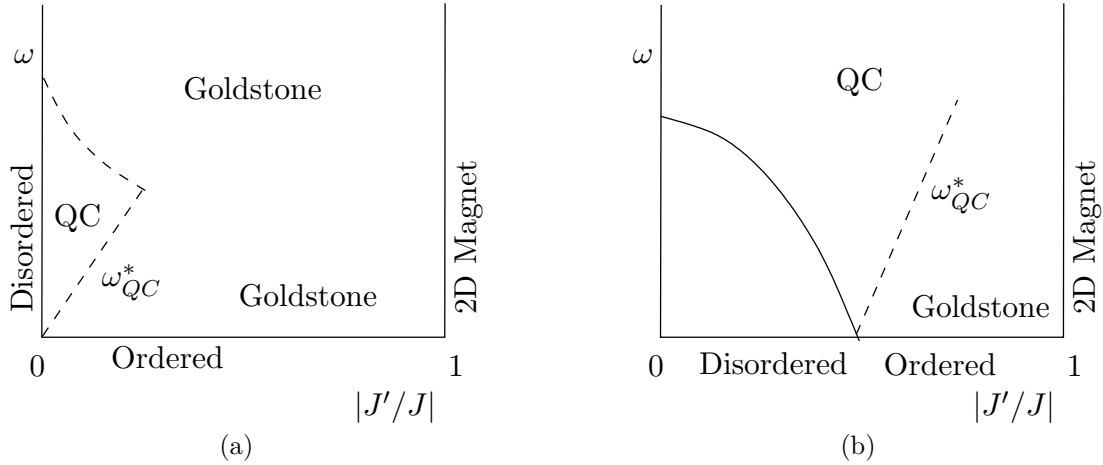


Figure 10.1: Generic phase diagram for coupled even- and odd-leg ladders. (a) In case of an odd leg ladder the quantum critical point is $J'_{\text{crit}} = 0$, where the system breaks into independent odd leg ladders. (b) In case of an even-leg ladder a quantum phase transition from the ordered into the disordered regime occurs at a finite value $|J'_{\text{crit}}|$ for ferromagnetic as well as for antiferromagnetic J' . For two leg ladders it holds $|J'_{\text{crit}}| \approx 0.25$

models. With $B = 0.225J$ and $B = 0.170J$ for the bond- or site-centred stripe models we obtain $J' = -0.051J$ and $J' = 0.071J$, respectively. The values for B are chosen such that the magnetic localisation energy $E_{\text{mag.}} = -B \sum_i (-1)^i S_i^z$ is equal for both types of stripes, and such that the mean value of the staggered magnetisation $\langle -S_1^z + S_5^z \rangle$ in the t - J cluster for the site-centred stripe matches the value we obtain in the fully consistent SWT of three-leg ladders described above.

10.3 Results

The significance of our results emerges in the context of a comparison of our spectrum with the experimental data obtained by Tranquada *et al.* [70] through inelastic neutron scattering on the stripe ordered compound $\text{La}_{1.875}\text{Ba}_{0.125}\text{CuO}_4$. The data points with corresponding error bars are shown as black or blue crosses in Figs. 10.4a and 10.4b, respectively. In Fig. 10.4b, which is directly reproduced from Tranquada *et al.* [70], the neutron data are superposed with the spectrum of the triplet excitation of an isotropic two-leg Heisenberg ladder, which models bond-centered stripes at accordingly high energies. To compare the data to a model of bond-centered stripes at all energies, Vojta *et al.* [76] and Uhrig *et al.* [77] have analyzed models of weakly, ferromagnetically coupled two-leg ladders, and find good agreement with the experimental data over the entire energy range from 0 to about 200meV. Vojta and Ulbricht [76] have analyzed the model through spin wave theory using a bond-operator formalism similar to the one we employ here, while Uhrig, Schmidt, and Grüninger [77] employ a method of continuous unitary

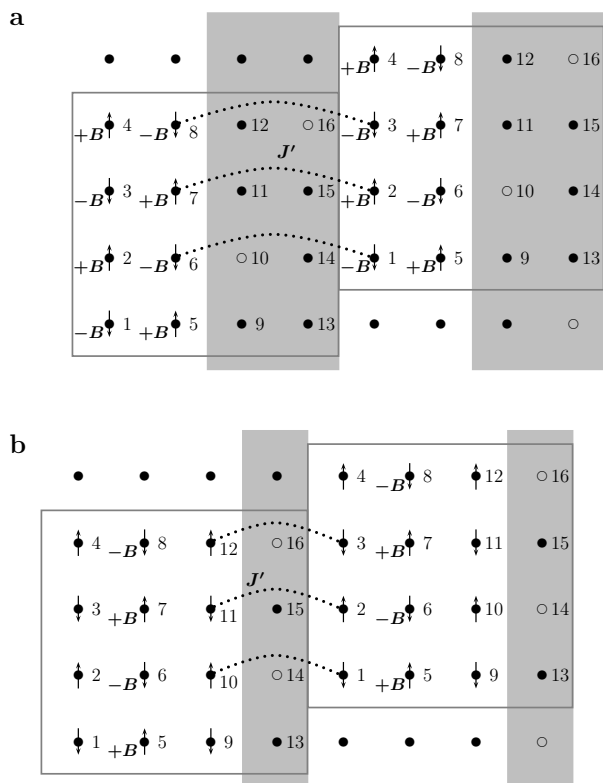


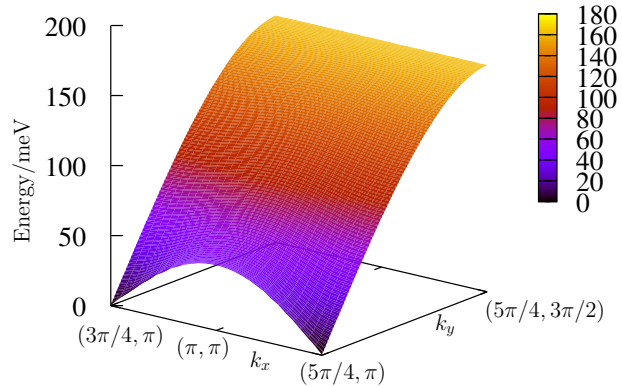
Figure 10.2: Finite size geometries with unfrustrated periodic boundaries for **a**, bond- and **b**, site-centred stripe models. The spin stripes are localised by a staggered magnetic field B as indicated by the signs.

transformations perfected by this group.

As for the calculations of both groups there appeared to be no systematic way to estimate the effective, ferromagnetic coupling J' induced by the likewise bond-centered charge stripe between two neighboring two-leg ladders, both groups resort to assuming values which yield good quantitative agreement of their spectra with the data. This, however, is only a minor inadequacy of their model, as the saddle-point energy is determined primarily by the triplet gap of the two-leg ladder and hence by the intra-ladder coupling J . The range of values they use depend on the approach and in the work of Uhrig *et al.* [77] also on the magnitude of the cyclic exchange term they impose, but all in all both studies provide as good a description as any one could get. Both groups independently conclude that the data are fully consistent with models of bond-centered stripes, and strengthen Tranquada's interpretation of the data as pointing towards bond-centered stripes.

To compare our results directly with the experimental data, we have superposed cuts of the lowest mode $\omega(\mathbf{k})$ along (k_x, π) and (π, k_y) with the experimental data in Fig. 10.4a. (The superposition of cuts of our spectrum in the x and y direction reflects the assumption that a superposition of domains with stripes along the two principal lattice directions has been observed in the experiment.) We believe it is fair to say that up to energies of about 175meV, the agreement is perfectly well and no worse than that of the bond-centered stripe models. Likewise, the constant energy slices of the neutron scattering intensities $\chi^{+-}(\mathbf{k}, \omega)$ obtained with the matrix elements calculated in Appendix

Figure 10.3: The dispersion $\omega(k_x, k_y)$ of the lowest eigenmode of $\hat{H}_{b1,c1,c-1}$ in half of the reduced Brillouin assuming $J_{\text{exp.}} = 120 \text{ meV}$



H shown in Fig. 10.5 agree as well as those obtained through analysis of two-leg ladder models (shown in Figs. 3 of Tranquada *et al.*[70], Vojta *et al.*[76], and Uhrig *et al.*[77]) with the experimentally measured constant-energy slices of the magnetic scattering in $\text{La}_{1.875}\text{Ba}_{0.125}\text{CuO}_4$ shown in Fig. 2 of Tranquada *et al.*[70]. The good agreement of our results with the experimental data up to energies even larger than $J = 140 \text{ meV}$ (where we would expect that the perturbative spin wave analysis becomes unreliable) is somewhat surprising. While any explanation in terms of bond-centered stripes, or coupled two-leg ladders, immediately gives a roughly adequate estimate for the saddle-point energy in terms of the triplet energy gap of the individual two-leg ladders, it is far from obvious that a model of coupled three-leg ladders, which are individually gapless, should give a saddle-point energy consistent with the data. In our model, the saddle-point energy depends significantly on the coupling J' between the ladders (cf. (10.1)). Fortunately, however, as already presented in Section 10.2 we are able to determine J' rather accurately through numerical comparison of a t - J model with a site centered spin and a site centered charge stripe to a model with three-leg Heisenberg ladders coupled by J' . This analysis does not only provide us with the value $J' \approx 0.07J$, but also shows that this value is rather robust in the sense that it does not significantly depend on the details of how we localize the stripe. To obtain a better understanding of the dependence of our final results on this coupling, we have obtained the spectrum for a number of different values of J' by solving (9.20) numerically for each value, and proceeding with the Bogoliubov transformation with the resulting values for $u(J')$ and $v(J')$. The results for the saddle-point energies $\omega(\pi, \pi)$ are shown in Fig. 10.6 (black dots). Fitting the data yields

$$\omega(\pi, \pi) \approx 1.47\sqrt{J'J} \quad (10.1)$$

to an excellent approximation up to values where J' becomes comparable to J .

The square root dependence of $\omega(\pi, \pi)$ on J' can be understood by considering a model of two three-leg ladders, which are weakly coupled by J' , as shown in Fig. 10.7a. The lowest energy excitations of the individual three-leg ladders are spin $\frac{1}{2}$ spinons, which are gapless. The coupling J' induces a linear confinement potential

$$V(y) = F|y| \quad (10.2)$$

between pairs of spinons, since the links coupling the chains effectively become decor-

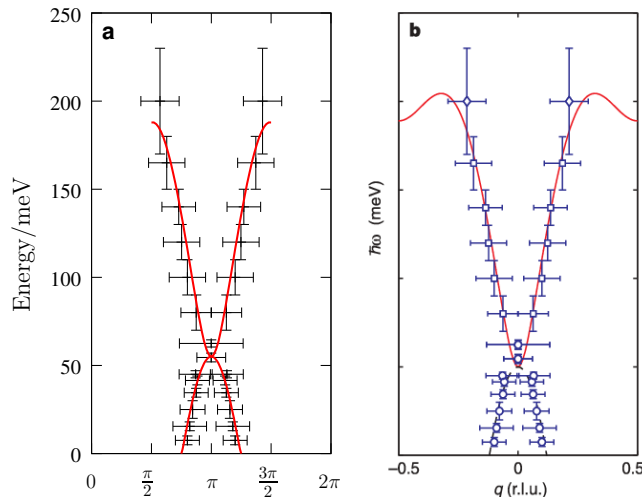


Figure 10.4: (a) Superpositions of cuts along (k_x, π) and (π, k_y) for the lowest mode $\omega(\mathbf{k})$ described by $\hat{H}_{b1,c1,c-1}$ (red) superimposed with the experimental data obtained by inelastic neutron scattering by Tranquada *et al.* [70] (black). (b) The neutron data as originally presented, with a triplon dispersion of a two-leg ladder superimposed (red line). (Figure (b) reproduced with permission.)

related in the region between them. The situation here is similar to a system of two coupled spin $\frac{1}{2}$ chains shown in Fig. 10.7b, where a weak coupling J_\perp between the chains is known to induce a linear confinement potential between pairs of spinons [90]. In the model of coupled chains, the force between the spinons is proportional to

$$F \approx \langle \mathbf{S}\mathbf{S} \rangle_\perp J_\perp \propto J_\perp^2/J. \quad (10.3)$$

For the model of two coupled three-leg ladders we consider here in the context of understanding the dependence (10.1) of our spin wave analysis, however, we assume that the spin correlation $\langle \mathbf{S}\mathbf{S} \rangle$ between the sites coupled by J' is to lowest order independent of J'/J . Therewith we account for the static correlations present due to the long range order we assume. For the confinement force in our auxiliary model of two coupled three-leg ladders we hence assume

$$F \propto J'. \quad (10.4)$$

The spinon confinement will then induce a gap Δ , which corresponds to the the ground state or zero-point energy of the linear potential oscillator for the relative motion of the spinons. The dispersion of the spinons is linear for both the individual spin chains and the individual three-leg ladders[91],

$$\varepsilon(k_y) \approx v|k_y|, \quad (10.5)$$

with $v \propto J$ as J is the only energy scale in these models. (In (10.5), we have shifted both spinon branches to the origin.) The ground state energy E_0 of a constant force

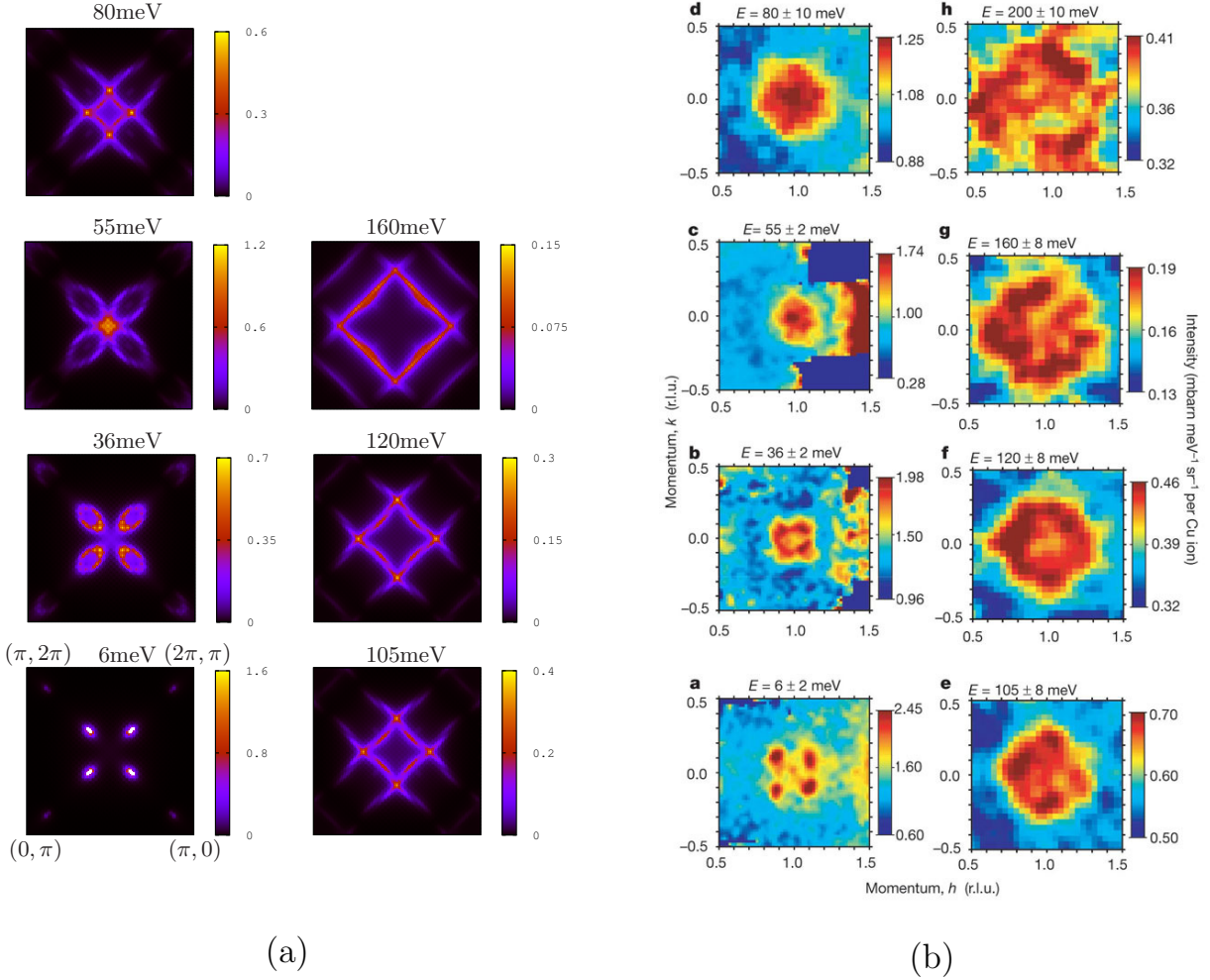


Figure 10.5: (a) Constant energy slices of the neutron scattering intensity $\chi^{+-}(\mathbf{k}, \omega)$ (see Appendix H below) for $J_{\text{exp}} = 140 \text{ meV}$ and $J' = 0.07 J_{\text{exp}}$ in the magnetic Brillouin zone. In the indicated energy range, only the lowest mode shown in Figs. 10.3 and 10.4a contributes. We have replaced the δ -functions in frequency by Lorentzians with half-width $\Delta = 0.05 J_{\text{exp}}$ and averaged over both stripe orientations (*i.e.*, horizontal and vertical). (b) For direct comparison we show the experimental data from Tranquada *et al.*[70].

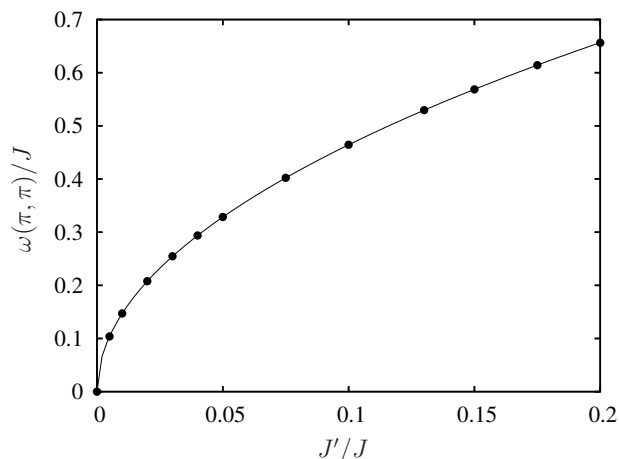


Figure 10.6: The saddle point energy $\omega(\pi, \pi)$ of the lowest magnetic mode $\omega(\mathbf{k})$ calculated for various values of J'/J (points). Fitting yields $\omega(\pi, \pi) \approx 1.47\sqrt{J'J}$ (solid line).

F oscillator of linearly dispersing particles with velocity v , however, is proportional to \sqrt{Fv} . (To see this, note that the spectrum must be invariant under the scaling (gauge) transformation $y \rightarrow \lambda y$, $k_y \rightarrow \lambda^{-1}k_y$, $F \rightarrow \lambda^{-1}F$, $v \rightarrow \lambda v$, which reflects its independence on the scale we use to measure lengths in our description. The spectrum can hence only depend on the invariant Fv , which has units of energy squared.) This implies $\Delta \propto J_{\perp}$ for the two weakly coupled chains and $\Delta \propto \sqrt{J'J}$ for the two weakly coupled three-leg ladders with the additional assumption of static correlations stemming from long range order.

To see why this gap Δ corresponds to the saddle point energy $\omega(\pi, \pi)$ in the spin wave analysis above, consider the transformation properties of our auxiliary model of the two weakly coupled three-leg ladders shown in Fig. 10.7a under the parity reflection $x \rightarrow -x$. The gapped spinon-spinon bound state is odd under this symmetry, which in the language of momenta k_x of the site centered stripe model corresponds to a shift of $\frac{\pi}{4}$. Since the ground state of the stripe model has order with $k_x = \pi \pm \frac{\pi}{4}$, the gapped excitation will correspond to $k_x = \pi$. Following this line of reasoning, we can hence understand the square root dependence (10.1) of $\omega(\pi, \pi)$ depicted in Fig. 10.6.

These considerations, however, are rather irrelevant to the ultimate goal of our studies, which is to deepen our understanding of and to broaden our perspective on the intriguing experimental results by Tranquada *et al.*[70].

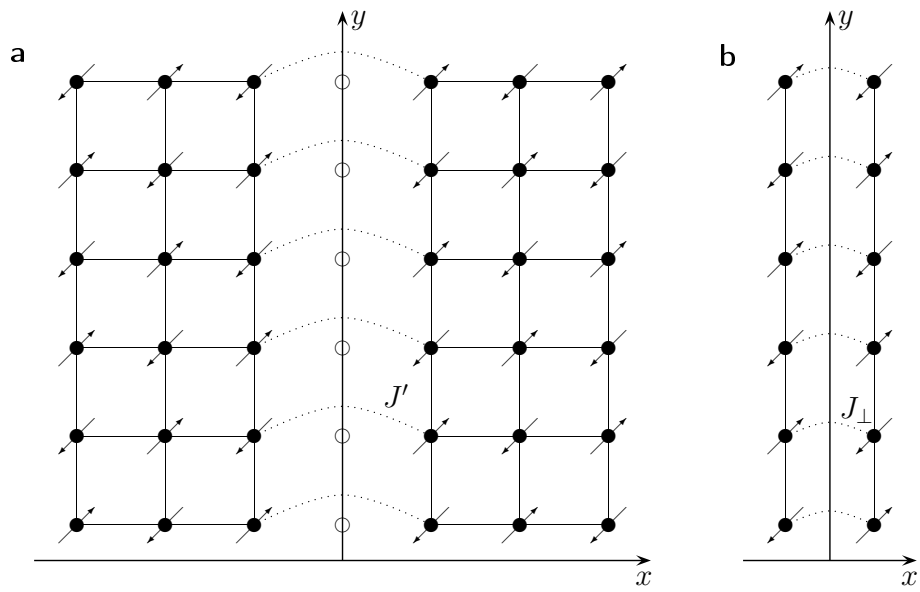


Figure 10.7: Auxiliary models of (a) two weakly coupled three-leg ladders and (b) two weakly coupled spin $\frac{1}{2}$ chains used in the discussion to understand the square root dependence of $\omega(\pi, \pi)$ on J' depicted in Fig. 10.6.

11 Conclusion

The second part of this thesis dealt with the high temperature superconducting compound $\text{La}_{2-x}\text{Ba}_x\text{CuO}_4$ at a doping level of $x = 1/8$. In a narrow region about this doping an anomalous suppression of superconductivity was observed and shown to be associated with charge and stripe order. Recent neutron scattering experiments focused on the quantum magnetic excitations in this striped phase. The results were subsequently interpreted in terms of a bond-centered stripe model, *i.e.* ferromagnetically coupled two leg spin ladders.

In this thesis we proposed a site-centered spin model which consists of antiferromagnetically coupled three-leg ladders. Whereas in both models the intra-ladder coupling is determined by experiment and amounts to about $J = 140\text{meV}$, the crucial point appears to be the inter-ladder coupling J' , which exhibits different behaviour in case of the bond-centered and site-centered spin model. Whereas in the site-centered stripe phase each small but finite coupling J' leads to magnetic order in case of the bond-centered stripe phase a sufficiently large value is required to induce magnetic order. For the bond-centered model studied previously by other groups this coupling was chosen in a way to either establish accordance with the experimental data or, in other words, to close the spin gap, which individual two-leg ladders obey.

The first question we have addressed in our work was whether the key assumption that J' is large enough to induce magnetic order in case of the bond-centered stripe model is valid. To this end we estimated the inter-ladder coupling as we compared small clusters with frustrated and unfrustrated boundary conditions. We find that only the site-centered model orders and hence conclude in favor of site- rather than bond-centered stripes. The main part of the work consists of the development of a fully consistent spin wave theory of bond-operators describing the magnetically ordered three-leg ladders. As far as physical observables are concerned, we focused on the magnetic excitations spectrum and the magnetic scattering intensity. In both cases we report excellent agreement with the experiment.

A The Pseudo-Fermion Representation

This appendix addresses the representation of a spin operator \mathbf{S} in terms of fermionic operators following Abrikosov [24, 25]. We restrict ourself to the case of $S = 1/2$. For each eigenstate of S_z $|\uparrow\rangle$ and $|\downarrow\rangle$ one introduces a pair of fermionic operators f_γ^\dagger and f_γ where $\gamma = \uparrow, \downarrow$. These operators obey the usual fermionic anti-commutation relations

$$\{f_\gamma, f_{\gamma'}^\dagger\} = \delta_{\gamma\gamma'}. \quad (\text{A.1})$$

The eigenstates of S_z are then obtained by acting with the creation operator f_γ^\dagger on the vacuum state $|0\rangle$: $|\gamma\rangle = f_\gamma^\dagger|0\rangle$.

The components of the spin operator \mathbf{S} is expressed as follows in the pseudo fermion representation

$$S_+ = f_\uparrow^\dagger f_\downarrow, \quad S_- = f_\downarrow^\dagger f_\uparrow, \quad S_z = \frac{1}{2} \left(f_\uparrow^\dagger f_\uparrow - f_\downarrow^\dagger f_\downarrow \right). \quad (\text{A.2})$$

Hence, S_x and S_y are given by

$$S_x = \frac{1}{2} (S_- + S_+) = \frac{1}{2} \left(f_\downarrow^\dagger f_\uparrow + f_\uparrow^\dagger f_\downarrow \right) \quad (\text{A.3})$$

$$S_y = \frac{i}{2} (S_- - S_+) = \frac{i}{2} \left(f_\downarrow^\dagger f_\uparrow - f_\uparrow^\dagger f_\downarrow \right). \quad (\text{A.4})$$

In a compact form the spin operator \mathbf{S} may thus be written as

$$\mathbf{S} = \frac{1}{2} \sum_{\gamma\gamma'} f_\gamma^\dagger \vec{\tau}_{\gamma\gamma'} f_{\gamma'} \quad (\text{A.5})$$

with τ being the vector build by the three Pauli matrices

$$\vec{\tau} = \left(\begin{pmatrix} 0 & 1 \\ 1 & 0 \end{pmatrix}, \begin{pmatrix} 0 & -i \\ i & 0 \end{pmatrix}, \begin{pmatrix} 1 & 0 \\ 0 & -1 \end{pmatrix} \right)^T. \quad (\text{A.6})$$

However, this representation has the disadvantage, that it provides four possibilities of occupancy $|0\rangle, |\uparrow\rangle, |\downarrow\rangle$ and $|\uparrow\downarrow\rangle$. Avoiding this displeasing circumstance is achieved by adding a chemical potential λ to the Hamiltonian, i.e. a term

$$H_\lambda = \lambda \sum_{\gamma} f_\gamma^\dagger f_\gamma \quad (\text{A.7})$$

and then take the limit $\lambda \rightarrow \infty$ as described in more detail in Section 3.4.

Finally we list expressions for spin sums which occur during the analysis of the FRG equations

$$\tau_{\sigma\sigma''}^i \tau_{\gamma\gamma''}^i \tau_{\sigma''\sigma'}^j \tau_{\gamma''\gamma'}^j = \tau_{\sigma\sigma'}^k \tau_{\gamma\gamma'}^k + 3\tau_{\sigma\sigma'}^0 \tau_{\gamma\gamma'}^0 \quad (\text{A.8})$$

$$\tau_{\sigma\sigma''}^i \tau_{\gamma''\gamma'}^i \tau_{\sigma''\sigma'}^j \tau_{\gamma\gamma''}^j = -\tau_{\sigma\sigma'}^k \tau_{\gamma\gamma'}^k + 3\tau_{\sigma\sigma'}^0 \tau_{\gamma\gamma'}^0. \quad (\text{A.9})$$

B Grassmann Algebra

Grassman fields occur naturally while setting up a functional integral representation for the partition function of a fermionic many particle system. This appendix deals with the basic features of Grassman fields and integrations in this regard. Let ψ_k and $\bar{\psi}_k$ Grassman fields and c_k, c_k^\dagger be the corresponding fermionic destruction and creation operators. The Grassmann fields obey the usual fermionic commutation relations

$$\{\psi_k, \psi_{k'}\} = \delta_{k,k'}. \quad (\text{B.1})$$

A fermion coherent state is defined via

$$c_k |\psi_k\rangle = \psi_k |\psi_k\rangle = |0\rangle - \psi_k |1\rangle. \quad (\text{B.2})$$

The basic Grassmann integrals are given by

$$\int d\psi_k 1 = 0 \quad (\text{B.3})$$

$$\int d\psi_k \psi_k = 1 \quad (\text{B.4})$$

$$\int d\bar{\psi}_k d\psi_k \bar{\psi}_k \psi_k = -1 \quad (\text{B.5})$$

$$\int d\bar{\psi}_k d\psi_k \psi_k \bar{\psi}_k = 1. \quad (\text{B.6})$$

Let $A_{kk'}$ be an arbitrary but invertible complex matrix. Then the following Gaussian identity is valid

$$\int \left(\prod_k d\bar{\psi}_k d\psi_k \right) e^{-\bar{\psi}_k A_{kk'} \psi_{k'}} e^{\bar{\psi}_k \eta_k + \bar{\eta}_k \psi_k} = \det(A) e^{\bar{\eta}_k A_{kk'}^{-1} \eta_{k'}}. \quad (\text{B.7})$$

The following identity for the integral of a product of a polynomial with a Gaussian directly corresponds to Wick's theorem

$$\frac{\int D[\bar{\psi}, \psi] \psi_{i_1} \cdots \psi_{i_n} \bar{\psi}_{j_1} \cdots \bar{\psi}_{j_n} e^{-(\bar{\psi}, A\psi)}}{\int D[\bar{\psi}, \psi] e^{-(\bar{\psi}, A\psi)}} = \sum_P (-1)^P A_{i_{P_n}, j_n}^{-1} \cdots A_{i_{P_1}, j_1}^{-1} \quad (\text{B.8})$$

where $(\bar{\psi}, A\psi) = \bar{\psi}_i A_{ij} \psi_j$. The proof of (B.8) may be obtained via the related formula

$$Z[\bar{\eta}, \eta] = \frac{\int D[\bar{\psi}, \psi] e^{-(\bar{\psi}, A\psi)} e^{(\bar{\eta}, \psi) + (\bar{\psi}, \eta)}}{\int D[\bar{\psi}, \psi] e^{-(\bar{\psi}, A\psi)}} = e^{(\bar{\eta}, A^{-1} \eta)} \quad (\text{B.9})$$

by differentiating the left hand side and the right hand side of (B.9) separately and then equating the two resulting expressions.

Finally we list the rule for a Grassmann delta function

$$\delta(\bar{\psi}_1 - \bar{\psi}_2) = \int d\psi e^{(\bar{\psi}_1 - \bar{\psi}_2)\psi}. \quad (\text{B.10})$$

C Derivation of the Functional Integral

This appendix gives a detailed derivation of the path integral representation of the Kondo dot model in nonequilibrium, following the path integral representation for the Keldysh contour in [26]. We start from the Kondo dot Hamiltonian equ. (3.7), which we write in the following form

$$\begin{aligned}
H &= \sum_{\alpha \sigma x} c_{\alpha \sigma x}^\dagger \left(-\frac{\partial_x^2}{2m} - \mu_\alpha \right) c_{\alpha \sigma x} - B \sum_{\sigma} \sigma f_{\sigma}^\dagger f_{\sigma} + \lambda \sum_{\sigma} f_{\sigma}^\dagger f_{\sigma} \\
&+ \frac{1}{4} \sum_{\alpha \alpha' \sigma \sigma' \gamma \gamma'} J_{\alpha, \alpha'} \vec{\tau}_{\sigma \sigma'} \vec{\tau}_{\gamma \gamma'} c_{\alpha \sigma 0}^\dagger c_{\alpha' \sigma' 0} f_{\gamma}^\dagger f_{\gamma'}.
\end{aligned} \tag{C.1}$$

For abbreviation we shall define

$$V_{\sigma \sigma' \gamma \gamma'} = \frac{1}{4} \vec{\tau}_{\sigma \sigma'} \vec{\tau}_{\gamma \gamma'} \tag{C.2}$$

At time $t = -\infty$ we take Hamiltonian to be

$$H = \sum_{\alpha \sigma x} c_{\alpha \sigma x}^\dagger \left(-\frac{\partial_x^2}{2m} - \mu_\alpha \right) c_{\alpha \sigma x} + \sum_{\sigma} (\lambda - B\sigma) f_{\sigma}^\dagger f_{\sigma} \tag{C.3}$$

which is composed of two noninteracting leads and an uncoupled local spin. To setup the functional integral we as usual coherent states for both the lead electron and the pseudo fermion operators

$$c_{\alpha \sigma x} |\psi\rangle = \psi_{\alpha \sigma x} |\psi\rangle \tag{C.4}$$

$$f_{\sigma} |\phi\rangle = \phi_{\sigma} |\phi\rangle. \tag{C.5}$$

The $\psi_{\alpha \sigma k}$ and ϕ_{σ} are Grassmann numbers (cf. App. B) and fulfill the closure relation

$$1 = \int \prod_{\alpha \sigma x} d\bar{\psi}_{\alpha \sigma x} d\psi_{\alpha \sigma x} e^{-\sum_{\alpha \sigma x} \bar{\psi}_{\alpha \sigma x} \psi_{\alpha \sigma x}} |\psi\rangle \langle \psi| \tag{C.6}$$

$$1 = \int \prod_{\sigma} d\bar{\phi}_{\sigma} d\phi_{\sigma} e^{-\sum_{\sigma} \bar{\phi}_{\sigma} \phi_{\sigma}} |\phi\rangle \langle \phi|. \tag{C.7}$$

The Lagrangian density in terms of the Grassmann fields reads

$$L(t) = \sum_{\alpha \sigma x} \bar{\psi}_{\alpha \sigma x} (i\partial_t + \frac{\partial_x^2}{2m} + \mu_\alpha) \psi_{\alpha \sigma x} + \sum_{\sigma} \bar{\phi}_{\sigma} (i\partial_t - \lambda + B\sigma) \phi_{\sigma} \tag{C.8}$$

$$- \sum_{\alpha \alpha' \sigma \sigma' \gamma \gamma'} J_{\alpha, \alpha'} V_{\sigma \sigma' \gamma \gamma'} \bar{\psi}_{\alpha \sigma 0} \bar{\phi}_{\gamma} \phi_{\gamma'} \psi_{\alpha \sigma 0}, \tag{C.9}$$

and the corresponding action S is obtained by integrating L over the Keldysh contour C_K

$$S[\bar{\psi}, \psi; \bar{\phi}, \phi] = \int_{C_K} L(\bar{\psi}, \psi; \bar{\phi}, \phi, t) dt \quad (\text{C.10})$$

Therewith the partition function is given by

$$Z = \int \left(\prod_{\alpha\sigma x t} d\bar{\psi}_{\alpha\sigma x}(t) d\psi_{\alpha\sigma x}(t) \right) \left(\prod_{\gamma t} d\bar{\phi}_{\gamma}(t) d\phi_{\gamma}(t) \right) e^{iS[\bar{\psi}, \psi; \bar{\phi}, \phi]}. \quad (\text{C.11})$$

As a next step we split the action S into a free, quadratic part S_0 and a quartic term S_1 which contains interactions

$$\begin{aligned} S_0 &= \int_{C_K} dt \left(\sum_{\alpha\sigma x} \bar{\psi}_{\alpha\sigma x}(t) (i\partial_t + \frac{\partial_x^2}{2m} + \mu_\alpha) \psi_{\alpha\sigma x}(t) + \sum_{\sigma} \bar{\phi}_{\sigma}(t) (i\partial_t - \lambda + B\sigma) \phi_{\sigma}(t) \right) \\ &= S_{0c} + S_{0f} \end{aligned} \quad (\text{C.12})$$

$$S_1 = - \int_{C_K} dt \left(\sum_{\alpha\alpha'\sigma\sigma'\gamma\gamma'} J_{\alpha,\alpha'} V_{\sigma\sigma'\gamma\gamma'} \bar{\psi}_{\alpha\sigma 0}(t) \bar{\phi}_{\gamma}(t) \phi_{\gamma'}(t) \psi_{\alpha'\sigma' 0}(t) \right) \quad (\text{C.13})$$

The free part has been divided into a term for the lead electrons S_{0c} and a term for the pseudo fermions S_{0f} . To avoid integration along the Keldysh contour we introduce the following vector fields

$$\bar{\psi}_{\alpha\sigma x}(t) \rightarrow (\bar{\psi}_{\alpha\sigma x}^+(t), \bar{\psi}_{\alpha\sigma x}^-(t)) \quad \psi_{\alpha\sigma x}(t) \rightarrow \begin{pmatrix} \psi_{\alpha\sigma x}^+(t) \\ \psi_{\alpha\sigma x}^-(t) \end{pmatrix} \quad (\text{C.14})$$

$$\bar{\phi}_{\gamma}(t) \rightarrow (\bar{\phi}_{\gamma}^+(t), \bar{\phi}_{\gamma}^-(t)) \quad \phi_{\gamma}(t) \rightarrow \begin{pmatrix} \phi_{\gamma}^+(t) \\ \phi_{\gamma}^-(t) \end{pmatrix}, \quad (\text{C.15})$$

where ψ^+, ϕ^+ resides on the upper and ψ^-, ϕ^- on the lower Keldysh contour, respectively (cf. Fig. 4.2). That followed we perform a Fourier transformation which yields for the electronic part S_{0c} :

$$\begin{aligned} S_{0c} &= \sum_{\alpha\sigma\omega k} \bar{\psi}_{\alpha\sigma k}^+(\omega) (\omega - \epsilon_k + \mu_\alpha) \psi_{\alpha\sigma k}^+(\omega) - \sum_{\alpha\sigma\omega k} \bar{\psi}_{\alpha\sigma k}^-(\omega) (\omega - \epsilon_k + \mu_\alpha) \psi_{\alpha\sigma k}^-(\omega) \\ &= \sum_{\alpha\sigma\omega k} \vec{\psi}_{\alpha\sigma k}(\omega) (\omega - \epsilon_k + \mu_\alpha) \tau_3 \vec{\psi}_{\alpha\sigma k}(\omega) \end{aligned} \quad (\text{C.16})$$

with the abbreviation

$$\sum_{\alpha\sigma\omega k} = \sum_{\alpha\sigma k} \int d\omega. \quad (\text{C.17})$$

Since the action is local in space we may integrate out the spatial electronic degrees of freedom. To this end we define the new fields

$$\bar{\psi}_{\alpha\sigma}^{\pm}(\omega) := \bar{\psi}_{\alpha\sigma x=0}^{\pm}(\omega) = \sum_k \bar{\psi}_{\alpha\sigma k}^{\pm}(\omega) \quad \psi_{\alpha\sigma}^{\pm}(\omega) := \psi_{\alpha\sigma x=0}^{\pm}(\omega) = \sum_k \psi_{\alpha\sigma k}^{\pm}(\omega) \quad (\text{C.18})$$

and drone fields

$$\bar{\xi}_{\alpha\sigma}^{\pm}(\omega) \quad \text{and} \quad \xi_{\alpha\sigma}^{\pm}(\omega). \quad (\text{C.19})$$

With the allows us to write down a Grassmann delta function (cf. equ. (B.10))

$$\int \left(\prod_{\alpha\sigma\omega} d\bar{\xi}_{\alpha\sigma}^{\pm}(\omega) d\xi_{\alpha\sigma}^{\pm}(\omega) \right) e^{i \sum_{\alpha\sigma\omega} (\bar{\xi}_{\alpha\sigma}(\omega)(\psi_{\alpha\sigma}(\omega) - \sum_k \psi_{\alpha\sigma k}(\omega)) + \xi_{\alpha\sigma}(\omega)(\bar{\psi}_{\alpha\sigma}(\omega) - \sum_k \bar{\psi}_{\alpha\sigma k}(\omega)))}$$

We now insert an integration over $\bar{\psi}_{\alpha\sigma}(\omega)$, $\psi_{\alpha\sigma}(\omega)$ and $\bar{\xi}_{\alpha\sigma}(\omega)$, $\xi_{\alpha\sigma}(\omega)$ and the Grassmann delta function as a unity to obtain with the aid of equ. (B.7) (first integrate over $\bar{\psi}_{\alpha\sigma k}(\omega)$, $\psi_{\alpha\sigma k}(\omega)$ and then over the drone fields $\bar{\xi}_{\alpha\sigma}(\omega)$, $\xi_{\alpha\sigma}(\omega)$) the following effective partition function

$$Z = \int \left(\prod_{\alpha\sigma\omega} d\bar{\psi}_{\alpha\sigma}^+(\omega) d\psi_{\alpha\sigma}^+(\omega) d\bar{\psi}_{\alpha\sigma}^-(\omega) d\psi_{\alpha\sigma}^-(\omega) \right) \left(\prod_{\gamma\omega} d\bar{\phi}_{\gamma}^+(\omega) d\phi_{\gamma}^+(\omega) d\bar{\phi}_{\gamma}^-(\omega) d\phi_{\gamma}^-(\omega) \right) e^{i(S_0+S_1)}.$$

The crucial point is to find the correct inverse matrix of

$$\begin{pmatrix} (\omega - \epsilon_k + \mu_{\alpha}) & 0 \\ 0 & -(\omega - \epsilon_k + \mu_{\alpha}) \end{pmatrix} \quad (\text{C.20})$$

To this end we have to remind ourself that the continuous functional formulation is an abbreviate notation, which represents a discrete version by means of discrete time steps. Finally the continuous version is recovered as for the number of time steps on the Keldysh contour $2N$ the limit $N \rightarrow \infty$ is taken [26, 46]. However, since one would face the displeasure of inverting a $2N \times 2N$ matrix in the discrete case, its easier to recall that Green function are traces of time-ordered (with respect to the Schwinger-contour) products of field operators, i.e. equ. (4.34) or (4.35), respectively. Finally we quote the result for the interacting part S_1 after Fourier transforming

$$\begin{aligned} S_1 &= - \int_{-\infty}^{\infty} dt \left(\sum_{\alpha\alpha'\sigma\sigma'\gamma\gamma'} J_{\alpha,\alpha'} V_{\sigma\sigma'\gamma\gamma'} \bar{\psi}_{\alpha\sigma}^+(t) \bar{\phi}_{\gamma}^+(t) \phi_{\gamma'}^+(t) \psi_{\alpha'\sigma'}^+(t) \right) \\ &+ \int_{-\infty}^{\infty} dt \left(\sum_{\alpha\alpha'\sigma\sigma'\gamma\gamma'} J_{\alpha,\alpha'} V_{\sigma\sigma'\gamma\gamma'} \bar{\psi}_{\alpha\sigma}^-(t) \bar{\phi}_{\gamma}^-(t) \phi_{\gamma'}^-(t) \psi_{\alpha'\sigma'}^-(t) \right) \\ &= - \frac{1}{2\pi} \int_{-\infty}^{\infty} d\omega_c d\omega'_c d\omega_f d\omega'_f \delta(\omega_c + \omega_f - \omega'_f - \omega'_c) \times \\ &\quad \times \sum_{\alpha\alpha'\sigma\sigma'\gamma\gamma'} J_{\alpha,\alpha'} V_{\sigma\sigma'\gamma\gamma'} \bar{\psi}_{\alpha\sigma}^+(\omega_c) \bar{\phi}_{\gamma}^+(\omega_f) \phi_{\gamma'}^+(\omega'_f) \psi_{\alpha'\sigma'}^+(\omega'_c) \\ &+ \frac{1}{2\pi} \int_{-\infty}^{\infty} d\omega_c d\omega'_c d\omega_f d\omega'_f \delta(\omega_c + \omega_f - \omega'_f - \omega'_c) \times \\ &\quad \times \sum_{\alpha\alpha'\sigma\sigma'\gamma\gamma'} J_{\alpha,\alpha'} V_{\sigma\sigma'\gamma\gamma'} \bar{\psi}_{\alpha\sigma}^-(\omega_c) \bar{\phi}_{\gamma}^-(\omega_f) \phi_{\gamma'}^-(\omega'_f) \psi_{\alpha'\sigma'}^-(\omega'_c) \end{aligned} \quad (\text{C.21})$$

D Details on the Nonequilibrium FRG for the Kondo Model

In this appendix provides the technical details and steps of the derivation of the fRG flow equations for the Kondo dot model. In order to perform a Legendre transformation to obtain the generating functional for the 1PI vertex function we again introduce the fields

$$\bar{\chi} = \frac{\partial \mathcal{W}}{\partial \eta} \quad \chi = -\frac{\partial \mathcal{W}}{\partial \bar{\eta}} \quad (\text{D.1})$$

$$\bar{\theta} = \frac{\partial \mathcal{W}}{\partial \xi} \quad \theta = -\frac{\partial \mathcal{W}}{\partial \bar{\xi}}, \quad (\text{D.2})$$

or after inverting

$$\frac{\partial \Gamma}{\partial \bar{\chi}} = -\eta + G_0^{-1} \chi \quad \frac{\partial \Gamma}{\partial \chi} = \bar{\eta} - \bar{\chi} G_0^{-1} \quad (\text{D.3})$$

$$\frac{\partial \Gamma}{\partial \bar{\theta}} = -\xi + F_0^{-1} \theta \quad \frac{\partial \Gamma}{\partial \theta} = \bar{\xi} - \bar{\theta} F_0^{-1}. \quad (\text{D.4})$$

By introducing the cutoff dependent bare lead electron propagator

$$G_0^\Lambda(\omega) = G_0(\omega) \Theta(|\omega| - \Lambda) \quad (\text{D.5})$$

the quantities \mathcal{W}^Λ and Γ^Λ acquire a Λ dependence. To begin with we take the derivate of $e^{\mathcal{W}^\Lambda} = \mathcal{G}^\Lambda$ with respect to Λ and obtain after some straightforward algebra

$$\frac{d\mathcal{W}^\Lambda}{d\Lambda} = -\text{Tr} \left(\frac{d(G_0^\Lambda)^{-1}}{d\Lambda} G_0^\Lambda \right) + i \text{Tr} \left(\frac{d(G_0^\Lambda)^{-1}}{d\Lambda} \frac{\partial^2 \mathcal{W}^\Lambda}{\partial \bar{\eta} \partial \eta} \right) + i \left(\frac{\partial \mathcal{W}^\Lambda}{\partial \eta}, \frac{d(G_0^\Lambda)^{-1}}{d\Lambda} \frac{\partial \mathcal{W}^\Lambda}{\partial \bar{\eta}} \right) \quad (\text{D.6})$$

From there the flow equation for the generating functional

Γ^Λ is obtained as

$$\frac{d\Gamma^\Lambda}{d\Lambda} = \text{Tr} \left(\frac{d(G_0^\Lambda)^{-1}}{d\Lambda} G_0^\Lambda \right) - i \text{Tr} \left(\frac{d(G_0^\Lambda)^{-1}}{d\Lambda} \frac{\partial^2 \mathcal{W}^\Lambda}{\partial \bar{\eta} \partial \eta} \right). \quad (\text{D.7})$$

The derivative $\frac{\partial^2 \mathcal{W}^\Lambda}{\partial \bar{\eta} \eta}$ can now again be expressed in terms of Γ^Λ using textbook relations [46]. If we denote

$$\begin{aligned} \tilde{\Gamma}^\Lambda[\bar{\chi}, \chi, \bar{\theta}, \theta] &= \Gamma[\bar{\chi}, \chi, \bar{\theta}, \theta] - i(\bar{\chi}, G_0^{-1} \chi) - i(\bar{\theta}, F_0^{-1} \theta) \\ &= -\mathcal{W}[\bar{\eta}, \eta, \bar{\xi}, \xi] - (\bar{\eta}, \chi) - (\bar{\chi}, \eta) - (\bar{\xi}, \theta) - (\bar{\theta}, \xi), \end{aligned} \quad (\text{D.8})$$

this relation becomes the following statement

$$\begin{pmatrix} W_{\bar{\eta}\eta} & -W_{\eta\eta} & W_{\bar{\xi}\eta} & -W_{\xi\eta} \\ -W_{\bar{\eta}\bar{\eta}} & W_{\eta\bar{\eta}} & -W_{\bar{\xi}\bar{\eta}} & W_{\xi\bar{\eta}} \\ W_{\bar{\eta}\xi} & -W_{\eta\xi} & W_{\bar{\xi}\xi} & -W_{\xi\xi} \\ -W_{\bar{\eta}\bar{\xi}} & W_{\eta\bar{\xi}} & -W_{\bar{\xi}\bar{\xi}} & W_{\xi\bar{\xi}} \end{pmatrix} \begin{pmatrix} \tilde{\Gamma}_{\bar{\chi}\chi} & \tilde{\Gamma}_{\chi\chi} & \tilde{\Gamma}_{\bar{\theta}\chi} & \tilde{\Gamma}_{\theta\chi} \\ \tilde{\Gamma}_{\bar{\chi}\bar{\chi}} & \tilde{\Gamma}_{\chi\bar{\chi}} & \tilde{\Gamma}_{\bar{\theta}\bar{\chi}} & \tilde{\Gamma}_{\theta\bar{\chi}} \\ \tilde{\Gamma}_{\bar{\chi}\theta} & \tilde{\Gamma}_{\chi\theta} & \tilde{\Gamma}_{\bar{\theta}\theta} & \tilde{\Gamma}_{\theta\theta} \\ \tilde{\Gamma}_{\bar{\chi}\bar{\theta}} & \tilde{\Gamma}_{\chi\bar{\theta}} & \tilde{\Gamma}_{\bar{\theta}\bar{\theta}} & \tilde{\Gamma}_{\theta\bar{\theta}} \end{pmatrix} = \mathbf{1}. \quad (\text{D.9})$$

Since the off diagonals of $\tilde{\Gamma}$ coincide with that of Γ one is let to

$$\frac{\partial^2 \mathcal{W}^\Lambda}{\partial \bar{\eta} \eta} = \begin{pmatrix} \tilde{\Gamma}_{\bar{\chi}\chi} & \Gamma_{\chi\chi} & \Gamma_{\bar{\theta}\chi} & \Gamma_{\theta\chi} \\ \Gamma_{\bar{\chi}\bar{\chi}} & \tilde{\Gamma}_{\chi\bar{\chi}} & \Gamma_{\bar{\theta}\bar{\chi}} & \Gamma_{\theta\bar{\chi}} \\ \Gamma_{\bar{\chi}\theta} & \Gamma_{\chi\theta} & \tilde{\Gamma}_{\bar{\theta}\theta} & \Gamma_{\theta\theta} \\ \Gamma_{\bar{\chi}\bar{\theta}} & \Gamma_{\chi\bar{\theta}} & \Gamma_{\bar{\theta}\bar{\theta}} & \tilde{\Gamma}_{\theta\bar{\theta}} \end{pmatrix}_{1,1}^{-1} \equiv (\Gamma_{\partial^2}^\Lambda)^{-1}_{1,1}. \quad (\text{D.10})$$

With the aid of the well known Dyson equations for the lead electrons and the pseudo fermions

$$(G^\Lambda)^{-1} = (G_0^\Lambda)^{-1} + \gamma_{1,\text{le}}^\Lambda \quad (\text{D.11})$$

$$(F^\Lambda)^{-1} = (F_0^\Lambda)^{-1} + \gamma_{1,\text{pf}}^\Lambda, \quad (\text{D.12})$$

where $\gamma_{1,\text{le}} = -\Sigma_{\text{le}}$ and $\gamma_{1,\text{pf}} = -\Sigma_{\text{pf}}$ denote the proper self energy parts of the lead electrons and the pseudofermions, respectively, equ. D.10 may be rewritten as

$$\begin{aligned}
 (\Gamma_{\partial^2}^\Lambda)^{-1} &= \begin{bmatrix} i(G^\Lambda)^{-1} & 0 & 0 & 0 \\ 0 & -i(G^\Lambda)^{-1} & 0 & 0 \\ 0 & 0 & i(F^\Lambda)^{-1} & 0 \\ 0 & 0 & 0 & -i(F^\Lambda)^{-1} \end{bmatrix} \\
 &+ \begin{bmatrix} \Gamma_{\bar{x}x} - i\gamma_{1,\text{le}}^\Lambda & \Gamma_{xx} & \Gamma_{\bar{\theta}x} & \Gamma_{\theta x} \\ \Gamma_{\bar{x}\bar{x}} & \Gamma_{x\bar{x}} + i\gamma_{1,\text{le}}^\Lambda & \Gamma_{\bar{\theta}\bar{x}} & \Gamma_{\theta\bar{x}} \\ \Gamma_{\bar{x}\theta} & \Gamma_{x\theta} & \Gamma_{\bar{\theta}\theta} - i\gamma_{1,\text{pf}}^\Lambda & \Gamma_{\theta\theta} \\ \Gamma_{\bar{x}\bar{\theta}} & \Gamma_{x\bar{\theta}} & \Gamma_{\bar{\theta}\bar{\theta}} & \Gamma_{\theta\bar{\theta}} + i\gamma_{1,\text{pf}}^\Lambda \end{bmatrix}^{-1} \\
 &= \begin{bmatrix} i(G^\Lambda)^{-1} & 0 & 0 & 0 \\ 0 & -i(G^\Lambda)^{-1} & 0 & 0 \\ 0 & 0 & i(F^\Lambda)^{-1} & 0 \\ 0 & 0 & 0 & -i(F^\Lambda)^{-1} \end{bmatrix} \left\{ 1 - \begin{bmatrix} -iG^\Lambda & 0 & 0 & 0 \\ 0 & iG^\Lambda & 0 & 0 \\ 0 & 0 & -iF^\Lambda & 0 \\ 0 & 0 & 0 & iF^\Lambda \end{bmatrix} \times \right. \\
 &\times \left. \begin{bmatrix} \Gamma_{\bar{x}x} - i\gamma_{1,\text{le}}^\Lambda & \Gamma_{xx} & \Gamma_{\bar{\theta}x} & \Gamma_{\theta x} \\ \Gamma_{\bar{x}\bar{x}} & \Gamma_{x\bar{x}} + i\gamma_{1,\text{le}}^\Lambda & \Gamma_{\bar{\theta}\bar{x}} & \Gamma_{\theta\bar{x}} \\ \Gamma_{\bar{x}\theta} & \Gamma_{x\theta} & \Gamma_{\bar{\theta}\theta} - i\gamma_{1,\text{pf}}^\Lambda & \Gamma_{\theta\theta} \\ \Gamma_{\bar{x}\bar{\theta}} & \Gamma_{x\bar{\theta}} & \Gamma_{\bar{\theta}\bar{\theta}} & \Gamma_{\theta\bar{\theta}} + i\gamma_{1,\text{pf}}^\Lambda \end{bmatrix} \right\}^{-1} \quad (\text{D.13}) \\
 &= \sum_{n=0}^{\infty} \left[\begin{bmatrix} -iG^\Lambda & 0 & 0 & 0 \\ 0 & iG^\Lambda & 0 & 0 \\ 0 & 0 & -iF^\Lambda & 0 \\ 0 & 0 & 0 & iF^\Lambda \end{bmatrix} \begin{bmatrix} \Gamma_{\bar{x}x} - i\gamma_{1,\text{le}}^\Lambda & \Gamma_{xx} & \Gamma_{\bar{\theta}x} & \Gamma_{\theta x} \\ \Gamma_{\bar{x}\bar{x}} & \Gamma_{x\bar{x}} + i\gamma_{1,\text{le}}^\Lambda & \Gamma_{\bar{\theta}\bar{x}} & \Gamma_{\theta\bar{x}} \\ \Gamma_{\bar{x}\theta} & \Gamma_{x\theta} & \Gamma_{\bar{\theta}\theta} - i\gamma_{1,\text{pf}}^\Lambda & \Gamma_{\theta\theta} \\ \Gamma_{\bar{x}\bar{\theta}} & \Gamma_{x\bar{\theta}} & \Gamma_{\bar{\theta}\bar{\theta}} & \Gamma_{\theta\bar{\theta}} + i\gamma_{1,\text{pf}}^\Lambda \end{bmatrix} \right]^n \times \\
 &\times \begin{bmatrix} iG^\Lambda & 0 & 0 & 0 \\ 0 & -iG^\Lambda & 0 & 0 \\ 0 & 0 & iF^\Lambda & 0 \\ 0 & 0 & 0 & -iF^\Lambda \end{bmatrix}.
 \end{aligned}$$

Therewith the flow for Γ^Λ can be rewritten as

$$\frac{d\Gamma^\Lambda}{d\Lambda} = \text{Tr} \left(\frac{d(G_0^\Lambda)^{-1}}{d\Lambda} G_0^\Lambda \right) - \text{Tr} \left(G^\Lambda \frac{d(G_0^\Lambda)^{-1}}{d\Lambda} \mathcal{R}_{1,1} \right) \quad (\text{D.14})$$

where $\mathcal{R}_{1,1}$ denotes the upper left corner of the matrix

$$\mathcal{R} = \sum_{n=0}^{\infty} \left[\begin{bmatrix} -iG^\Lambda & 0 & 0 & 0 \\ 0 & iG^\Lambda & 0 & 0 \\ 0 & 0 & -iF^\Lambda & 0 \\ 0 & 0 & 0 & iF^\Lambda \end{bmatrix} \begin{bmatrix} \Gamma_{\bar{x}x} - i\gamma_{1,\text{le}}^\Lambda & \Gamma_{xx} & \Gamma_{\bar{\theta}x} & \Gamma_{\theta x} \\ \Gamma_{\bar{x}\bar{x}} & \Gamma_{x\bar{x}} + i\gamma_{1,\text{le}}^\Lambda & \Gamma_{\bar{\theta}\bar{x}} & \Gamma_{\theta\bar{x}} \\ \Gamma_{\bar{x}\theta} & \Gamma_{x\theta} & \Gamma_{\bar{\theta}\theta} - i\gamma_{1,\text{pf}}^\Lambda & \Gamma_{\theta\theta} \\ \Gamma_{\bar{x}\bar{\theta}} & \Gamma_{x\bar{\theta}} & \Gamma_{\bar{\theta}\bar{\theta}} & \Gamma_{\theta\bar{\theta}} + i\gamma_{1,\text{pf}}^\Lambda \end{bmatrix} \right]^n \quad (\text{D.15})$$

E Useful Relations and Formulas

This Appendix contains a collection of helpful relations for the Bose and the Fermi functions and integrals in this regard. To begin with first recall the Fermi and Bose functions

$$n_F(x) = \frac{1}{e^{\beta x} + 1}, \quad n_B(x) = \frac{1}{e^{\beta x} - 1}. \quad (\text{E.1})$$

where $\beta = 1/T0$. For $a, b \in \mathbb{R}$ it holds

$$\begin{aligned} \int_{-\infty}^{\infty} n_F(x+a) (1 - n_F(x+b)) dx &= (a-b) \frac{1}{e^{\beta(a-b)} - 1} \\ &= (a-b) n_B(a-b). \end{aligned} \quad (\text{E.2})$$

If $a - b \equiv \Delta < 0$ this may be written as $|\Delta| (1 + n_B(|\Delta|))$.

For $a - b = 0$ equ. (E.2) reduces to

$$\int_{-\infty}^{\infty} n_F(x) (1 - n_F(x)) dx = \int_{-\infty}^{\infty} n_F(x) n_F(-x) dx = \frac{1}{\beta} \quad (\text{E.3})$$

Further useful relation for the Fermi and Bose functions.

$$1 - 2n_F(x) = \tanh(\beta x/2) \quad (\text{E.4})$$

$$1 + n_B(-x) = -n_B(x) \quad (\text{E.5})$$

$$n_B(x) - n_B(-x) = \coth(\beta x/2) \quad (\text{E.6})$$

$$n_F(x) + n_F(-x) = 1 \quad (\text{E.7})$$

Finally we list some limits

$$\lim_{x \rightarrow 0} x \coth\left(\frac{x}{a}\right) = a \quad (\text{E.8})$$

$$\lim_{x \rightarrow 0} x n_B(x) = T \quad (\text{E.9})$$

$$(\text{E.10})$$

F Matrix Elements of the Individual Spin Operators on Rungs

In Sec. 9.2 we have written out the spin operators \hat{s}_α^τ and \hat{S}_α^τ with $\tau = +, -, z$ on the individual sites $\alpha = 1, 2, 3$ on rungs belonging to sublattice \mathcal{A} and \mathcal{B} , respectively,

$$\hat{s}_\alpha^\tau = \sum_{\mu, \nu} s_{\alpha, \mu\nu}^\tau |\mu\rangle \langle \nu|^{\mathcal{A}}, \quad \hat{S}_\alpha^\tau = \sum_{\mu, \nu} S_{\alpha, \mu\nu}^\tau |\mu\rangle \langle \nu|^{\mathcal{B}}, \quad (\text{F.1})$$

in the basis sets $M^{\mathcal{A}}$ and $M^{\mathcal{B}}$ specified in (9.6) and (9.11). The matrix elements

$$s_{\alpha, \mu\nu}^\tau = \langle \mu | \hat{s}_\alpha^\tau | \nu \rangle^{\mathcal{A}} \quad S_{\alpha, \mu\nu}^\tau = \langle \mu | \hat{S}_\alpha^\tau | \nu \rangle^{\mathcal{B}}, \quad (\text{F.2})$$

are explicitly given by:

$$s_1^+ = \begin{pmatrix} 0 & 0 & 0 & 0 & \frac{-u+\sqrt{2}v}{\sqrt{6}} & 0 & 0 & 0 \\ \frac{-2\sqrt{2}u+v}{3\sqrt{2}} & 0 & -\frac{1}{\sqrt{3}} & 0 & 0 & \frac{u+\sqrt{2}v}{3\sqrt{2}} & 0 & 0 \\ 0 & 0 & 0 & 0 & \frac{1}{\sqrt{2}} & 0 & 0 & 0 \\ -\frac{\sqrt{2}u+v}{\sqrt{6}} & 0 & 0 & 0 & 0 & \frac{-u+\sqrt{2}v}{\sqrt{6}} & 0 & 0 \\ 0 & 0 & 0 & 0 & 0 & 0 & 0 & 0 \\ 0 & 0 & 0 & 0 & \frac{\sqrt{2}u+v}{\sqrt{6}} & 0 & 0 & 0 \\ \frac{u+2\sqrt{2}v}{3\sqrt{2}} & 0 & -\frac{1}{\sqrt{6}} & 0 & 0 & \frac{2\sqrt{2}u-v}{3\sqrt{2}} & 0 & 0 \\ 0 & -\frac{1}{\sqrt{6}} & 0 & \frac{1}{\sqrt{2}} & 0 & 0 & \frac{1}{\sqrt{3}} & 0 \end{pmatrix} = (s_1^-)^\dagger = S_1^- = (S_1^+)^\dagger$$

$$s_2^+ = \begin{pmatrix} 0 & 0 & 0 & 0 & \frac{\sqrt{2u+v}}{\sqrt{3}} & 0 & 0 & 0 \\ \frac{u-\sqrt{2}v}{3} & 0 & 0 & 0 & 0 & -\frac{\sqrt{2u+v}}{3} & 0 & 0 \\ 0 & 0 & 0 & 0 & 0 & 0 & 0 & 0 \\ 0 & 0 & -1 & 0 & 0 & 0 & 0 & 0 \\ 0 & 0 & 0 & 0 & 0 & 0 & 0 & 0 \\ 0 & 0 & 0 & 0 & \frac{u-\sqrt{2}v}{\sqrt{3}} & 0 & 0 & 0 \\ \frac{-\sqrt{2}u+2v}{3} & 0 & 0 & 0 & 0 & \frac{2u+\sqrt{2}v}{3} & 0 & 0 \\ 0 & \sqrt{\frac{2}{3}} & 0 & 0 & 0 & 0 & \frac{1}{\sqrt{3}} & 0 \end{pmatrix} = (s_2^-)^\dagger = S_2^- = (S_2^+)^\dagger$$

$$s_3^+ = \begin{pmatrix} 0 & 0 & 0 & 0 & \frac{-u+\sqrt{2}v}{\sqrt{6}} & 0 & 0 & 0 \\ \frac{-2\sqrt{2}u+v}{3\sqrt{2}} & 0 & \frac{1}{\sqrt{3}} & 0 & 0 & \frac{u+\sqrt{2}v}{3\sqrt{2}} & 0 & 0 \\ 0 & 0 & 0 & 0 & -\frac{1}{\sqrt{2}} & 0 & 0 & 0 \\ \frac{\sqrt{2}u+v}{\sqrt{6}} & 0 & 0 & 0 & 0 & \frac{u-\sqrt{2}v}{\sqrt{6}} & 0 & 0 \\ 0 & 0 & 0 & 0 & 0 & 0 & 0 & 0 \\ 0 & 0 & 0 & 0 & \frac{\sqrt{2}u+v}{\sqrt{6}} & 0 & 0 & 0 \\ \frac{u+2\sqrt{2}v}{3\sqrt{2}} & 0 & \frac{1}{\sqrt{6}} & 0 & 0 & \frac{2\sqrt{2}u-v}{3\sqrt{2}} & 0 & 0 \\ 0 & -\frac{1}{\sqrt{6}} & 0 & -\frac{1}{\sqrt{2}} & 0 & 0 & \frac{1}{\sqrt{3}} & 0 \end{pmatrix} = (s_3^-)^\dagger = S_3^- = (S_3^+)^\dagger$$

$$s_1^z = \begin{pmatrix} -\frac{(\sqrt{2}u+v)^2}{6} & 0 & \frac{-u+\sqrt{2}v}{2\sqrt{3}} & 0 & 0 & \frac{-\sqrt{2}u^2+uv+\sqrt{2}v^2}{6} & 0 & 0 \\ 0 & \frac{1}{3} & 0 & \frac{1}{2\sqrt{3}} & 0 & 0 & \frac{1}{3\sqrt{2}} & 0 \\ \frac{-u+\sqrt{2}v}{2\sqrt{3}} & 0 & 0 & 0 & 0 & \frac{\sqrt{2}u+v}{2\sqrt{3}} & 0 & 0 \\ 0 & \frac{1}{3\sqrt{2}} & 0 & 0 & 0 & 0 & -\frac{1}{\sqrt{6}} & 0 \\ 0 & 0 & 0 & 0 & -\frac{1}{2} & 0 & 0 & 0 \\ \frac{-\sqrt{2}u^2+uv+\sqrt{2}v^2}{6} & 0 & \frac{\sqrt{2}u+v}{2\sqrt{3}} & 0 & 0 & -\frac{(u-\sqrt{2}v)^2}{6} & 0 & 0 \\ 0 & \frac{1}{3\sqrt{2}} & 0 & -\frac{1}{\sqrt{6}} & 0 & 0 & \frac{1}{6} & 0 \\ 0 & 0 & 0 & 0 & 0 & 0 & 0 & \frac{1}{2} \end{pmatrix} = -S_1^z$$

$$s_2^z = \begin{pmatrix} \frac{u^2+4\sqrt{2}uv-v^2}{6} & 0 & 0 & 0 & 0 & \frac{\sqrt{2}u^2-uv-\sqrt{2}v^2}{3} & 0 & 0 \\ 0 & -\frac{1}{6} & 0 & 0 & 0 & 0 & -\frac{\sqrt{2}}{3} & 0 \\ 0 & 0 & -\frac{1}{2} & 0 & 0 & 0 & 0 & 0 \\ 0 & 0 & 0 & \frac{1}{2} & 0 & 0 & 0 & 0 \\ 0 & 0 & 0 & 0 & -\frac{1}{2} & 0 & 0 & 0 \\ \frac{\sqrt{2}u^2-uv-\sqrt{2}v^2}{3} & 0 & 0 & 0 & 0 & \frac{-u^2-4\sqrt{2}uv+v^2}{6} & 0 & 0 \\ 0 & -\frac{\sqrt{2}}{3} & 0 & 0 & 0 & 0 & \frac{1}{6} & 0 \\ 0 & 0 & 0 & 0 & 0 & 0 & 0 & \frac{1}{2} \end{pmatrix} = -S_2^z$$

$$s_3^z = \begin{pmatrix} -\frac{(\sqrt{2}u+v)^2}{6} & 0 & \frac{u-\sqrt{2}v}{2\sqrt{3}} & 0 & 0 & \frac{-\sqrt{2}u^2+uv+\sqrt{2}v^2}{6} & 0 & 0 \\ 0 & \frac{1}{3} & 0 & -\frac{1}{2\sqrt{3}} & 0 & 0 & \frac{1}{3\sqrt{2}} & 0 \\ \frac{u-\sqrt{2}v}{2\sqrt{3}} & 0 & 0 & 0 & 0 & -\frac{\sqrt{2}u+v}{2\sqrt{3}} & 0 & 0 \\ 0 & -\frac{1}{3\sqrt{2}} & 0 & 0 & 0 & 0 & \frac{1}{\sqrt{6}} & 0 \\ 0 & 0 & 0 & 0 & -\frac{1}{2} & 0 & 0 & 0 \\ \frac{-\sqrt{2}u^2+uv+\sqrt{2}v^2}{6} & 0 & -\frac{\sqrt{2}u+v}{2\sqrt{3}} & 0 & 0 & -\frac{(u-\sqrt{2}v)^2}{6} & 0 & 0 \\ 0 & \frac{1}{3\sqrt{2}} & 0 & \frac{1}{\sqrt{6}} & 0 & 0 & \frac{1}{6} & 0 \\ 0 & 0 & 0 & 0 & 0 & 0 & 0 & \frac{1}{2} \end{pmatrix} = -S_3^z$$

G Analysis of \tilde{E}_0 , \hat{H}_{a0} , \hat{H}_{c0} , \hat{H}_{a1} , and \hat{H}_{c2}

In this appendix, we expand and analyze the terms in the Hamiltonian (9.25) which have no influence on the low energy spectrum in this appendix. These terms, however, are required for the evaluation of the ground state energy.

The Bare Ground State Energy \tilde{E}_0

The bare ground state energy \tilde{E}_0 accounts for the constant terms in the Hamiltonian (9.16). It is given by $\tilde{E}_0 = \sum_{\mathbf{k}} 2\tilde{\varepsilon}_0 = N\tilde{\varepsilon}_0$ with

$$\begin{aligned}\tilde{\varepsilon}_0 &= \frac{1}{2} - \frac{3}{2}u^2 + J \sum_{\alpha=1}^3 s_{\alpha,11}^z S_{\alpha,11}^z + J' s_{3,11}^z S_{1,11}^z \\ &= -1.45842.\end{aligned}\tag{G.1}$$

Evaluation of the Spectrum of \hat{H}_{a0}

The term \hat{H}_{a0} is given by

$$\begin{aligned}\hat{H}_{a0} &= \sum_{\mathbf{k}} \left[\varepsilon_{a0} (a_{0,\mathbf{k}}^\dagger a_{0,\mathbf{k}} + A_{0,\mathbf{k}}^\dagger A_{0,\mathbf{k}}) \right. \\ &\quad \left. + \xi_{a0,\mathbf{k}} (a_{0,\mathbf{k}}^\dagger + a_{0,\mathbf{k}}) (A_{0,\mathbf{k}}^\dagger + A_{0,\mathbf{k}}) \right],\end{aligned}\tag{G.2}$$

with

$$\varepsilon_{a0} = -\frac{1}{2} + \frac{3}{2}u^2 - 2J \sum_{\alpha=1}^3 s_{\alpha,11}^z S_{\alpha,11}^z - 2J' s_{3,11}^z S_{1,11}^z,\tag{G.3}$$

$$\xi_{a0,\mathbf{k}} = J' \cos(4k_x) s_{3,13}^z S_{1,13}^z + J \cos k_y \sum_{\alpha=1}^3 s_{\alpha,13}^z S_{\alpha,13}^z.\tag{G.4}$$

To a reasonable approximation, we obtain low energy modes described by \hat{H}_{a0} by diagonalizing (G.2) at each point in \mathbf{k} space in the reduced Hilbert space spanned by

$$|\tilde{0}\rangle, a_0^\dagger|\tilde{0}\rangle, A_0^\dagger|\tilde{0}\rangle, \text{ and } a_0^\dagger A_0^\dagger|\tilde{0}\rangle,$$

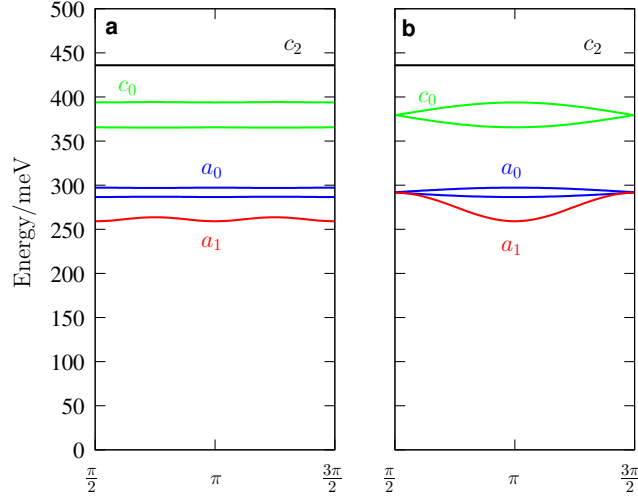


Figure G.1: Modes described by \hat{H}_{a0} (blue), \hat{H}_{c0} (green), \hat{H}_{a1} (red), \hat{H}_{c-2} (black) plotted as cuts (a) along (k_x, π) and (b) along (π, k_y) using $J_{\text{exp}} = 140$ meV.

where

$$|\tilde{0}\rangle \equiv \prod_{i \in \mathcal{A}} |\tilde{b}_{-1/2}\rangle_i \cdot \prod_{j \in \mathcal{B}} |\tilde{b}_{1/2}\rangle_j \quad (\text{G.5})$$

is the bare vacuum unrenormalized by spin wave theory. This yields two almost dispersionless modes

$$(\omega_{a0, \mathbf{k}})_{1/2} = \sqrt{\varepsilon_{a0}^2 + \xi_{a0, \mathbf{k}}^2} \pm \xi_{a0, \mathbf{k}}, \quad (\text{G.6})$$

with energies of about $\varepsilon_{a0} = 2.07$, or 290 meV if we assume $J_{\text{exp}} = 140$ meV. Cuts of the dispersions of these two modes are shown in blue (color online) in Fig. G.1. \hat{H}_{a0} also gives rise to a contribution

$$E_{a0} = \sum_{\mathbf{k}} \left(\varepsilon_{a0} - \sqrt{\varepsilon_{a0}^2 + \xi_{a0, \mathbf{k}}^2} \right) = -0.00008 N \quad (\text{G.7})$$

to the ground state energy. (Here N denotes the number of rungs, which implies that the sum extends over $\frac{N}{2}$ values for \mathbf{k} .)

Evaluation of the Spectrum of \hat{H}_{c0}

A similar analysis of

$$\begin{aligned} \hat{H}_{c0} = \sum_{\mathbf{k}} & \left[\varepsilon_{c0} (c_{0, \mathbf{k}}^\dagger c_{0, \mathbf{k}} + C_{0, \mathbf{k}}^\dagger C_{0, \mathbf{k}}) \right. \\ & \left. + \xi_{c0, \mathbf{k}} (c_{0, \mathbf{k}}^\dagger + c_{0, \mathbf{k}}) (C_{0, \mathbf{k}}^\dagger + C_{0, \mathbf{k}}) \right], \end{aligned} \quad (\text{G.8})$$

with

$$\begin{aligned}\varepsilon_{c0} &= \frac{3}{2}(u^2 - v^2) + 2J \sum_{\alpha=1}^3 s_{\alpha,11}^z (S_{\alpha,66}^z - S_{\alpha,11}^z) \\ &+ 2J' s_{3,11}^z (S_{1,66}^z - S_{1,11}^z),\end{aligned}\tag{G.9}$$

$$\xi_{c0,\mathbf{k}} = J' \cos(4k_x) s_{3,16}^z S_{1,16}^z + J \cos k_y \sum_{\alpha=1}^3 s_{\alpha,16}^z S_{\alpha,16}^z,\tag{G.10}$$

yields two additional, almost dispersionless modes

$$(\omega_{c0,\mathbf{k}})_{1/2} = \sqrt{\varepsilon_{c0}^2 + \xi_{c0,\mathbf{k}}^2} \pm \xi_{c0,\mathbf{k}},\tag{G.11}$$

with energies of about $\varepsilon_{c0} = 2.71$, or 380 meV, which is shown in green (color online) in Fig. G.1. $\hat{\mathbf{H}}_{c0}$ also gives rise to a contribution

$$E_{c0} = \sum_{\mathbf{k}} \left(\varepsilon_{c0} - \sqrt{\varepsilon_{c0}^2 + \xi_{c0,\mathbf{k}}^2} \right) = -0.00048 N\tag{G.12}$$

to the ground state energy.

Evaluation of the Spectrum of $\hat{\mathbf{H}}_{a1}$

The term

$$\begin{aligned}\hat{\mathbf{H}}_{a1} &= \sum_{\mathbf{k}} \left[\varepsilon_{a1} (a_{1,\mathbf{k}}^\dagger a_{1,\mathbf{k}} + A_{-1,\mathbf{k}}^\dagger A_{-1,\mathbf{k}}) \right. \\ &\quad \left. + \xi_{a1,\mathbf{k}} (a_{1,\mathbf{k}}^\dagger A_{-1,\mathbf{k}}^\dagger + a_{1,\mathbf{k}} A_{-1,\mathbf{k}}) \right],\end{aligned}\tag{G.13}$$

with $\varepsilon_{a1} = \varepsilon_{a0}$ as given in (G.3) and

$$\xi_{a1,\mathbf{k}} = J' \cos(4k_x) s_{3,41}^+ S_{1,41}^- + J \cos k_y \sum_{\alpha=1}^3 s_{\alpha,41}^+ S_{\alpha,41}^-, \tag{G.14}$$

can be diagonalized by a Bogoliubov transformation. We obtain

$$\hat{\mathbf{H}}_{a1} = \sum_{\mathbf{k}} \left[\omega_{a1,\mathbf{k}} (\alpha_{1,\mathbf{k}}^\dagger \alpha_{1,\mathbf{k}} + \alpha_{2,\mathbf{k}}^\dagger \alpha_{2,\mathbf{k}}) + \omega_{a1,\mathbf{k}} - \varepsilon_{a1} \right]\tag{G.15}$$

with

$$\omega_{a1,\mathbf{k}} = \sqrt{\varepsilon_{a1}^2 - \xi_{a1,\mathbf{k}}^2}.\tag{G.16}$$

It yields a two-fold degenerate, weakly dispersing mode with an energy of about 1.95, or 273 meV, which is shown in red (color online) in Fig. G.1, as well as a contribution

$$E_{a1} = \sum_{\mathbf{k}} \left(\omega_{a1,\mathbf{k}} - \varepsilon_{a1} \right) = -0.05363 N\tag{G.17}$$

to the ground state energy.

Evaluation of the Spectrum of \hat{H}_{c2}

Finally,

$$\hat{H}_{c2} = \sum_{\mathbf{k}} \omega_{c2} (c_{2,\mathbf{k}}^\dagger c_{2,\mathbf{k}} + C_{-2,\mathbf{k}}^\dagger C_{-2,\mathbf{k}}) \quad (\text{G.18})$$

with

$$\begin{aligned} \omega_{c2} = & \frac{3}{2} u^2 + 2J \sum_{\alpha=1}^3 s_{\alpha,11}^z (S_{\alpha,88}^z - S_{\alpha,11}^z) \\ & + 2J' s_{3,11}^z (S_{1,88}^z - S_{1,11}^z), \end{aligned} \quad (\text{G.19})$$

describes a two-fold degenerate, completely dispersionless mode with an energy of $\omega_{c2} = 3.12$, or 436 meV.

Ground State Energy

To evaluate the ground state energy E_0 , we collect the contributions from (G.1), (G.7), (G.12), (G.17), and (9.42). This yields

$$E_0 = -1.73378 N, \quad (\text{G.20})$$

where N is the number of rungs. This number is in excellent agreement with what we would expect from the results for small clusters of 12, 18 and 24 sites with unfrustrated boundary conditions.

H Matrix Elements

The dynamical structure factor measured in neutron scattering is given by

$$\chi^{+-}(\mathbf{k}, \omega) = \sum_n |\langle 0 | \hat{S}_{\mathbf{k}}^+ | n \rangle|^2 \delta(\omega - \omega_n), \quad (\text{H.1})$$

where $|0\rangle$ is the ground state and the sum extends over all excited states $|n\rangle$ with energy ω_n , and

$$\hat{S}_{\mathbf{k}}^+ = \sum_l e^{-i\mathbf{k}\mathbf{r}_l} \hat{S}_l^+ \quad (\text{H.2})$$

is the Fourier transform of the spin raising operator \hat{S}_l at lattice site l with respect to original lattice, *i.e.*, the sum runs over all lattice sites. This implies

$$\mathbf{r}_{i,\alpha} = \mathbf{R}_i + \begin{pmatrix} \alpha - 2 \\ 0 \end{pmatrix}, \quad \mathbf{r}_{j,\alpha} = \mathbf{R}_j + \begin{pmatrix} \alpha - 2 \\ 0 \end{pmatrix}, \quad (\text{H.3})$$

with \mathbf{R}_i and \mathbf{R}_j as indicated in Fig. 9.3 for sublattices A and B , respectively. In analogy to Fourier transforms of the bosonic creation and annihilation operators (9.22) and (9.23), we further Fourier transform the spin operators with respect to the rung sublattices \mathcal{A} and \mathcal{B} according to

$$\hat{s}_{\mathbf{k},\alpha}^+ = \sqrt{\frac{2}{N}} \sum_{i \in \mathcal{A}} e^{-i\mathbf{k}\mathbf{R}_i} \hat{s}_{i,\alpha}^+, \quad \hat{S}_{\mathbf{k},\alpha}^+ = \sqrt{\frac{2}{N}} \sum_{j \in \mathcal{B}} e^{-i\mathbf{k}\mathbf{R}_j} \hat{S}_{j,\alpha}^+, \quad (\text{H.4})$$

and express the operator (H.2) in terms of them:

$$\begin{aligned} \hat{S}_{\mathbf{k}}^+ &= \sqrt{\frac{2}{N}} \left\{ \sum_{i \in \mathcal{A}} \sum_{\alpha} e^{-i\mathbf{k}\mathbf{r}_{i,\alpha}} \hat{s}_{i,\alpha}^+ + \sum_{j \in \mathcal{B}} \sum_{\alpha} e^{-i\mathbf{k}\mathbf{r}_{j,\alpha}} \hat{S}_{j,\alpha}^+ \right\} \\ &= \sum_{\alpha} e^{-ik_x(\alpha-2)} s_{\mathbf{k},\alpha}^+ + \sum_{\alpha} e^{-ik_x(\alpha-2)} S_{\mathbf{k},\alpha}^+ \\ &= \sum_{\alpha} e^{-ik_x(\alpha-2)} (\hat{s}_{\mathbf{k},\alpha}^+ + \hat{S}_{\mathbf{k},\alpha}^+) \end{aligned} \quad (\text{H.5})$$

As we are interested only in the contribution of the low-energy mode $\omega_{\mathbf{k},1}$ to $\chi^{+-}(\mathbf{k}, \omega)$, the only matrix element we need to evaluate is

$$|\langle 0 | \hat{S}_{\mathbf{k}}^+ | \gamma_{1,\mathbf{k}} \rangle|^2 = |\langle 0 | \hat{S}_{\mathbf{k}}^+ \gamma_{1,\mathbf{k}}^\dagger | 0 \rangle|^2 \quad (\text{H.6})$$

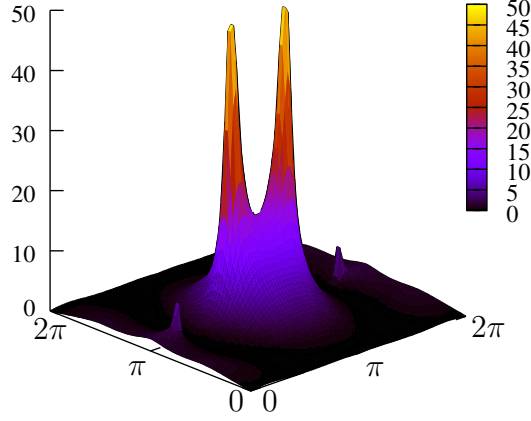


Figure H.1: Numerical evaluation of the matrix elements $|\langle 0 | \hat{S}_{\mathbf{k}}^+ | \gamma_{1,\mathbf{k}} \rangle|^2$ for the entire Brillouin zone $\mathbf{k} \in [0, 2\pi] \times [0, 2\pi]$. Note the strong enhancement around the antiferromagnetic ordering wave vectors $\mathbf{k} = (\pi \pm \pi/4, \pi)$.

for all values of \mathbf{k} . (The second low-energy mode $\omega_{\mathbf{k},2}$, which is degenerate with the first, does not contribute to (H.6) and hence to $\chi^{+-}(\mathbf{k}, \omega)$, but instead yields a contribution to $\chi^{-+}(\mathbf{k}, \omega)$ which is identical to the one we calculate below.) Keeping only terms which contribute to this mode and are linear in the expansion (9.13) of \hat{s}_α^+ , we obtain for sublattice \mathcal{A}

$$\hat{s}_\alpha^+ = s_{\alpha,21}^+ b_1^\dagger + s_{\alpha,71}^+ c_1^\dagger + s_{\alpha,15}^+ c_{-1}$$

or in Fourier space with (H.4), (9.22), and (9.27)

$$\hat{s}_{\mathbf{k},\alpha}^+ = s_{\alpha,21}^+ b_{1,\mathbf{k}}^\dagger + s_{\alpha,71}^+ c_{1,\mathbf{k}}^\dagger + s_{\alpha,15}^+ c_{-1,-\mathbf{k}} = (0, s_{\alpha,21}^+, 0, s_{\alpha,71}^+, 0, s_{\alpha,15}^+) \cdot \Psi_{\mathbf{k}} \quad (\text{H.7})$$

and similarly with (9.15) and (9.23) for \mathcal{B}

$$\hat{S}_{\mathbf{k},\alpha}^+ = S_{\alpha,12}^+ B_{-1,\mathbf{k}} + S_{\alpha,17}^+ C_{-1,\mathbf{k}} + S_{\alpha,51}^+ C_{1,-\mathbf{k}}^\dagger = (S_{\alpha,12}^+, 0, S_{\alpha,17}^+, 0, S_{\alpha,51}^+, 0) \cdot \Psi_{\mathbf{k}}. \quad (\text{H.8})$$

We then use $\Psi_{\mathbf{k}} = M_{\mathbf{k}} \Gamma_{\mathbf{k}}$ and (9.41) to express $\hat{s}_{\mathbf{k},\alpha}^+$ and $\hat{S}_{\mathbf{k},\alpha}^+$ in terms of $\gamma_{i,\mathbf{k}}$ and $\gamma_{i,\mathbf{k}}^\dagger$, recall $S_{\alpha,ji}^+ = s_{\alpha,ij}^+$, and finally obtain

$$\begin{aligned} |\langle 0 | \hat{S}_{\mathbf{k}}^+ | \gamma_{1,\mathbf{k}} \rangle|^2 &= \left| \sum_{\alpha=1}^3 e^{-ik_x(\alpha-2)} \{ s_{\alpha,21}^+ (M_{\mathbf{k},11} + M_{\mathbf{k},21}) \right. \\ &\quad \left. + s_{\alpha,71}^+ (M_{\mathbf{k},31} + M_{\mathbf{k},41}) + s_{\alpha,15}^+ (M_{\mathbf{k},51} + M_{\mathbf{k},61}) \} \right|^2 \end{aligned} \quad (\text{H.9})$$

Note that $\chi^{zz}(\mathbf{k}, \omega) = 0$ as there is no term linear in b_1^\dagger , c_1^\dagger , or c_{-1} in the expansion (9.13) for \hat{s}_α^z .

I Staggered Magnetization

The staggered magnetizations on the outer and inner chains of our three-leg ladders, $-\langle \hat{s}_1^z \rangle = -\langle \hat{s}_3^z \rangle = \langle \hat{S}_1^z \rangle = \langle \hat{S}_3^z \rangle$ and $\langle \hat{s}_2^z \rangle = -\langle \hat{S}_2^z \rangle$, respectively, are given in by the the bare values $s_{\alpha,11}^z = -S_{\alpha,11}^z$ with $\alpha = 1, 2, 3$ minus corrections from the individual terms in (9.25). The bare expectation values are explicitly given by

$$\langle \hat{s}_2^z \rangle_{\text{bare}} = s_{2,11}^z = 0.4265 \quad (\text{I.1})$$

$$\langle \hat{s}_3^z \rangle_{\text{bare}} = s_{3,11}^z = -0.4633 \quad (\text{I.2})$$

To begin with we focus on corrections of these bare values due to the part $\hat{H}_{b_1, c_1, c_{-1}}$ of the Hamiltonian. From equ. 9.13 the relevant part of \hat{s}_α^z belonging the this subspace is singled out as

$$\begin{aligned} \hat{s}_\alpha^z &= b_1^\dagger b_1 (s_{\alpha,22}^z - s_{\alpha,11}^z) + c_1^\dagger c_1 (s_{\alpha,77}^z - s_{\alpha,11}^z) \\ &+ c_{-1}^\dagger c_{-1} (s_{\alpha,55}^z - s_{\alpha,11}^z) + (b_1^\dagger c_1 + c_1^\dagger b_1) s_{\alpha,27}^z. \end{aligned} \quad (\text{I.3})$$

If we define

$$\begin{aligned} \rho_{\alpha,1} &= (s_{\alpha,22}^z - s_{\alpha,11}^z) \\ \rho_{\alpha,2} &= (s_{\alpha,77}^z - s_{\alpha,11}^z) \\ \rho_{\alpha,3} &= (s_{\alpha,55}^z - s_{\alpha,11}^z), \end{aligned} \quad (\text{I.4})$$

and then express the operators b_1, c_1, c_{-1} via $\Psi = M\Gamma$ through the γ operators and furthermore note that $\gamma_j|0\rangle = \langle 0|\gamma_j^\dagger = 0$ and $\langle 0|\gamma_i\gamma_j^\dagger|0\rangle = \delta_{ij}$ the corrections from $\hat{H}_{b_1, c_1, c_{-1}}$ to the bare value are written as

$$\begin{aligned} \langle \hat{s}_\alpha^z \rangle_{\text{corr}, \hat{H}_{b_1, c_1, c_{-1}}} &= \frac{2}{N} \sum_{\mathbf{k}} \left\{ \left(\rho_{\alpha,1} M_{\mathbf{k},21} M_{\mathbf{k},12}^T + \rho_{\alpha,2} M_{\mathbf{k},41} M_{\mathbf{k},14}^T + \rho_{\alpha,3} M_{\mathbf{k},62} M_{\mathbf{k},26}^T \right. \right. \\ &+ s_{\alpha,27}^z [M_{\mathbf{k},21} M_{\mathbf{k},14}^T + M_{\mathbf{k},41} M_{\mathbf{k},12}^T] \left. \right) \\ &+ \left(\rho_{\alpha,1} M_{\mathbf{k},23} M_{\mathbf{k},32}^T + \rho_{\alpha,2} M_{\mathbf{k},43} M_{\mathbf{k},34}^T + \rho_{\alpha,3} M_{\mathbf{k},64} M_{\mathbf{k},46}^T \right. \\ &+ s_{\alpha,27}^z [M_{\mathbf{k},23} M_{\mathbf{k},34}^T + M_{\mathbf{k},43} M_{\mathbf{k},32}^T] \left. \right) \\ &+ \left(\rho_{\alpha,1} M_{\mathbf{k},26} M_{\mathbf{k},62}^T + \rho_{\alpha,2} M_{\mathbf{k},46} M_{\mathbf{k},64}^T + \rho_{\alpha,3} M_{\mathbf{k},65} M_{\mathbf{k},56}^T \right. \\ &+ s_{\alpha,27}^z [M_{\mathbf{k},26} M_{\mathbf{k},64}^T + M_{\mathbf{k},46} M_{\mathbf{k},62}^T] \left. \right) \left. \right\}. \end{aligned}$$

This expression is arranged such that the first line corresponds to corrections originating from the lowest eigenmodes γ_1, γ_2 , whereas the second line refers to corrections from the modes γ_3, γ_4 followed by corrections from modes generated by γ_5, γ_6 in the third line. In total the corrections amount out

$$\langle \hat{s}_2^z \rangle_{\text{corr}, \hat{H}_{b_1, c_1, c-1}} = -0.1075 \quad (\text{I.5})$$

$$\langle \hat{s}_3^z \rangle_{\text{corr}, \hat{H}_{b_1, c_1, c-1}} = 0.1773 \quad (\text{I.6})$$

For completeness we single out these individual correction contributions

$$\begin{aligned} \langle \hat{s}_2^z \rangle_{\text{corr}, \gamma_1, \gamma_2} &= -0.0864 & \langle \hat{s}_3^z \rangle_{\text{corr}, \gamma_1, \gamma_2} &= 0.1752 \\ \langle \hat{s}_2^z \rangle_{\text{corr}, \gamma_3, \gamma_4} &= -0.0210 & \langle \hat{s}_3^z \rangle_{\text{corr}, \gamma_3, \gamma_4} &= 0.0018 \\ \langle \hat{s}_2^z \rangle_{\text{corr}, \gamma_5, \gamma_6} &= -0.0001 & \langle \hat{s}_3^z \rangle_{\text{corr}, \gamma_5, \gamma_6} &= 0.0003. \end{aligned}$$

For sake of simplicity we have left out the subscript $\hat{H}_{b_1, c_1, c-1}$. As expected the major contributions stem from the lowest mode.

An analogous consideration may be achieved for the sector \hat{H}_{a_1} . In this case we have to subject the operators to a Bogoliubov transformation as in case of $\hat{H}_{b_1, c_1, c-1}$ with $\Psi_a = (A_{-1}, a_1^\dagger)^T$. The corresponding transformation matrix M_a is two dimensional. The only relevant term in this subspace to \hat{s}_α^z is $-s_{\alpha, 11}^z a_1^\dagger a_1$ (no contribution from the mixed terms $a_1 b_1$ and $a_1 c_1$) which gives rise to the correction

$$\langle \hat{s}_\alpha^z \rangle_{\text{corr}, \hat{H}_{a_1}} = -\frac{2}{N} \sum_{\mathbf{k}} s_{\alpha, 11}^z M_{a, \mathbf{k}, 21} M_{a, \mathbf{k}, 12}^T \quad (\text{I.7})$$

Hence we obtain the corrections

$$\langle \hat{s}_2^z \rangle_{\text{corr}, \hat{H}_{a_1}} = -0.0117 \quad \langle \hat{s}_3^z \rangle_{\text{corr}, \hat{H}_{a_1}} = 0.0127.$$

Finally we have a negligible correction from the \hat{H}_{a_0} and \hat{H}_{c_0} sectors which are given by

$$\langle \hat{s}_\alpha^z \rangle_{\text{corr}, \hat{H}_{a_0}} = (-s_{\alpha, 11}^z) \frac{2}{N} \sum_{\mathbf{k}} \frac{1}{N_{a_0, \mathbf{k}}^2} \quad (\text{I.8})$$

$$\langle \hat{s}_\alpha^z \rangle_{\text{corr}, \hat{H}_{c_0}} = (s_{\alpha, 66} - s_{\alpha, 11}^z) \frac{2}{N} \sum_{\mathbf{k}} \frac{1}{N_{c_0, \mathbf{k}}^2} \quad (\text{I.9})$$

where

$$N_{a_0, \mathbf{k}}^2 = \left(\frac{\epsilon_{a_0} + \sqrt{\epsilon_{a_0}^2 + \xi_{a_0, \mathbf{k}}^2}}{\xi_{a_0, \mathbf{k}}} \right)^2 + 1 \quad (\text{I.10})$$

$$N_{c_0, \mathbf{k}}^2 = \left(\frac{\epsilon_{c_0} + \sqrt{\epsilon_{c_0}^2 + \xi_{c_0, \mathbf{k}}^2}}{\xi_{c_0, \mathbf{k}}} \right)^2 + 1 \quad (\text{I.11})$$

with ϵ_{a0} and $\xi_{a0,\mathbf{k}}$ as given in (G.3) and ϵ_{c0} and $\xi_{c0,\mathbf{k}}$ as given in (G.9). These corrections explicitly read

$$\langle \hat{s}_2^z \rangle_{\text{corr}, \hat{H}_{a0}} = -0.000033 \quad (\text{I.12})$$

$$\langle \hat{s}_3^z \rangle_{\text{corr}, \hat{H}_{a0}} = 0.000017 \quad (\text{I.13})$$

$$\langle \hat{s}_2^z \rangle_{\text{corr}, \hat{H}_{c0}} = -0.000076 \quad (\text{I.14})$$

$$\langle \hat{s}_3^z \rangle_{\text{corr}, \hat{H}_{c0}} = 0.000082 \quad (\text{I.15})$$

and may be safely neglected. Hence, in total we obtain

$$\langle \hat{s}_2^z \rangle = 0.3073 \quad \langle \hat{s}_3^z \rangle = -0.2733. \quad (\text{I.16})$$

List of Figures

3.1	Possible impurity configuration for the Anderson model	14
3.2	Magnetic and non magnetic phases for the Anderson model	14
3.3	Effective spin flip	15
3.4	Mechanisms leading to an an attenuation of the Kondo effect	17
3.5	Resistivity curve for the Kondo model	18
3.6	Anderson’s poor man scaling approach	19
3.7	“Wilson-chain”	20
4.1	FRG flow equations	28
4.2	Schwinger contour	30
4.3	FRG flow equations for the Kondo model	37
4.4	Modified FRG flow equations for the Kondo model	39
5.1	Second order diagrams	42
5.2	Rederivation of the perturbative results via the FRG	44
5.3	Equilibrium: conductance	52
5.4	Equilibrium: imaginary part of the self energy	53
5.5	Equilibrium: leading component	54
5.6	Frequency dependent coupling function in equilibrium	55
5.7	Nonequilibrium: conductance and imaginary part of the self energy	57
5.8	Nonequilibrium: finite temperature	57
5.9	Difference in the flow of Γ	58
5.10	Leading component of the coupling function $g(\omega)$ versus ω/T_K for various values of V/T_K	60
5.11	Imaginary part of the self energy Γ versus V/T_K . Dots: numerical results from FRG; solid line: $\Gamma = \frac{3\pi}{4}V \frac{1}{(2\log(V/2T_K))^2}$	60
5.12	Conductance $G/G_0 = I/V$ versus V/T_K . Dots: numerical result from FRG; solid line: $G/G_0 = \frac{3\pi^2}{16} \frac{1}{\log^2(V/2T_K)}$	61
5.13	Effective spin flip	61
5.14	Nonequilibrium: finite temperature	62
5.15	Nonequilibrium: finite temperature	62
5.16	Self consistent equations: g and Γ	63
5.17	Conductance at strong coupling - equilibrium	64
5.18	Conductance at strong coupling - nonequilibrium	65
6.1	Kondo dot: experimental setup	68
6.2	Anderson model: dot occupancy	68

6.3	Conductance: experiment 1	69
6.4	Conductance: experiment 2	70
6.5	Kondo dot: Nonequilibrium measurements	71
8.1	Bond vs. site centered stripe models	78
9.1	Single rung on sublattice \mathcal{A}	81
9.2	Bosonic operators	84
9.3	Microscopic model for site centered spin stripes	85
9.4	Reduced Brillouin zone	87
9.5	Modes: cuts along (k_x, π) and (π, k_y)	91
10.1	phase diagram the coupled even- and odd-leg ladders	94
10.2	Finite size geometries to determine J'	95
10.3	The dispersion $\omega(k_x, k_y)$ of the lowest eigenmode	96
10.4	Superpositions of cuts along (k_x, π) and (π, k_y)	97
10.5	Constant energy slices of the neutron scattering intensity	98
10.6	The saddle point energy $\omega(\pi, \pi)$ of the lowest magnetic mode	99
10.7	Auxiliary models: coupled three-leg ladders and two spin $\frac{1}{2}$ chains	100
G.1	High energy modes	122
H.1	Matrix elements	126

Bibliography

- [1] L Kouwenhoven and L. Glazman. Revival of the Kondo effect. *Physics world*, page 33, 2001.
- [2] W. de Haas, h. Boer, and G. van den Berg. *Physica*, 1:1115, 1934.
- [3] M.P. Sarachik, E. Corenzwit, and L.D. Longinotti. Resistivity of mo-nb and mo-re alloys containing 1 % *fe*. *Phys. Rev. A*, 135:1041, 1964.
- [4] J. Kondo. Resistance minimum in dilute magnetic alloys. *Prog. Theo. Phys.*, 32:37, 1964.
- [5] D.R. Hamann. New solution for exchange scattering in dilute alloys. *Phys. Rev.*, 158:570, 1967.
- [6] Y. Nagaoka. Self-consistent treatment of kondo's effect in dilute alloys. *Phys. Rev.*, 138:A1112, 1965.
- [7] H. Suhl. Dispersion theory of the kondo effect. *Phys. Rev.*, 138:A515, 1965.
- [8] C. Y. Cheung and R. D. Mattuck. Removing the divergence at the kondo temperature by means of self-consistent perturbation theory. *Phys. Rev. B*, 2:2735, 1970.
- [9] R.D. Mattuck. *A guide to Feynman diagrams in the many body problem*. McGraw-Hill International Book Company, 1967.
- [10] P. Noizeres. A Fermi-Liquid Description of the Kondo Problem at Low Temperatures. *J. of Low Temp. Phys.*, 17:31, 1974.
- [11] P. W. Anderson. A poor man's derivation of scaling laws for the kondo problem. *J. Phys. C.*, 3:2436, 1970.
- [12] K.G. Wilson and J. Kogut. The renormalization group and the ϵ expansion. *Phys. Rep. C*, 12:75, 1974.
- [13] K.G. Wilson. The renormalization group: Critical phenomena and the Kondo problem. *Rev. Mod. Phys.*, 47:773, 1975.
- [14] N. Andrei. Diagonalization of the kondo hamiltonian. *Phys. Rev. Lett.*, 45:3, 1980.
- [15] P.B. Wiegmann. Exact solution of the s-d exchange model (kondo problem). *J. Phys. C: Solid State Phys.*, 14:1463, 1981.

- [16] L.V. Keldysh. Diagram technique for nonequilibrium processes. *Zh. Eksp. Theor. Fiz.*, 47:1515, 1964.
- [17] A. Rosch, J. Paaske, J. Kroha, and P. Wölfle. Nonequilibrium transport through a Kondo dot in a magnetic field: Perturbation theory and poor man's scaling. *Phys. Rev. Lett.*, 90:076804, 2003.
- [18] A. Rosch, J. Paaske, J. Kroha, and P. Wölfle. The Kondo effect in non-equilibrium quantum dots: Perturbative renormalization group. *J. Phys. Soc. Jpn.*, 74:118, 2005.
- [19] D. Goldhaber-Gordon, H. Shtrikman, D. Mahalu, D. Abusch-Magder, U. Meirav, and M.A. Kastner. Kondo effect in a single-electron transistor. *Nature*, 391:156, 1998.
- [20] D. Goldhaber-Gordon, J. Göres, M. A. Kastner, Hadas Shtrikman, D. Mahalu, and U. Meirav. From the kondo regime to the mixed-valence regime in a single-electron transistor. *Phys. Rev. Lett.*, 81:5225, 1998.
- [21] S.M. Cronenwett, T.H. Oosterkamp, and L.P. Kouwenhoven. A Tunable Kondo Effect in Quantum Dots. *Science*, 281:540, 1998.
- [22] W.G. van der Wiel, S. De Franceschi, T. Fujisawa, J.M. Elzerman, S. Tarucha, and L.P. Kouwenhoven. The Kondo effect in the unitary limit. *Science*, 289:2105, 2000.
- [23] R. M. Potok H. Shtrikman M. Grobis, I. G. Rau and D. Goldhaber-Gordon. Universal scaling in nonequilibrium transport through a single channel kondo dot. *Phys. Rev. Lett.*, 100:246601, 2008.
- [24] A.A. Abrikosov. Electron scattering on magnetic impurities in metals and anomalous resistivity effects. *Physics*, 2:5, 1965.
- [25] A.A. Abrikosov. Electron scattering on magnetic impurities in metals and anomalous resistivity effects. *Physics*, 2:61, 1965.
- [26] A. Kamenev. Many-body theory of non-equilibrium systems. *cond-mat/0412296*, 2005.
- [27] P. W. Anderson. Localized magnetic states in metals. *Phys. Rev.*, 124:41, 1969.
- [28] R. Noack and S. Manmana. Diagonalization- and Numerical Renormalization-Group-Based Methods for Interacting Quantum Systems. *AIP Conf. Proc.*, 789:93–163, 2005.
- [29] J. R. Schrieffer and P. A. Wolff. Relation between the anderson and kondo hamiltonians. *Phys. Rev.*, 149:491, 1966.
- [30] A.C. Hewson. *The Kondo Problem to Heavy Fermions*. Cambridge University Press, 1993.

-
- [31] H. Bruus and K. Flensberg. *Many-Body Quantum Theory in Condensed Matter Physics*. Oxford University Press, 2004.
- [32] M. Pustilnik and L. Glazman. Kondo effect in quantum dots. *J.Phys.: Condens. Matter*, 16:513, 2004.
- [33] M. Salmhofer and C. Honerkamp. Fermionic renormalization group flows. *Prog. Th. Phys.*, 105(1), 2001.
- [34] W. Metzner. Functional renormalization group computation of interacting fermi systems. *Prog. Th. Phys.*, 160:58, 2006.
- [35] C.J. Halboth and W. Metzner. Renormalization-group analysis of the two-dimensional Hubbard model. *Phys. Rev. B*, 61(11):7364, 2000.
- [36] S. Andergassen, T. Enss, V. Meden, W. Metzner, U. Schollwöck, and K. Schönhammer. Functional renormalization group for Luttinger liquids with impurities. *Phys. Rev. B*, 70:075102, 2004.
- [37] S. Andergassen, T. Enss, and V. Meden. Kondo physics in transport through a quantum dot with luttinger-liquid leads. *Phys. Rev. B*, 73:153308, 2006.
- [38] T. Enss. *Renormalization, Conservation Laws and Transport in Correlated Electron Systems*. PhD thesis, Max-Planck Institut für Festkörperforschung, Stuttgart, Februar 2005.
- [39] R. Hedden, V. Meden, Th. Pruschke, and K. Schoenhammer. A functional renormalization group approach to zero-dimensional interacting systems. *J. Phys. Condens. Matter*, 16:5279, 2004.
- [40] C. Karrasch, T. Enss, and V. Meden. Functional renormalization group approach to transport through correlated quantum dots. *Phys. Rev. B*, 73:235337, 2006.
- [41] S. Andergassen, T. Enss, C. Karrasch, and V. Meden. A gentle introduction to the functional renormalization group: The kondo effect in quantum dots. 2008.
- [42] S. Jakobs, M. Pletyukhov, and H. Schoeller. Properties of multi-particle green and vertex functions within keldysh formalism. preprint arXiv:0902.2350, 2009.
- [43] R. Gezzi, Th. Pruschke, and V. Meden. Functional renormalization group for nonequilibrium quantum many-body problems. *Phys. Rev. B*, 75:045324, 2007.
- [44] S. Jakobs, V. Meden, and H. Schoeller. Nonequilibrium functional renormalization group for interacting quantum systems. *Phys. Rev. Lett.*, 99:150603, 2007.
- [45] S. Jakobs. Renormierungsgruppen-Methoden für nichtlinearen Transport. Master's thesis, RWTH Aachen, November 2003.
-

- [46] John W. Negele and Henri Orland. *Quantum Many-Particle Systems*. Addison-Wesley, New York, 1988.
- [47] J.J. Sakurai. *Modern Quantum mechanics*. Addison Wesley Longman, 1994.
- [48] T.R. Morris. *Int. J. Mod. Phys. A*, 9:2411, 1994.
- [49] A.A. Abrikosov, L.P. Gorkov, and I.E. Dzyaloshinski. *Methods of Quantum Field Theory in Statistical Physics*. Dover, New York, 1961.
- [50] A.L. Fetter and J.D. Walecka. *Quantum Theory of Many-Particle Systems*. Dover, New York, 1971.
- [51] L.D. Landau and E.M. Lifschitz. *Physikalische Kinetik*, volume 10 of *Lehrbuch der theoretischen Physik*. Akademie-Verlag, Berlin, 1978.
- [52] L.D. Landau and E.M. Lifschitz. *Statistische Physik: Teil 2*, volume 9 of *Lehrbuch der theoretischen Physik*. Akademie-Verlag, Berlin, 1977.
- [53] J. Rammer and H. Smith. Quantum field-theoretical methods in transport theory of metals. *Rev. Mod. Phys.*, 58:323, 1986.
- [54] A.M. Zagoskin. *Quantum Theory of Many-Body Systems: Techniques and Applications*. Springer, Berlin, 1998.
- [55] J. Paaske, A. Rosch, and P. Wölfle. Nonequilibrium transport through a kondo dot in a magnetic field: Perturbation theory. *Phys. Rev. B*, 69:155330, 2004.
- [56] J. Paaske, A. Rosch, J. Kroha, and P. Wölfle. Nonequilibrium transport through a Kondo dot: Decoherence effects. *Phys. Rev. B*, 70:155301, 2004.
- [57] C. Honerkamp. Electron-doping versus hole-doping in the 2d t - t' hubbard model. *The European Physical Journal B*, 21:81, 2001.
- [58] U. Larsen. Impurity Spin Lifetime and Electrical Resistivity in Dilute Magnetic Alloys. In *Proceedings of the International Conference of Magnetism ICM-73*, volume V, page 88, 1974.
- [59] U. Larsen. Resistance maximum in spin glasses. *Phys. Rev. B*, 14:4356, 1976.
- [60] R. Bulla, Th. Pruschke, and T. Costi. Numerical renormalization group method for quantum impurity systems. *Rev. Mod. Phys.*, 80:395, 2008.
- [61] J. von Delft. Quantum dots as tunable kondo impurities. *Science*, 289:2064, 2000.
- [62] T.A. Costi, A. C. Hewson, and V. Zlatic. Transport coefficients of the anderson model via the numerical renormalization group. *Journal of Physics: Condensed Matter*, 6:2519, 1994.

- [63] L. H. Yu, Z. K. Keane, J. W. Ciszek, L. Cheng, J. M. Tour, T. Baruah, M. R. Pederson, and D. Natelson. Kondo resonances and anomalous gate dependence in the electrical conductivity of single-molecule transistors. *Phys. Rev. Lett.*, 95:256803, 2005.
- [64] K. Nagaoka, T. Jamneala, M. Grobis, and M. F. Crommie. Temperature dependence of a single kondo impurity. *Phys. Rev. Lett.*, 88:077205, 2002.
- [65] A. Schiller and S. Hershfield. Exactly solvable nonequilibrium kondo problem. *Phys. Rev. B*, 51:12896, 1995.
- [66] J. G. Bednorz and K. A. Müller. Possible high- t_c superconductivity in the Ba-La-Cu-O system. *Zeitschrift für Physik B Condensed Matter*, 64(2):189, 1986.
- [67] R. Coldea, S. M. Hayden, G. Aeppli, T. G. Perring, C. D. Frost, T. E. Mason, S.-W. Cheong, and Z. Fisk. Spin waves and electronic interactions in La_2CuO_4 . *Phys. Rev. Lett.*, 86:5377, 2001.
- [68] Sudip Chakravarty, Bertrand I. Halperin, and David R. Nelson. Low-temperature behavior of two-dimensional quantum antiferromagnets. *Phys. Rev. Lett.*, 60:1057, 1988.
- [69] A. R. Moodenbaugh, Youwen Xu, M. Suenaga, T. J. Folkerts, and R. N. Shelton. Superconducting properties of $\text{La}_{2-x}\text{Ba}_x\text{CuO}_4$. *Phys. Rev. B*, 38:4596, 1988.
- [70] J. Tranquada, H. Woo, T. Perring, H. Goka, G. Gu, G. Xu, M. Fujita, and K. Yamada. Quantum magnetic excitations from stripes in copper oxide superconductors. *Nature*, 429:534, 2004.
- [71] V. J. Emery, S. A. Kivelson, and O. Zachar. Spin-gap proximity effect mechanism of high-temperature superconductivity. *Phys. Rev. B*, 56:6120, 1997.
- [72] V. J. Emery, S.A. Kivelson, and J.M. Tranquada. Stripe phases in high-temperature superconductors. *Proc. Natl. Acad. Sci. U.S.A.*, 96:8814, 1999.
- [73] Jakub Tworzydło, Osman Y. Osman, Coen N. A. van Duin, and Jan Zaanen. Quantum magnetism in the stripe phase: Bond versus site order. *Phys. Rev. B*, 59:115, 1999.
- [74] Subir Sachdev. Colloquium: Order and quantum phase transitions in the cuprate superconductors. *Rev. Mod. Phys.*, 75(3):913, 2003.
- [75] S. A. Kivelson, I. P. Bindloss, E. Fradkin, V. Oganesyan, J. M. Tranquada, A. Kapitulnik, and C. Howald. How to detect fluctuating stripes in the high-temperature superconductors. *Rev. Mod. Phys.*, 75:1201, 2003.
- [76] M. Vojta and T. Ulbricht. Magnetic excitations in a bond-centered stripe phase: Spin waves far from the semiclassical limit. *Phys. Rev. Lett.*, 93:127002, 2004.

- [77] G. S. Uhrig, K. Schmidt, and M. Grüninger. Unifying magnons and triplons in stripe-ordered cuprate superconductors. *Phys. Rev. Lett.*, 93:267003, 2004.
- [78] R. M. Konik, F. H. L. Essler, and A. M. Tsvelik. Modeling magnetic fluctuations in the stripe ordered state. *Phys. Rev. B*, 78:214509, 2009.
- [79] M. Vojta and O. Rösch. Superconducting d-wave stripes in cuprates: Valence bond order coexisting with nodal quasiparticles. *Phys. Rev. B*, 77:094504, 2008.
- [80] M. Vojta, T. Vojta, and K. K. Ribhu. Spin excitations in fluctuating stripe phases of doped cuprate superconductors. *Phys. Rev. Lett.*, 97:097001, 2006.
- [81] D. X. Yao, E. W. Carlson, and D. K. Campbell. Magnetic excitations of stripes near a quantum critical point. *Phys. Rev. Lett.*, 97:017003, 2006.
- [82] D. X. Yao, E. W. Carlson, and D. K. Campbell. Magnetic excitations of stripes and checkerboards in the cuprates. *Phys. Rev. B*, 73:224525, 2006.
- [83] N. B. Christensen, H. M. Rønnow, J. Mesot, R. A. Ewings, N. Momono, M. Oda, M. Ido, M. Enderle, D. F. McMorrow, and A. T. Boothroyd. Nature of the magnetic order in the charge-ordered cuprate $\text{La}_{1.48}\text{Nd}_{0.4}\text{Sr}_{0.12}\text{CuO}_4$. *Phys. Rev. Lett.*, 98:197003, 2007.
- [84] M. R. Norman. Linear response theory and the universal nature of the magnetic excitation spectrum of the cuprates. *Phys. Rev. B*, 75:184514, 2007.
- [85] G. Seibold and J. Lorenzana. Magnetic fluctuations of stripes in the high temperature cuprate superconductors. *Phys. Rev. Lett.*, 94:107006, 2005.
- [86] P. Wrobel, A. Maciag, and R. Eder. Bond-centred, bond-ordered stripes in doped antiferromagnets. *J. Phys. Condens. Matter*, 18:1249, 2006.
- [87] S. Sachdev. Kagome- and triangular-lattice heisenberg antiferromagnets: Ordering from quantum fluctuations and quantum-disordered ground states with unconfined bosonic spinons. *Phys. Rev. B*, 45:12377, 1992.
- [88] F. C. Zhang and T. M. Rice. Effective Hamiltonian for the superconducting Cu oxides. *Phys. Rev. B*, 37(7):3759, Mar 1988.
- [89] H. Eskes and G. A. Sawatzky. Tendency towards local spin compensation of holes in the high- T_c copper compounds. *Phys. Rev. Lett.*, 61(12):1415–1418, Sep 1988.
- [90] M. Greiter. Fictitious flux confinement: Magnetic pairing in coupled spin chains or planes. *Phys. Rev. B*, 66:054505, 2002.
- [91] T. M. Rice, Stephan Haas, Manfred Sigrist, and Fu-Chun Zhang. Lightly doped $t - j$ three-leg ladders: An analog for the underdoped cuprates. *Phys. Rev. B*, 56:14655, 1997.

Lebenslauf

Angaben zur Person

Nachname, Vorname
Adresse
Telefon
E-Mail
Staatsangehörigkeit
Geburtsdatum

Schmidt, Holger

Am Brurain 12, 76187, Karlsruhe
0721/ 6019500 Mobil: 0176/ 21690670
hschmidt@tkm.uni-karlsruhe.de
deutsch
4.2.1980



Berufserfahrung

11/2005 - 09/2009

Wissenschaftlicher Angestellter und Promotion am Institut für Theorie der Kondensierten Materie an der Universität Karlsruhe
Thema der Dissertation:
“*Correlated Electron Systems with Antiferromagnetic Spin Interaction*”

Ausgeübte Lehrtätigkeiten

10/2009 - 03/2010
08/2009 - 10/2009
10/2008 - 03/2009
08/2008 - 10/2008
04/2008 - 09/2008
10/2007 - 03/2008
08/2007 - 10/2007
04/2007 - 04/2007
04/2007 - 09/2007
10/2006 - 03/2007
08/2006 - 10/2006
04/2006 - 09/2006
10/2005 - 03/2006
04/2005 - 09/2005
10/2004 - 03/2005
04/2004 - 09/2004
10/2003 - 03/2004
04/2003 - 09/2003
10/2002 - 03/2003
06/2002 - 12/2004

Übungsleitung zur Theoretischen Physik C für Lehramt (Elektrodynamik und Quantenmechanik)
Vorlesung “Presemester: Physics” am International Department der Universität Karlsruhe
Übungsleitung zur Theoretischen Physik C für Lehramt (Elektrodynamik und Quantenmechanik)
Vorlesung “Presemester: Physics” am International Department der Universität Karlsruhe
Tutorium zur Theoretischen Physik F (Statistische Physik)
Tutorium zur Theoretischen Physik E (Quantenmechanik II)
Vorlesung “Presemester: Physics” am International Department der Universität Karlsruhe
Mathematik Vorkurs für Studierende der Physik
Tutorium zur Theoretischen Physik F (Statistische Physik)
Tutorium zur Theoretischen Physik A (Mechanik)
Vorlesung “Presemester: Physics” am International Department der Universität Karlsruhe
Tutorium zur Theoretischen Physik D (Quantenmechanik)
Tutorium zur Theoretischen Physik C (Elektrodynamik)
Zwei Tutorien zur Theoretischen Physik D (Quantenmechanik)
Übungen für Theorie der kondensierten Materie I und Tutorium für Analysis I
Tutorium für Analysis II
Tutorium für Analysis I
Tutorium für Höhere Mathematik II für Informatiker
Tutorium für Höhere Mathematik I für Informatiker
Hilfswissenschaftlicher Angestellter am Institut für Baustatik

Schul- und Berufsbildung

10/2000 – 9/2005

Diplom in Physik (Note: 1.2) an der Universität Karlsruhe

Thema der Diplomarbeit:

“*Towards a Microscopic Description of Spin Stripes in High T_C Superconductors*”

10/1999 – 7/2000

Zivildienst beim Arbeiter-Samariter-Bund Offenburg

9/1990 – 6/1997

Abitur (Note: 1.4) mit Leistungskursen Mathematik und Physik am Grimmelshausen
Gymnasium, 77654 Offenburg

Publikationen

HOLGER SCHMIDT und PETER WÖLFLE:

Transport through a Kondo quantum dot: Functional RG approach

submitted to Ann. Phys. (Berlin)

MARTIN GREITER und HOLGER SCHMIDT:

Evidence for site-centred stripes in CuO superconductors

submitted to Phys. Rev. Lett.

MARTIN GREITER und HOLGER SCHMIDT:

*Magnetic Excitations in the Site-Centered Stripe Phase: Spin Wave Theory of Coupled
Three-Leg Ladders*

to be submitted to Phys. Rev. B.

Konferenzbeiträge

Kondo model at strong coupling - An fRG approach

Posterpräsentation

DPG Frühjahrstagung, Dresden 2009

Kondo model at weak coupling - An fRG approach

Posterpräsentation

CFN Summerschool, Bad Herrenalb 2007

Nonequilibrium fRG - Application to the Kondo dot model

Posterpräsentation

384. Wilhelm and Else Heraeus Seminar, Nonequilibrium Transport of Strongly Cor-
related Systems, Bad Honnef 2007